PROCESSING, MICROSTRUCTURES, AND PROPERTIES OF ALUMINIDE-STRENGTHENED FERRITIC STEELS

A Dissertation Presented for the

Doctor of Philosophy Degree

The University of Tennessee, Knoxville

Zhenke TENG

December 2011

Copyright ©2011 by Zhenke Teng

All rights reserved.

ACKNOWLEDGEMENTS

First and foremost I would like to express my sincere gratitude to my major advisor Prof. Peter K. Liaw, for supporting me academically and financially through his patience, motivation, enthusiasm, and encouragement. I would also like to thank the committee members: Prof. Yanfei Gao, Prof. David C. Joy, and Prof. John D. Landes, for their great efforts and guidance to my PhD study.

My sincere thanks also go to Dr. Chain T. Liu and Dr. Michael K. Miller from Oak Ridge National Laboratory (ORNL), for contributing their immense knowledge and insightful comments to my study on the alloy design and atom probe tomography. I would like to thank Dr. Easo George Dr. Hongbin Bei, Dr. Yuki Yamamoto, and Mr. Cecil A. Carmichael for allowing the use of the facilities at the Division of Materials Science and Engineering, ORNL. The work included in this thesis would not be possible without their support. I am grateful to Prof. Morris E. Fine and Prof. Gautam Ghosh from Northwestern University, for their help in conducting the TEM/AEM studies, constructive comments and advices on conducting the experiments. I am also grateful to Dr. Fan Zhang from CompuTherm LLC. for her thermodynamic calculations to accelerate the alloy design process. I would like to thank Mr. Douglas E. Fielden, and his team, Mr. Larry D. Smith and Mr. Dan Hackworth, at The University of Tennessee, for their help in machining the experiment samples in a timely manner.

I am indebted to many of my student colleagues for providing a stimulating and fun environment in which to learn and grow. I am especially grateful to Dr. Gongyao Wang, Dr.

Dongchun Qiao, Dr. Fengxiao Liu, Dr. Jiawan Tien, Dr. Liang Wu, Dr. E-wen Huang, Dr. Sooyeol Lee, Dr. Feng Jiang, Dr. Li Li, Ms. Shenyan Huang, Mr. Andrew Chuang, Mr. Wei Wu, Ms. Lu Huang, Mr. Qingming Feng, Mr. Zhinan An, Mr. Wei Guo, Mr. Zhiqian Sun, Mr. Zhi Tang, and Mr. Bilin Chen at The University of Tennessee.

I am particularly grateful to my best friends, John T. Fail, Tao Zhou, Xiaowen Zeng, Scott Dossey, Elisabeth Dossey, and Dottie Pickett, for helping me get through the difficult times, and for all the emotional support, comraderie, entertainment, and caring that they provided.

This research is mainly supported by the Department of Energy (DOE), Office of Fossil Energy Program, under Grant No. DE-FG26-06NT42732 and No. DE-09NT0008089, with Dr. Patricia Rawls and Mr. Vito Cedro as the program managers. Atom probe tomography experiments were supported by the ORNL's Shared Research Equipment (SHaRE) User Facility, which is sponsored by the Office of Basic Energy Sciences, US Department of Energy.

Lastly and most importantly, I would like to dedicate my thesis to my parents, Lianchu Teng and Yuelian Huang, my sisters, Guiye Teng, Guifen Teng, and Guifang Teng, for their love, encouragement, and support in all my pursuits.

ABSTRACT

NiAl-strengthened ferritic steel is a material of interest for steam turbine applications due to their promising creep resistance, high thermal conductivity, low cost and thermal expansion coefficient. However, there are two critical issues restricting their applications: low room temperature ductility and limited creep resistance at temperatures higher than 600°C. The reasons for these behaviors have not been fully understood, especially the processing-microstructure-property relationship has not been clearly identified.

The alloys were designed, fabricated, and processed, according to the required microstructures and properties. The matrix and precipitates can be thoroughly characterized by a combination of techniques, including atom probe tomography, neutron diffraction, and electron microscopy experiments. Bending, tension, and creep tests were conducted to study the ductility and creep behaviors of the as-designed alloys. Relationships were subsequently developed between the characterized microstructures and the mechanical behaviors to provide in-depth understandings of the alloy properties.

Phase transformations and the resulting microstructure, structure, coherency, chemistry, and volume fraction of the precipitates were determined. The relationship between the precipitate microstructure and the room temperature ductility was thoroughly studied and established. Hot rolling was found to significantly improve the ductility.

Moreover, thermodynamic modeling was combined with focused experiments to study

the ductility and creep resistance. Thermodynamic calculations were used to identify the potential alloy compositions that may exhibit the balanced room temperature ductility and high temperature creep resistance, which was subsequently verified by experiements. This integrated experimental and modeling approach was found to be very effective in the alloy development process.

TABLE OF CONTENTS

CHAPTER 1 INTRODUCTION……...……1

1.1 Background……...……2

1.2 Critical Issues……....…….5

1.3 Objective……..…….7

1.4 Intellectual Merit and Broader Impacts……...…7

CHAPTER 2 LITERITURE REVIEW……9

2.1 Strengthening Mechanism of Ni-based Superalloy ……..……..…9

2.2 Alloying Effects on the Ductility of bcc Fe……...…10

2.2.1 General effects……..……10

2.2.2 Yield strength……..……12

2.2.3 Ductility……...……14

2.3 Mechanisms of Fracture in the Precipitate-Strengthened Alloys…….……15

2.3.1 Ductile fracture……15

2.3.2 Cleavage fracture……..……17

2.4 Mechanical Properties of NiAl……..…...…20

2.4.1 Yield strength……..……20

2.4.2 Ductility……...……21

2.4.3 Creep……..……23

2.5 Development of Creep-Resistant Ferritic Steels……..24

2.6 Materials Characterization Techniques……..……..…….26

2.6.1 Atom probe tomography……26

2.6.2 Neutron diffraction……..30

CHAPTER 3 ALLOY PROCESSING……...…….34

3.1 Alloy Design……34

3.2 Fabrication……..…….……34

3.3 Hot Rolling…….…….…….36

3.4 Heat Treatment……..……...……37

CHAPTER 4 CHARACTERIZATION OF NANOSCALE NIAL-TYPE PRECIPITATES BY ATOM PROBE TOMOGRAPHY…….……..38

4.1 Introduction……..……38

4.2 Experimental…….....39

4.3 Results and Discussions……...……..…..40

4.4 Summary…….…….45

CHAPTER 5 NEUTRON DIFFRACTION STUDY AND MODELING OF THE LATTICE PARAMETERS…….46

5.1 Introduction……..……46

5.2 Experimental…….....47

5.3 ND Analysis…….……..…..48

5.4 X-ray Diffraction……...…..…….51

5.5 Lattice Parameter as a Function of Temperature……..……....51

5.6 Modeling of Lattice Parameter at Room Temperature…….....…53

5.7 Discussion……54

5.8 Summary……...……..…..57

CHAPTER 6 EFFECTS OF AL ON THE MICROSTRUCTURE AND DUCTILITY AT ROOM TEMPERATURE…….…….59

6.1 Introduction……..……59

6.2 Experimental…….…...62

6.3 Phase Transformation…….…..63

6.4 Microstructure Characterization…….……..65

6.5 Partitioning Behavior of the Alloying Elements…….……65

6.6 Volume Fraction of β'……..……...…..…67

6.7 Three-Point-Bending Experiment and Fracture Behavior……..……..67

6.8 Discussion……68

6.9 Summary……...…….…..71

CHAPTER 7 EFFECTS OF PRECIPITATE MICROSTRUCTURE AND HOT ROLLING ON THE ROOM TEMPERATURE DUCTILITY……..73

7.1 Introduction……..…73

7.2 Experimental…….…...75

7.2.1 Fabrication……...……75

7.2.2 Heat treatment and thermo-mechanical treatment……...……75

7.2.3 Microstructural characterization……..……..……..76

7.2.4 Mechanical behavior……...……77

7.3 Initial Microstructure and Ductility…….……...…..77

7.4 Precipitate Microstructure……..……..79

7.4.1 Alloy FBB-8 aged for different lengths of time……..……79

7.4.2 Alloy with different β' precipitate volume fraction……...……..80

7.5 Hot Rolling……..…….……81

7.6 Discussion……83

7.6.1 Effects of inter-particle spacing…….……83

7.6.2 Effects of Al and Ni solubility in the Fe matrix……..……84

7.6.3 Effects of hot rolling……..……85

7.6.4 Approaches to improve the ductility……...……86

7.7 Summary……...……..87

CHAPTER 8 DESIGN OF ALLOY WITH BALANCED CREEP RESISTANCE AND DUCTILITY AT ROOM TEMPERATURE…...…..88

8.1 Introduction……..……..……..…88

8.2 Experimental……....89

8.2.1 Fabrication and heat treatment……89

8.2.2 Thermodyanmic property characterization…….90

8.2.3 Mechanical behaviors……..…..……..91

8.3 Thermodynamic Calculation and Experimental Validation in Fe-Ni-Al-Cr-Mo system……...….……...91

8.4 Creep Behavior……...……..…….. 93

8.5 Ductility Behavior……..……..…..…..……94

8.6 Search for Alloys with Balanced Properties……..…95

8.7 Summary……..…….……..98

CHAPTER 9 SUMMARY AND CONCLUSIONS…….…….100

CHAPTER 10 FUTURE WORK……..103

REFERENCES……105

APPENDIX: TABLES AND FIGURES…….……..127

VITA……..189

LIST OF TABLES

Table 1.1 Compositions of the recently developed creep-resistant ferritic steels…….128

Table 2.1 Chemical compositions of creep resistant ferritic steels for power plants…....129

Table 3.1 FBB Alloy compositions (wt.%)……..……130

Table 3.2 Concentration of the alloying elements in FBB alloys……..……131

Table 4.1 Composition (in at.%) of phases in an Fe-12.7 Al-10.2 Cr-9.0 Ni-1.9 Mo (in at.%). In the case of matrix α and primary β' precipitate, both analytical electron microscopy (AEM) and atom-probe tomography (APT) techiniques were employed…….…..132

Table 5.1 The elemental concentrations in the β/β' phases, and the equivalent scattering lengths……...……...….133

Table 5.2 Lattice parameters as a function of temperature…….134

Table 5.3 Atomic volumes of alloying elements in the β' NiAl precipitate……..135

Table 6.1 Composition [mass% (at.%)] of β and β' phases in prototype FBB alloys, aged at 700˚C for 100 hrs. The alloys FBB-3 to FBB-12 were determined using thin foils in AEM. Alloy FBB-13 was determined by APT……..……136

Table 7.1 Nominal compositions of the model alloys (at.%). The actual composition of FBB-8 determined by wet chemical analyses is in a very good agreement with the nominal one……...137

Table 7.2 Elemental partitioning (at.%) and precipitate volume fractions (V_f) of the studied alloys. The standard error (σ) of the concentration estimated by APT is ~ 0.03%,

given by $\sigma = \sqrt{C(1-C)N}$, where C is the concentration, N is the total number of atoms in the measured volume……..……138

Table 7.3 Comparison of the compositions (at.%) between the unrolled (HT2) and hot-rolled (HR) alloy FBB-8……...……..……139

Table 8.1 Nominal compositions of the NiAl strengthened ferritic model alloys (at.%)...140

Table 8.2 Elemental partitioning by both experimental measurement and thermodynamic predictions (at.%)……...……...141

LIST OF FIGURES

Figure 1.1 The present status of the development of creep-resistant steels for power plants……142

Figure 1.2 Sigmoidal creep behavior of the recently-developed creep-resistant ferritic steels ……...143

Figure 1.3 Pseudo-binary phase diagram from $Ni_{48.75}Al_{51.25}$ to $Fe_{97.5}Al_{2.5}$: miscibility gap between ordered (B2) and disordered (α-Fe) BCC phases……..144

Figure 1.4 TEM microstructures of a Fe-Al-Ni-Cr alloy, solution treated at 1,200℃ for 30 minutes, followed by aging at 700 ℃ for 100 hours……...…145

Figure 1.5 Tension creep curve of a previously designed alloy FBB-8 (Fe-6.5Al-10Ni-10Cr) at a load of 140 MPa and a temperature of 700°C……146

Figure 1.6 (a) Bending load and deflection curve of a recently-developed Fe-Al-Ni-Cr ferritic steel and (b) its fracture surface at room temperature……...147

Figure 1.7 Schematic diagram of the proposed research……...…….148

Figure 1.8 Comparison of allowable stresses and a sectional view of main steam pipes designed at 570 and 600℃ Schematic diagram of the proposed research…….149

Figure 2.1 (a) IMAGO atom probe, (b) schematic of atom probe tomography (APT), and (c) a representative APT sample……...……..150

Figure 3.1 (a) As-cast ingot, and (b) after hot-rolling with 80% reduction in thickness…151

Figure 3.2 Solvus temperature of NiAl decreases as reducing the Al%.....152

Figure 3.3 Microhardnesses of hot-rolled FBB-8 after aging at different temperatures for 1 hour……153

Figure 3.4 SEM micrographs showing the microstructures of hot-rolled FBB-8 after aging at different temperatures for 1 hour……..……154

Figure 3.5 Hardness of the designed alloys decrease as the aging time increases……155

Figure 4.1 A comparison of the Larson-Miller parameter plots between FBB-8 and other Fe-based materials candidates for steam turbine applications, where the LMP is calculated by T(25 + log t)/1000. Tensile creep tests were performed at 700°C under loads of 140 MPa, 100 MPa, 80 MPa, and 60 MPa……...…….156

Figure 4.2 (a) Dark field TEM micrograph showing β' precipitates (bright regions) and selected area diffraction pattern (inset) with a zone axis of [100], and APT characterization of a β' precipitate as well as the dark regions [see Figure 4.2a)] inside the precipitate: (b) Al atom map and corresponding 15 % Al iso-concentration surface, (c) Fe map, (d) Ni map, (e) Cr map, and (f) Mo map……157

Figure 4.3 APT characterization of primary and secondary β' precipitates: (a) corresponding 15 at.% Al iso-concentration surface, (b) morphology of secondary ultrafine β' precipitates, (c) selected atom map of one ultrafine β' precipitates, (d) Mo atom map, (e) Cr atom map, and (f) Al atom map. The total number of atoms analyzed is 3,532,698……158

Figure 4.4 The composition profiles of (a) the primary β' precipitates, (b) secondary β' precipitates, and (c) the volume fraction of primary β' estimated by both AEM and APT……...…….159

Figure 5.1 Comparison of the LMPs at 140 MPa between FBB-18 and other ferrite-based

candidate materials for steam turbine applications……..…….160

Figure 5.2 Representative neutron diffraction pattern and the single peak fitting result of the β' (100) superlattice reflection……161

Figure 5.3 (a) Atom map of Al and 15% Al iso-concentration surface, (b) atom map of Cr, and (c) the volume fraction of primary β' estimated by lever rule……162

Figure 5.4 The separation of a ND fundamental reflection (110)……...……163

Figure 5.5 Lattice misfit between the matrix and precipitates as a function of temperature……164

Figure 5.6 Representative XRD pattern and the single peak fitting result of the β' (100) superlattice reflection……..……..165

Figure 5.7 Lattice volume of the matrix (a) and precipitates (b) as a function of temperature ……...……166

Figure 6.1 (a) The heating curves from the DSC analysis of the alloys with different Al% showing a phase transition peak at a temperature higher than $T_{\beta'(NiAl)}$. This is most likely to be the phase separation of FeAl inside NiAl. (b) A comparison between the DSC curves of the solution-treated and aged alloys…….167

Figure 6.2 Centered dark-field (using 100_{B2} reflection) TEM micrographs of prototype alloys that are solution treated and then aged at 700˚C for 100 hrs: (a) FBB-3, (b) FBB-8, and (c) FBB-12. In each case, the diffraction pattern is shown as inset……...168

Figure 6.3 As-collected EDS spectra: (a) from the β matrix, and (b) from a β' precipitate in FBB-8 aged at 700˚ for 100 hrs……169

Figure 6.4 Partitioning ratios of Al and Ni in prototype alloys with different Al contents as determined by AEM. All alloys are aged at 700 ˚C for 100 hrs. The results show that the solubility of Ni in Fe matrix in the alloys is almost constant, while that of Al increases significantly as the Al content in the alloys increases……..170

Figure 6.5 The effects of Al content in the alloy on the bending ductility and hardness of prototype alloys, where ε_f is the failure strain on the outer surface of the strip sample……171

Figure 6.6 Cleavage fracture surfaces of bending-tested samples (a) FBB-3, (b) FBB-8, (c) FBB-9, and (d) FBB-13, the representative ductile fracture is shown as inset……...172

Figure 7.1 The microstructures of FBB-8: (a) optical micrographs showing the average grain size of the alloy aged at 700˚C for 100 h is ~ 100 μm, (b) TEM dark field (DF) micrograph using 100_{B2} reflection showing the average precipitate size of the aged alloy is ~130 nm, and (c) USAXS intensity vs. scattering vector plot of FBB-8 aged for different time periods at 700˚C. The inter-particle spacing can be calculated by 2π over peak Q……...173

Figure 7.2 Representative atom map of elements in both the β matrix and β' precipitates (Alloy FBB-8). All the compositions can be measured by counting the numbers of collected ions……174

Figure 7.3 Microstructure and ductility of the alloy FBB-8 aged for different time: (a) bending ductility showing an independence of inter-particle spacing and precipitate size, (b) The inter-particle spacing showing a near linear relationship

with the precipitate size……175

Figure 7.4 Bending ductility vs. β' precipitate volume fraction (V_f) curve showing the ductility decreases as V_f increases……176

Figure 7.5 Elemental solubility in the β matrix showing low Al and high Ni solubilities contribute to the ductility improvement……177

Figure 7.6 (a) SEM image showing the microstructure of the hot-rolled FBB-8 after aging at 850℃ for 1 h, and (b) EBSD mapping showing many subgrains with a size of ~ 1 μm inside the elongated grains……178

Figure 7.7 (a) Tensile stress vs. strain curve of hot rolled FBB-8, (b) fracture surface showing a mixture mode of cleavage and ductile rupture, and (c) high magnification image of the fracture surface in both ductile and cleavage areas……...179

Figure 7.8 Atom-probe samples of the alloy FBB-8 by SEM in (a) unrolled and (b) hot-rolled conditions showing the coarsening of the precipitates……180

Figure 8.1 APT characterization of the FBB alloys: (a) SEM figure of the FBB-8 sample after polishing, (b)-(f): Representative atom maps of different elements in the alloy FBB-8……..181

Figure 8.2 Calculated isothermal section of Fe-Al-Ni-10Cr-2Mo (wt.%) system at 700^{o}C……182

Figure 8.3 Synchrotron high energy X-ray diffraction of alloys (a) FBB-12 and (b) FBB-13 revealing the possible formation of a small amount of FCC-Fe phase…….183

Figure 8.4 Comparisons between the calculated and experimentally determined results

showing good agreements: (a) elemental solubilities in Fe matrix, and (b) elemental partitioning in NiAl. Note that the data points of some elements in (a) and (b) overlap with each other as their concentrations are very similar. The detailed concentration of each element can be found in Table 8.2……184

Figure 8.5 (a) Representative tension creep strain and creep rate versus time curves of alloy FBB-18, (b) Steady-state-creep rate decreases as increasing the precipitate volume fraction……...……..185

Figure 8.6 Bending ductility increases with decreasing the B2-ordered precipitate volume fraction and Al solubility in Fe matrix…….……186

Figure 8.7 Thermodynamic calculations of phase fraction and the solubility of elements in the matrix BCC-A2 phase as a function of the Ni content for (a) and (b): Fe-10Cr-2Mo-10Al-(9-15)Ni, (c) and (d): Fe-10Cr-2Mo-11Al-(9-15)Ni, (e) and (f): Fe-10Cr-2Mo-12Al-(9-15)Ni……..187

Figure 8.8 (a) Comparison of the designed alloys regarding the ductility and Larson-Miller parameter (LMP) at a tensile stress of 140 MPa. The alloy FBB-21 predicted by the thermodynamic calculations exhibited a balance between the ductility and creep resistance, and (b) comparison of the LMPs at 140 MPa between the designed alloys and other ferrite-based candidate materials for steam turbine applications……..188

CHAPTER 1 INTRODUCTION

The efficiency of the conventional fossil-power plant is a strong function of the steam temperature and pressure. An increase of the efficiency from 47%, representing the current state-of-the-art plant, to around 55% will be achieved through increasing the steam temperature from 593°C to 700°C [1]. The Ultra-Supercritical Steam Turbines Program sponsored by the Department of Energy (DOE) Fossil Energy Program requires an increase of the steam temperature from 593°C to 677°C by the year 2010 and to 760°C by 2020 [2-3].

The materials with good thermal conductivity and low thermal expansion are preferable for thick-section components of the steam turbine. Cost efficiency demands the use of the relatively inexpensive materials. These requirements give an advantage to ferritic steels, as compared to austenitic steels and Ni-based superalloys. The current creep-resistant ferritic steels, which are used in power plants [4], can be divided into CMn- steels, Mo- steels, low-alloyed CrMo- steels, and 9-12 weight percent (wt.%) Cr- steels. Figure 1.1 shows an overview of the present development of the resistant steels for power plants. Based on 9 – 12 wt.%Cr-steel, the newly-developed steels, T/P91, T/P911, and T/P92 (compositions are shown in Table 1.1), have moved the application of ferritic steels into the range of austenitic steels. T/P911 and T/P92 will enable live steam and hot reheat lines to be operated at 605°C and 625°C, respectively [5]. However, the further developments of the 9 - 12%Cr-steel have been proved to be very difficult in the past two decades [5]. All the recent developed materials seemed promising from short-term creep tests. As shown in Figure 1.2, those

materials exhibited sigmoidal creep behavior in long-term creep tests. So far no ferritic alloys demonstrated superior long-term creep resistance than P92. The microstructure investigations of those recently-developed steels shows that the complex Z-phase nitride [Cr(V, Nb)N] takes place in the steels at the expense of the strengthening carbonitrides, which dissolve and result in the sigmoidal creep behavior.

As presented in Figure 1.2, Inconel 617, which is a face-centered-cubic (FCC) nickel-based γ/γ′ superalloy, exhibits the best creep resistance. This is due to the presence of a high volume fraction of coherent–coplanar ordered γ′ precipitates. For the body-centered-cubic (BCC) Fe matrix (β), there is a miscibility gap in the Fe–Ni–Al system, as shown in Figure 1.3, which makes precipitate hardening with the B2 (Fe, Ni)Al-phase (β') possible [6-7]. The lattice parameters of α-Fe (0.28665 nm) and NiAl (0.28864 nm) are very similar [8]. Therefore, the β' precipitates can form in a coherent-coplanar orientation, providing the possibility of achieving a β/β' Fe-based analogue to the γ/γ' Ni-based superalloys. Figure 1.4 exhibits the microstructure of a Fe-Al-Ni-Cr alloy obtained from the preliminary research [9]. β' precipitates with a size of about 100 nm in diameter form coherently in the Fe matrix after aging at 700°C for 100 hours. By modifying the composition and controlling the microstructures, it is possible to achieve a Fe-based alloy with competitive mechanical properties, compared to the Ni-based superalloys.

1.1 Background

NiAl-type *B*2 precipitates have been previously observed in ferritic Fe-Al-Ni-Cr alloys [10-12]. Bradley [13-15] was the first to report the phase separation involving Fe and

NiAl-type phases in the Fe-Al-Ni system. He determined the isothermal and vertical sections of the Fe-Ni-Al system showing a miscibility gap. Following Bradley, Hao et al. systematically studied this miscibility gap [7] using diffusion-couple experiments, for temperatures ranging from 850°C to 1,150°C. Marcon et al. [16] confirmed the results of Bradley and found a γ-Fe loop existing at the Fe side, which can be inhibited by the small addition of Al.

Two Ph.D.s at Northwestern University, Kolesar and Calderon, focused on the investigation of the NiAl-type precipitation kinetics in Fe-Ni-Al and related alloys [17-18]. Calderon et. al [18-19] investigated the morphology and coarsening behaviors of NiAl-type precipitates in the Fe-Al-Ni-Mo alloy system. He suggested that Mo additions alter the lattice misfit between the NiAl-type precipitates and the Fe matrix and stabilized the spherical morphology of the NiAl-type precipitates during prolonged aging [19]. Stallybrass et al. [20] studied the Fe-Al-Ni-Cr alloy system and demonstrated that the microstructures consist of large precipitates with a mean precipitate size of around 400 nm and the small precipitates with a precipitate size of below 10 nm. Blavette et al. [11] used an atom-probe-field-ion microscope and determined the composition of the B2 precipitate in the Fe-19Cr-4Ni-1.87Al alloy to be $(Ni_{0.86}Fe_{0.12})Al_{1.02}$ (at.%). Miller et al. [21] also studied the precipitates in the Fe-Al-Ni-Mo alloy by the atom-probe tomography and found there was no Mo segregation to the precipitate-matrix interface, and Mo barely partitioned to the NiAl-type precipitates. However, the detailed analysis of the hyperfine particles, and the microstructures in a higher order alloy system [9] (with the addition of Cr, Mo, Zr, and B), which shows the improved creep resistance,

have not been performed.

Recently, mechanical properties of ferritic Fe-Al-Ni or Fe-Al-Ni-Cr alloys have been reported. Jung [22] examined the creep behavior of Fe-(6 to 8)Al-(12 to 14)Ni and Fe-(9 to 11)Al-(19 to 21)Ni alloys from 550 to 900°C. The steady-state creep rate of the alloy was about $10^{-8}s^{-1}$ at a stress level of 50 MPa and 750°C, with a 20-volume percent (vol. %) of NiAl. Zhu et al. [23] investigated the creep behavior of the Fe-2Al-4Ni-19Cr alloy and generated a power law with a stress exponent of 4 after the threshold-stress compensation. Stallybrass et al. [24] investigated the creep behavior of the Fe-Al-Ni-Cr system with different volume fractions of NiAl. He found that the stress dependence can be described as a power law with a threshold stress, comparing favorably with Zhu et al.'s results [23]. The oxidation behavior of the Fe-Al-Ni-Cr system has been studied. Rawers and Mattlin [25] examined the oxidation resistance of Fe-12Ni-7Cr alloys containing 0 to 6 wt.% Al over the temperature range of 800 to 1,000°C. When the Al content was between 3 and 4.5 wt.%, a substantial improvement in the oxidation resistance was found to be due to the formation of a protective Al_2O_3 layer, which formed over the Cr_2O_3 layer. However, a systematic study of the effects of several important parameters (i.e., the β' volume fraction, and β' particle size, grain size, and alloying) on the creep resistance has not been performed. There are also very few studies related to the ductility of the Fe-Al-Ni system. Stallybrass et al. [24] used four-point-bending tests to study the ductility and pointed out that the secondary precipitates formed during the aging process caused brittleness problems, and it can be improved by a two-step aging treatment.

1.2 Critical Issues

One of the main critical issues restricting the application of the NiAl-strengthened-ferritic steels is the limited creep resistance at temperatures higher than 600°C. Ferritic Fe has the open BCC structure and thus, has higher self-diffusion rates and lower creep strengths, as compare to the FCC Ni-based alloys. Figure 1.5 shows a tension creep curve of one of the previously designed alloys [9]. It appears that the materials rupture in ~ 2 h at a load of 140 MPa and a temperature of 700°C, while the target is 2% elongation for a 30-year period at a load of 35 MPa and a temperature of 760°C. For the Fe-Ni-Al alloy system, Calderon's study [18] indicated that the creep resistance is strongly affected by the coarsening rate of the precipitates, which is a function of lattice misfit between β and β' phases, and the volume fraction of β'. In addition, the yield stress of the polycrystalline stoichiometric NiAl was reported to drop rapidly with increasing temperature above 623°C [26], which leads to a much lower strengthening effects of the NiAl particles at high temperatures. The stoichiometry study of the NiAl suggested that the Ni-rich NiAl is stronger [27] and small deviations from the stoichiometry result in an increase in both the hardness and strength [28].

Since the precipitate microstructure and composition are such important factors in controlling the creep resistance, detailed characterizations of the precipitates will need to be conducted. Understanding the relationship between the precipitate microstructure features and the mechanical properties will be crucial in searching for the possible solutions to improve the creep resistance.

As the creep resistance is one of the most important properties for high temperature applications, previous research on the Fe-Al-Ni alloy system has focused on the phase stability [11-13], microstructures [14, 15], and properties [16, 17] related to the creep behavior. However, another critical issue of these materials, the low ductility at room temperature has been rarely mentioned [16]. The steels must have not only adequate creep rupture strength but also good fabricability (e.g., hot workability, weldability, and hot bending). Figure 1.6 represents a bending load-deflection curve and the fracture surface of this material. The curve before rupture shows almost only an elastic deformation. The calculated bending strain at the failure point is about 0.94% [9], which is much lower than the required ductility of 10 - 15 % for sufficient fabricability. The flat facets of the fracture exhibit river markings, which is the characteristic feature of a brittle cleavage fracture. This characteristic is caused by the crack moving through the crystal along a certain crystalline planes that form a series of plateaus and connecting ledges. As described in Figure 1.4, the microstructures of the Fe-Al-Ni-Cr alloy system consist of two major phases: the β ferritic Fe matrix and β' (Fe, Ni)Al-type-strengthening precipitates. The ferritic stainless steels exhibit up to 30% in elongation and 60% in area [29]. Therefore, the reduction of the ductility most likely comes from the formation of NiAl precipitates and/or the compositional change associated with the partitioning of the alloying elements. This reinforces the importance of the characterization of the precipitates, including the size, inter-particle spacing, volume fraction, and composition. The effects of the matrix composition and grain size will also need to be investigated. Furthermore, the microstructural features required to satisfy the combined creep and ductility properties will be carefully identified.

1.3 Objective

Figure 1.7 shows the schematic of the proposed research. The ultimate objective of the proposed research is to design innovative ferritic NiAl-strengthened superalloys for fossil-energy applications at temperatures up to 760°C [2-3]. The alloy design aims at (1) a steady-state creep rate of approximately 3 x 10^{-11} s^{-1} at a temperature of 760°C and a stress level of 35 MPa [2-3], and (2) a tensile ductility of more than 10% at room temperature. To meet the performance goal set by the DOE Fossil Energy Program, a set of microstructural and mechanical properties requirements must be satisfied. Specifically, this research will employ the transmission-electron microscopy (TEM), scanning-electron microscopy (SEM), X-ray diffraction (XRD), atom probe tomography (APT), and neutron diffraction to characterize the microstructures of the Fe matrix and β' NiAl-type particles; and conduct a systematic study of the effects of the microstructural features and compositions of the β and β' phases on the ductility and creep resistance of the designed alloys. The experimental results will be compared with those of thermodynamic calculations. After the dominant microstructrual features are determined, an alloy composition with combined balanced creep resistance and ductility will be predicted by thermodynamic calculations and verified by focused experiments.

1.4 Intellectual Merit and Broader Impacts

The main purpose of this research is to develop a ferritic based alloy analogous to γ/γ' Ni-based superalloys, which have been extensively investigated. However, the β/β' Fe-based alloys have BCC/B2 structures, and the fundamental study to understand their microstructures and mechanical properties have not been conducted. Specifically, the nano-scaled NiAl-type precipitates have not been carefully characterized. The ductility of these alloys was rarely

mentioned in the previous studies, and their fracture mechanism at room temperature has not been determined. A systematic study of the effects of the microstructural features (i.e., the β' volume fraction, β' particle size, grain size, and elemental partitioning) on the creep resistance and ductility has not been conducted. Furthermore, the alloy with combined balanced creep resistance and ductility has not been identified. These critical studies will be addressed in this thesis and the results will provide further understanding for the β/β' Fe-based alloy system. In addition, the demonstration of the alloy-design approaches may be applicable for the design and development of other high-temperature materials in the power-generating industry.

The potential applications and outcomes of the development of the β/β' Fe-based alloy system include: (1) a suitable candidate for the application to steam-turbine components operating at temperatures higher than 700°C. The development of this ferritic steel will be mainly used for thick-section pipes and headers of the boiler, and the blade materials of the turbine, (2) a capital cost reduction in steam turbines. Figure 1.8 shows a comparison of allowable stresses and a sectional view of main steam pipes (the concentric circles) designed at 570 and 600°C [3]. At any given temperature, higher allowable stresses for a material permit the design of thinner wall headers/pipes. This trend not only reduces thermal stresses, but also reduces cost [3], and (3) the increase in the thermal efficiency of the steam turbine and the reduction in not only the fuel costs but also the release of SO_2, NO_x, and CO_2 emissions. This fact is very significant in view of the worldwide agreements to reduce CO_2 emissions by 2010 and the fact that a 1% increase in the efficiency of an 800 MW machine would lead to a lifetime reduction in CO_2 approaching one million tons [26].

CHAPTER 2 LITERATURE REVIEW

2.1 Strengthening Mechanisms of Ni-based Superalloy

Typical Ni-based superalloys are variations of an FCC Ni-Cr-W γ matrix, further hardened by coherent precipitates of $L_1 2$ γ' with optional additions of Co, Ti, Zr, B, C, and Fe [27]. The understanding of the strengthening mechanisms involves the strengthening of the γ matrix, as well as the means by which γ' precipitates.

In the case of solid-solution strengthening of the γ matrix, there are several theories of yielding in terms of the effects of solutes on various physical or crystallographic properties, such as the lattice parameter, elastic modulus, and short-range order. Mott and Nabarro [28] concluded that the yield stress τ for a dilute solid solution is given by:

$$\tau = 2G\varepsilon c \tag{2.1}$$

where G is the shear modulus, ε the misfit, and c the concentration of solute atoms. The studies conducted by Pellous and Grant [29] showed that the change in yield stress for various solutes in Ni also depends directly upon the position of the solute in the periodic table. Fleischer [30-31] suggested that modulus difference between the solute and solvent may give rise to strengthening, due to that extra work is needed to force a dislocation through hard or soft regions in the matrix. In addition, concentrated solid solutions are likely to exhibit appreciable short-range order. The energy required to shear a short-range-ordered crystal causes an increase in the flow stress of the alloy [27].

The major contribution to the strength of precipitation hardened Ni-based superalloys is provided by the formation of coherent stable intermetallic compounds, such as γ' [Ni_3(Al, Ti)] [27]. Both single crystals and polycrystals of unalloyed γ' exhibit a reversible increase in the flow stress between -196°C and about 800°C [32]. The factors that have been suggested to account for observed hardening of Ni-based superalloys by coherent precipitates include [27]: (1) coherency strains, (2) differences in elastic moduli between precipitate and matrix, (3) existence of order in the precipitates, (4) difference in stacking fault energy of precipitate and matrix, (5) energy to create additional precipitate-matrix interface, (6) increases in lattice resistance of precipitates with temperature. Among all of them, the major factors that contribute to strengthening are coherency strains and the presence of order in the precipitates [27].

2.2 Alloying Effects on the Ductility of BCC Fe

2.2.1 General effects [33]

The studied alloy system contains 7 elements, Fe, Al, Ni, Cr, Mo, B, and Zr. To further understand the physical and mechanical behaviors of the designed steels, it is necessary to firstly review their effects on steels.

Al can improve the oxidation resistance of the steels, if added in substantial amounts. As a deoxidizer, up to 0.05% Al may be added to steel. Al is also the most effective alloying element in controlling the grain growth prior to quenching. For increasing fine grain characteristics or sub-zero impact properties, up to 10% may be added. Approximately 5% added to the Cr steel increases electrical resistivity. In precipitation hardening steels, Al is

used to form the intermetallic compounds that increase the strength in the aged condition [33].

Ni increases the strength and toughness of ferritic steels without seriously affecting the ductility. It is generally added in amounts ranging from 1-4%. Ni also tends to help reduce cracking during the quenching phase of heat treatments. Addition of 5% of Ni provides high fatigue resistance. When alloyed at higher proportions, significant corrosion resistance results and at 27% a non-magnetic stainless steel results. 9% Ni steels are useful at very low temperatures. High nickel increases the resistance to corrosion, and in combination with Cr, is used in the austenitic corrosion-resisting steels [33].

Cr is commonly added to steels to increase the corrosion resistance and oxidation resistance, or to improve high-temperature strengths. As a hardening element, Cr is frequently used with a toughening element, such as nickel, to produce superior mechanical properties. At higher temperatures, Cr contributes to the increased strength. Cr is the most important alloying element in stainless steels. It is this element that gives the stainless steels their basic corrosion resistance. The corrosion resistance increases with increasing the Cr content. It also increases the resistance to oxidation at high temperatures. Cr promotes a ferritic structure. Steels with at least 13% Cr is called "stainless" steels. Despite the name, all steel can rust if not maintained properly [33].

Mo promotes the formation of ferritic structures in steels. It is widely used because of its powerful effect in increasing the steel strength at high temperatures. It forms stable carbides, raises the temperature at which softening takes place on tempering and increases the

resistance to creep. In high speed steels, it can be used to replace approximately twice its weight of W. The corrosion resistance of stainless steels is improved by Mo additions. It enhances the creep strength of low-alloy steels at elevated temperatures. Mo also promotes the formation of secondary phases in ferritic steels. Additions of 0.5% Mo have been made to plain-carbon steels to give the increased strength at boiler temperatures of 400°C, but the element is mainly used in combination with other alloying elements [33].

B is added to steels to improve hardenability. The addition of about 0.003 % of boron confers the increased harden ability to steels in the quenched and tempered condition. Furthermore, it has been found that the addition of 0.003% B to low-carbon, 0.50% Mo steels in the normalized condition doubles the yield strength and gives a 30% increase in the tensile strength [33].

Zr can be used to achieve improvements in inclusion characteristics. Zr causes sulfide inclusions to be globular rather than elongated, thus improving the toughness and ductility in transverse bending. Zr acts as a deoxidizing element in steels and combines with the S [33].

2.2.2 Yield strength

The effects of many alloying elements on the yield strength of BCC Fe was summarized by Leslie [28, 34]. They investigated [28, 34] the yield strength of alloys with different elements, minus the yield strength of Fe, as a function of temperature. The magnitudes of solid solution strengthening and softening are apparent. With the exception of

Co and Cr, the strengthening behavior produced by each alloying element increases with decreasing the temperature to a maximum at room temperature, and drops sharply into the alloy softening region around 150 K.

There are several different theories developed to understand the solid-solution strengthening effects of alloying elements. Mott and Nabarro [28] considered that the solid solution hardening is independent of temperature and is due to an atom size misfit. Most other theories [30-31] included both the size and shear modulus misfit parameters. Suzuki's theory [35] involved a temperature (T) -dependent strengthening, and considered that the strengthening is proportional to 1/T. Van der Planken and Deruyttere [36] attempted to account for electronic effects in strengthening. Leslie [34] compared all these theories with the experimental results, and found that there is no single simple relation between the size misfit, the modulus misfit, and the solid solution component of strengthening that will apply to all alloys. He concluded that the size misfit parameter, $(1/a_0) \times (da/dc)$, where a_0 is the lattice constant of BCC Fe, and da/dc is the change of the lattice parameter as a function of the alloying concentration, is reasonable good indicator of the strengthening of BCC Fe by low concentrations of substitutional solutes, but there are important exceptions. He also found that the solid solution softening of the alloying elements at a temperature lower than 150 K. This phenomenon can occur regardless of whether the solute atoms are substitutional or interstitial, whether Young's modulus or the shear modulus is increased, decreased, or remains unchanged by the solute. The theories to understand the solid solution softening was not fully developed, and limited explanations were given by Leslie [34].

2.2.3 Ductility

The effects of a variety of elements on the physical and mechanical properties have been thoroughly reviewed by Leslie [34]. Pugh [37], Crutchley, and Reid [38] indicated that the ductility of pure metals is related to the ratio of the bulk modulus to shear modulus, K/G. The greater the magnitude of this ratio, the higher the ductility of the metal. The relationship between the Poisson's ratio and K/G can be expressed by:

$$\nu = \frac{3K/G - 2}{6K/G + 2} \tag{2.2}$$

The rationale [37-39] is that as K/G decreases, more elastic energy is stored as dilation rather than as shear deformation. Therefore, elastic stress concentrations at roots of crack become more intense since the plastic flow is more difficult. Speich et. al [40] compared the K/G and v values of a variety of alloying steels. He pointed out that this theory worked well for many elements but failed for Si, Co, Ru, and other additions [40]. The discrepancy may lie in the use of an average shear modulus.

The effect of solute elements on the cohesive energy is another theory to explain the ductility of alloying BCC Fe [34]. In this theory, the cohesive energy was assumed to increase smoothly with the number of s, p, and d electrons. Fe has 8 such electrons, elements having more should improve ductility, elements having less should be harmful. On this basis, Co, Ni, Rh, Ir, and Pt would be expected to improve ductility, with Ni and Pt having the greatest effects. Ductility would be decreased markedly by Si and S and somewhat less by Cr, Mn, and Re. When comparing the predicted results with those measured by experiments, this theory also work well for most elements but failed for some others [34].

Among all the alloying element (Al, Ni, Cr, Mo, Zr, and B) included in the studied alloy system, Al has the most significant effects on the ductility. It was reported that the ductility of Fe decreases with increasing Al alloying contents [41-45]. This problem is aggravated by ordering reactions when the addition of Al is more than 10 at.%. At such high Al contents, there is a transition from the disordered atom distribution to an intermediate state, and then to long-range ordering to produce the DO_3 crystal structure and B2 structure with increasing Al contents [46]. In addition, the Al segregation at grain boundaries may contribute to embrittlement [47]. Herrmann [48] investigated the deformation behaviors of Fe-Al alloys at low temperatures. He revealed that the dislocation mobility is lower in the alloys with higher Al contents, which is the major reason contributing to the ductility decrease with increasing the Al additions.

2.3 Mechanisms of Fracture in the Precipitate-Strengthened Alloys

2.3.1 Ductile fracture

The mechanism of ductile rupture in the precipitate-strengthened alloys is that it is initiated by the generation of voids at the precipitate - by either decohesion of the precipitate/matrix interface or cracking of the precipitates themselves [49]. These cavities grow as the material is strained further, and ultimately the cavities coalesce by an internal necking mechanism to give the dimpled fracture surface characteristics. The mechanism of how the voids nucleate at the precipitates was reviewed by Goods and Brown [50]. This model proposed that as the matrix flow, the regions within and around the particles must increase in the elastic energy, and that at a certain strain, it is energetically favorable for this locally concentrated strain-energy to be released by the decohesion or fracture of the

precipitates. After the voids are nucleated, Brown and Embury's model [51] assumed that they grow by plastic extension. When the voids have been extended, a plastic slip line field can be constructed between the voids, so that the voids can coalesce. The final fracture surface, corresponding to the result of the processes described above, will consist of an array of dimples, each dimple containing a precipitate.

The role of precipitates in the ductile fracture has been investigated by Smith and his present and former associates at Cambridge [52-55]. They found out that voids form first at the larger precipitates, then at progressively smaller precipitates as the strain increases. There were only a fraction of precipitates associated with voids. This finding was consistent with Pelloux [56] 's study on Al age-hardening alloys. It was reported that the size of the dimples observed fractographically is much larger than the interparticle spacing, indicating that only a fraction of the particles present are contributing to fracture.

The effect of particle size on ductility has not been completely established nor is it clear whether or not the precipitate size dependence is related to the absolute size or volume fraction of precipitates. The theoretical analyses of Gurland [57] and Ashby [54] would indicate that the ductility should increase as the precipitate size increases. However, a general agreement was not established for different materials. Other studies showed that the ductility was independent of the precipitate size [58] or even exhibited a different trend [59].

Several studies [60-64] demonstrated that the tensile elongation decreases rapidly with increasing the precipitate volume fraction. It was reported [63-64] that the composite

failure is associated with particle cracking and void formation in the matrix within clusters of particles. The ductility as a function of the precipitate volume fraction was developed by Brown and Embury [51]. They proposed a model, which enables an estimate of the failure strain ε_f.

$$\varepsilon_f = \frac{1}{C} \ln\left(\sqrt{\pi / 6f} - \sqrt{2/3} + e_n\right) \tag{2.3}$$

where C is the factor that the voids elongate at a rate faster than the rate of extension of the specimen itself ($1 < C < 2$), f the precipitate volume fraction, and e_n the nucleation strain. It is clearly seen that this model was in good agreement with the data of Edelson and Baldwin [65]'s study on some dispersion-strengthened Cu-based alloys.

The strength of the precipitate itself relative to that of the metal matrix can alter the observed ductility significantly. If the fracture strength of the precipitate is low, it will lead to early void nucleation. Hard, tough precipitates that do not deform with the matrix substantially alter the flow pattern in the metal. When numerous and small, they can strengthen the metal matrix considerably. When coarse and present in low-volume fractions, they act principally to lower the ductility, making little contribution to the strength [66].

2.3.2 Cleavage fracture

The process of cleavage fracture consists of three stages: (1) plastic deformation, which involves the pile-up of dislocations along their slip planes at an obstacle, (2) the buildup of shear stress at the head of the pile-up to nucleate a microcrack, (3) in some cases the stored elastic strain energy drives the microcrack to complete fracture without the further

dislocation movement in the pile-up. A distinct growth stage is observed in which an increase stress is required to propagate the microcrack [67].

In the precipitate-strengthened alloys, the nucleation of a crack can come from a grain-boundary precipitates [68]. This is a direct consequence of the high local stresses, which are generated by inhomogeneous plastic deformation processes in the form of a pile-up of dislocations in the surrounding matrix. Kotilainen and Torronen [69] examined and evaluated the fracture behavior of a Cr-Mo-V steel, which had been quenched and tempered at various temperatures. They concluded that crack nucleation and initial growth occur with difficulty because the fine dispersion of carbides restricts the necessary dislocation motion to form stress concentration. However, the propagation of the microcracks is easier than their nucleation. The arresting of a propagating microcrack depends on the possibility of some plastic deformation at the crack tip absorbing energy. The dislocations are locked by the dispersion and thus the crack can propagate without losing energy. The dispersion is, therefore, beneficial in raising the stress required for crack nucleation, but it is ineffective against crack propagation since the dispersion determines the ease of the plastic deformation. This feature will result in an increase of the ductile/brittle transition temperature with decreasing the dispersion spacing.

It has been shown experimentally that reducing the size of grain-boundary carbides in steels significantly lowers the transition temperature, due to that the cleavage is initiated from grain-boundary cracks [70]. There is strong evidence that in engineering materials, the most difficult step is generally the propagation of deformation-produced microcracks through a

strong barrier, such as a grain boundary. Thus, the grain size will have a strong influence on the brittle-fracture behavior. Petch [71] reported that the brittle fracture stress increases as reducing the grain size.

In the particle-strengthened alloys in which the crack initiates in the matrix, the quantitative relationship between the inter-particle spacing and the ductility was developed by Baker [72]. The rationale of this model lies in that the hard particle dispersion can improve the ductility by limiting the dislocation pile-up. The critical inter-particle spacing where optimal ductility is achieved can be calculated by [72]

$$\lambda_{crit} = \frac{\pi G b^2}{\gamma(1+\nu)} + 2r_s \tag{2.4}$$

where λ_{crit} is the critical inter-particle spacing, G the shear modulus, b the magnitude of the Burgers' vector, γ the surface energy, ν the Poisson's ratio, and r_s the precipitate radius. The optimal ductility ε_f can be expressed by:

$$\varepsilon_f = \frac{1}{\theta}\left\{\left[\frac{4G(1+\nu)\gamma}{\pi(\lambda - 2r_s)}\right]^{1/2} - \sigma_0 - \frac{Gb}{(\lambda - 2r_s)}\right\} \tag{2.5}$$

where σ_0 is the lattice resistance, and θ the work hardening rate. Baker's model [72] also proposed that there is a λ_{max}, which can be calculated by

$$\lambda_{max} = \frac{G}{\sigma_0}\left\{\left[\frac{(1+\nu)\gamma}{\pi\sigma_0}\right]^{1/2} + \left[\frac{(1+\nu)\gamma}{\pi\sigma_0} - b\right]^{1/2}\right\}^2 + 2r_s \tag{2.6}$$

Between λ_{crit} and λ_{max}, as predicted by Baker's model, the ductility decreases as the inter-particle spacing increases. Using this model, it is possible to predict the optimal inter-particle spacing in our studied alloy systems. As the particle spacing is a function of the

particle size and precipitate volume fraction, its optimal value can be achieved by controlling the alloy compositions and heat treatment process.

2.4 Mechanical Properties of NiAl

2.4.1 Yield strength

Although yield strength is the most commonly reported mechanical properties for polycrystalline NiAl, inconsistencies are evident in literature [73]. The lack of agreement may be due to differences in the grain size, interstitial content, texture from thermomechanical processing, and chemistry [73]. The yield strength of polycrystalline stoichiometric NiAl is typically reported to be relatively independent of temperature from RT to ~800 K [74-76], and to drop rapidly with increasing the temperature below RT and above ~900 K [75-77]. Several studies have observed that the tensile strength of NiAl increases with temperatures up to ~ 1,000 K [76]. Stoichiometry also has a strong effect on the yield strength of NiAl. Stoichiometric NiAl is the weakest binary alloy below 1100 K [77-79] but is reported to be stronger than both Ni-rich and Al-rich NiAl above 1500 K [79]. Although an increase in the yield strength is observed for both Ni- and Al-rich alloys at lower temperatures, the magnitude of the strengthening effect is not equivalent. Most studies have found a greater hardening rate in the Al-rich alloys, suggesting that vacancies provide greater resistance to the dislocation motion than that produced by substitutional atoms [80].

Solid solution alloying of NiAl has been investigated in a number of studies, including Be [81], B [82], C [81], Cr [82], Mo [83], Y [83], and Zr [84]. Among all these

elements, B, Be, and C pose the strongest strengthening effects [73, 80]. George and Liu [81] explain this solid strengthening effects in terms of the relative size of the atom, compared with the resident site of the atom in the NiAl matrix. For elements which dissolve interstitially, the greater the radius the larger the associated strain field and the greater the resistance to dislocation motion, thus resulting in a greater hardening effect.

The effect of grain size on yield strength is complicated by the additional variable of alloy composition. Several studies clearly indicated that the influence of grain size on yield stress increases with increasing the deviation from stoichiometry [84]. Consequently, yield strength is essentially independent of the grain size for NiAl alloys very close to stoichiometry, whereas the yield strength of non-stoichiometric alloys is strongly influenced by grain size. The effect of grain size on yield strength is further complicated, when alloying additions are involved. It is reported that when NiAl is alloyed with 0.05 at.% Zr, the yield strength is independent of grain size in the range of 16 to 280 μm, but becomes strongly dependent on grain size in the range less than 16 μm [84].

2.4.2 Ductility

Polycrystalline NiAl deforms predominantly by <100> slip on {011} and occasionally {001} type planes [80]. There are only three independent available slip systems, which is less than the five independent deformation modes considered necessary for extensive, uniform, crack free deformation [85]. It was reported that the tensile ductility of NiAl at room temperature was very low, ranging from 0 to a maximum of ~ 4% [76, 81, 86]. Observations

of grain boundary fracture in both tension and compression specimens at low temperatures appear to confirm that limited ductility results from the incompatibility in shape changes of neighboring grains because of an insufficient number of slip systems [76, 81, 87]. It was reported that the oxygen embrittlement was responsible for the intergranular fracture [88]. However, in-situ Auger electron spectroscopy studies of the NiAl alloys [81] after various heat treatments revealed that the grain boundaries in NiAl are clean and free from the measurable impurity contamination, including oxygen. Another theory believed that the intergranular fracture comes from the fact that the grain boundaries are intrinsically weak due to their structure [89-90]. However, grain boundary structure simulations for NiAl indicated that there are no periodic structural defects present at the grain boundaries in near stoichiometric NiAl which would cause the grain boundaries to be inherently weak [91-92].

Two mechanisms have been proposed to provide the additional modes of deformation: the activation of additional slip vectors and dislocation climb. It has been shown that a<110> dislocations become mobile at the same macroscopic stress required for the movement of a<100> dislocations as a result of elastic and plastic constraints at grain boundaries [93]. Dislocation climb has been suggested to contribute to the deformation of polycrystalline NiAl above the ductile-brittle transition temperature (DBTT) [75-76, 94]. A combination of a<100> glide and the climb of a<100> edge dislocations provides the requisite five independent strains [95].

While alloying additions to polycrystalline NiAl typically increase the DBTT, Be has little effect [81], and low levels of Mo have been shown to increase the ductility at room

temperature (RT) [96]. Recent data shows a remarkable effect of small additions of Mo, Fe, and Ga on the RT tension ductility in <110> [97-98] and <111> [98] single crystals. While the effects of these elements have not been determined, it is not likely that significant improvements in polycrystalline ductility will result unless these additions are able to encourage the nucleation of non-a<100> dislocations [93]. It has been suggested that additions which lower the ordering energy, such as Cr, Mn, and Fe, will favor a<111> slip [99].

In the case of the effects of grain size on the ductility, a good agreement was not achieved from different studies. Schulson [100] suggested that grain refinement can be used to increase the ductility of brittle intermetallics, such as NiAl, and performed tensile tests on NiAl as a function of grain size and temperature to support this view [99]. A critical grain size of ~ 20 μm was reported to exist in Ni-49 at.% Al tested in tension at 673 K, and smaller grain sizes result in significant ductility (> 40%) [101]. Only a mild effect is observed for stoichiometric NiAl at RT, with an increase of ~ 2% ductility in specimens with a grain size below 20~30 μm [86]. However, Chan's quantitative model on the relationship between the grain size and ductility in brittle materials argued that there is very little grain size dependence of ductility at RT for grain sizes greater than 1 μm. Consequently, grain size refinement alone is not a practical method for achieving significant improvements in the ductility of NiAl at RT [80].

2.4.3 Creep

As mentioned in Section 2.4.1, the yield strength of NiAl decreases rapidly as

increasing the temperature. There is a decrease of about 8 orders of magnitude in the creep rate as progressive alloying changes are made from pure Ni to Ni-based superalloy [102]. Similar improvements will be necessary for NiAl to compete with current Ni-based superalloy. Solid solution strengthening of NiAl was reported on many elements, especially Zr [103]. Significant improvements in the creep strength of NiAl by precipitation hardening were also demonstrated by Polvani et al. [104] by adding Ti to form a two phase mixture of NiAl and the Heusler phase Ni_2AlTi. The Heusler phases and other intermetallic compounds can be formed with ternary additions, such as Nb, Ta, Hf, and Zr. However, it was reported that this effect is only evident at high stresses, but not in the low stresses regime [104-107]. Fine dispersions of second phases were reported to increase the creep resistance of NiAl [108-110], as those particles are generally resistant to coarsening because of their very low solubility in the matrix. However, the use of rapid solidification to dispersion strengthen NiAl has not yet provided sufficient strengthening to compete effectively with superalloys [80].

2.5 Development of Creep-Resistant Ferritic Steels [4]

Table 2.1 gives an overview on creep resistant ferritic steels, which are used in power plants for tubing and piping [4]. The list of steels can be subdivided into CMn-steels, Mo-steels, low alloyed CrMo-steels, and 9-12 wt.%Cr-steels. The steel grades have been listed according to the increasing content of alloying elements.

In the CMn-steel, the C and Mn contents are the major factors influencing the strength. One of the representative steel is P235, with a composition shown in Table 2.1. The

Mo-steels are very similar to the CMn-steels but with an addition of ~ 0.3 wt.% Mo, which is a strong solution hardening element. The solution hardening effect is the main reason for the increase of the creep rupture strength. However, it has been found that the creep ductility strongly decreases with increasing the Mo content [4]. Another limitation in the application of Mo-steels is the observed decomposition of carbides above 500°C. A solution to both problems was the use of Cr as an alloying element in combination with Mo. CrMo-steels were the first ones that allowed steam temperatures in power stations above 500°C. Their creep-rupture strengths are distinctly higher than the simple Mo-steels. Cr also promotes the use at higher temperatures as it increases the oxidation resistance. However, a problem was reported [4] from the use of low Cr ferritic steels, like T/P22, in combination with high Cr austenitic steels. The higher C affinity of the high Cr austenitic steel caused a massive diffusion of C from the ferritic steel into the austenitic steel. As a result, a strong decrease of strength occurred in the ferritic steel and an embrittlement in the austenitic steel. The problem was solved by alloying T/P22 with Nb leading to the formation of Nb carbides instead of Cr carbides. The stronger affinity of C to Nb prevents a carbon depletion of the ferritic steel and consequently a decrease in the strength.

The increase of Cr in CrMo-steels above 7 wt.% leads to a group of steels. Further improvements of the creep strength have been achieved by alloying with V, Nb, W, and B. The higher creep-rupture strength of X20CrMoNiV11-1 is mainly caused by the higher amount of $M_{23}C_6$ carbides. The prototype of the new steels from this development work is the modified 9% Cr steel T/P91 invented in the USA [111-112]. Although the C content is

lower, the creep rupture strength of T/P91 is distinctly higher than that of X20CrMoNiV11-1. This has been achieved by alloying with V and Nb. T/P91 uses the precipitation of finely dispersed Nb/V carbonitrides of type MX as additional strengthening effect. It was essential to balance the composition, because an optimal dispersion and particle size of MX can only be achieved by an optimized Nb/V ratio and nitrogen content. Subsequently new steel grades have been developed on the basis of T/P91, like X11CrMoWVNb9-1-1 (T/P911), T/P92 and T/P122 [113]. These steel grades represent the current state of development for creep resistant ferritic steels.

T/P911 and T/P92 are currently the focal point of interest in Europe. They are intended for use in main steam lines. T/P911 and T/P92 differ only in their Mo and W contents, while the Mo equivalent (Mo + 1/2 W) of both steels is nearly the same. W has been added as an additional hardening element. First it was believed that W mainly acts in solution hardening due to its large atomic size. However, it has been found out later [4] that most of the W content will precipitate as Laves phases during the service operation. The benefit of B is believed to decrease the coarsening rate of carbides. On the other hand, T/P122 is more preferred for use as boiler components because of its higher oxidation resistance. The disadvantages of T/P122 are mainly found in the area of fabricability [4].

2.6 Materials Characterization Techniques

2.6.1 Atom probe tomography

The atom probe is a combination of a field ion microscope and a mass spectrometer

[114]. In the time-of-flight mass spectrometer, ions are field evaporated from the specimen by the application of either a high voltage positive-polarity pulse to the specimen or a negative-polarity pulse to a counterelectrode a few millimeters in front of the specimen, as shown in Figure 2.1. The amplitude of the pulse voltage is typically 15%–20% of the standing voltage on the specimen. The amplitude of the pulse, the standing voltage, and the specimen temperature are all selected to ensure that all atoms have the same probability of being field evaporated on the application of the pulse [114].

In the field evaporation process, the potential energy of an atom on the surface due to the voltages on the specimen, *neV*, is converted into the kinetic energy of $1/2(mv^2)$, when the ion leaves the specimen. *n* is the number of electrons removed from the atom during the field evaporation, *e* is the charge on an electron, *V* is the total applied voltage on the specimen, *m* is the mass of the atom, and $v = d/t$ is the speed of the atom which, to a good approximation, is taken to be constant because the ions reach a terminal speed within a few tip radii, *d* is the distance between the specimen and the detector, and *t* is the time of flight. Therefore, the mass-to-charge-state ratio *m*/*n* of the ion is given by

$$\frac{m}{n} = \frac{2e}{d^2}(V_{dc} + \alpha V_{pulse})t_e^2 \tag{2.7}$$

where α is a factor less than 1, V_{dc} is the standing voltage on the tip, and V_{pulse} is the pulse voltage amplitude. The time of flight is determined with a time-to-digital converter (TDC) from the time between the application of the field evaporation pulse and the impact of the ion on the single ion detector at the end of the mass spectrometer [114].

In the three-dimensional atom probe, as atoms on the surface of the specimen field evaporate one at a time and fly toward a two-dimensional position-sensitive detector, their hit position in x and y is recorded. Gradually, each atom on the surface evaporates and exposes the underlying layers. The sequence of atom hits on the detector can be used to track both the serial evaporation of atoms in a given layer and the serial evaporation of the layers. The three-dimensional image is thus reconstructructed from this combination of two-dimensional hit positions and field evaporation sequence. The scanning atom probe and local electrode atom probe were developed later on for the materials that a needle-shaped specimen is difficult to fabricate. [114]

There are two features of APT making it stand out among analytical instruments: three dimensional compositional imaging at the nanoscale analysis of buried features and high analytical sensitivity. The image resolution is excellent, but electron microscopy and scanning probe instruments can exceed it for pure image resolution. It is the spatial resolution of APT as an analytical technique that is unmatched. Many scientific instruments offer a compositional imaging mode where characteristic signals are resolved spatially on a point-by-point basis. The spatial resolution of such images is the resolution of the technique when operated in a focused-probe mode. The highest spatial resolution technique of these is the scanning transmission electron microscopy (STEM) which can provide 1 nm resolution laterally from x-ray emissions and 0.2 nm resolution laterally from electron energy loss events. However, these images are integrated through the specimen thickness, which is about 10 nm. APT achieves better than 0.3 nm in all three directions of a three-dimensional image

simultaneously. Because it is a three-dimensional technique, APT excels at an analysis of subsurface or buried features in specimens. These can include one-dimensional features such as dislocations, two-dimensional features, such as layers and interfaces, and three-dimensional features, such as precipitates. With a wide field of view, about 250,000 atoms per atomic layer can be recorded. For the interfacial segregation, the sensitivity is therefore about 40 appm/atomic layer and is limited principally by the number of atoms detected per layer. For bulk analyses, the sensitivity can be 10 appm or better. It is typically limited by the background signal in the mass spectrum as long as enough atoms are collected. For an analytical imaging technique, this is a very high sensitivity. Thus APT, especially as practiced by the high speed, large field of view instruments, offers an unparalleled combination of compositional imaging at the atomic scale of multidimensional objects with high analytical sensitivity [114].

APT has been applied in the characterizations of many materials. In the case of precipitate-strengthened Ni-based superalloys, APT has been used to characterize the partitioning of the alloying elements between the different phases, solute concentration profiles across the interphase interface and grain boundaries, and the site occupancy of solute additions in the ordered phase [115-117]. The morphology and distribution of phases can be also characterized. Isoconcentration surfaces are used to visualize the interface between regions of different compositions, such as the γ' precipitates and the surrounding γ matrix.

The high spatial resolution of APT enables the early stages of phase separation and their evolution of the phases to be characterized. Classic samples of this type of study are the

phase separation that occurs within the miscibility gap in the Fe-Cr system [118-120] and the formation and evolution of Guinier-Preston (GP) zones in aluminum alloys [121]. APT can be also used in the characterization of the segregation of solutes to a dislocation [122], grain boundaries, interphase interface [123], and multilayer thin films [124].

2.6.2 Neutron diffraction

Neutron diffraction is a powerful tool to characterize the materials microstructures, based on the Bragg's Law. This law establishes that a diffracted beam exists for a wavelength, λ, at an angle 2θ, relative to the incident beam, by the atoms lying in the {*hkl*} lattice planes with a spacing, d_{hkl}, if the relation [125]:

$$2d_{hkl}\sin\theta = n\lambda \tag{2.8}$$

is satisfied, in which *n* is an integer defining the order of reflection. Diffraction patterns of polycrystalline materials can be usually obtained, using a diffractometer. Through the evaluation of the measured intensity distributions of the reflections (*hkl*), the primary data can be extracted from the diffraction pattern, including the peak positions and integral intensities. The whole diffraction pattern can be analyzed through performing full profile fittings using Rietveld refinement methods. The Rietveld method refines user-selected parameters to minimize the difference between a whole experimental pattern (observed data) and a model based on the hypothesized crystal structure and instrumental parameters (calculated patterns) [126-127]. Neutrons have many properties that make neutron diffraction an important tool for characterizing materials behavior. Neutrons penetrate deeply into most engineering materials, such that the entire volume of a specimen can be probed by neutron beams regardless of the

specimen orientation during the measurements. Thus, the information obtained is averaged over a bulk sampling volume.

The neutron study included in this thesis utilized The Spectrometer for MAterials Research at Temperature and Stress (SMARTS), at the Manuel Lujan Jr. Neutron Scattering Center, Los Alamos Neutron Science Center (LANSCE) at the Los Alamos Nation Laboratory (LANL), optimized for the study of engineering materials. SMARTS provides an exciting range of capabilities for studying polycrystalline materials focusing on two areas: the measurement of deformation under the stress and extreme temperature, and the measurement of spatially resolved strain fields.

Similar to the Ni-based superalloys, the lattice misfit between the BCC Fe matrix and the coherent B2 NiAl-type precipitates is a parameter of significant importance in controlling the creep resistance. The main purpose of using neutron diffraction in the thesis is to accurately determine the lattice parameters of those two phases. However, this kind of measurement is not simple. Firstly, due to the very small lattice misfit between the β and β' phases, their fundamental reflections are often not clearly resolved and are sometimes completely overlapped. The accuracy of the lattice parameter determination may therefore depend to a great extent on the peak deconvolution procedure adopted. Even in case when the resolution allows one to distinguish the two peaks, it is non-trivial to ascribe the peaks to the respective phases. Secondly, as the precipitates are coherent with the matrix, there are local strains in the matrix surrounding the precipitates. Because of this feature, the lattice parameters are not

constant, but vary continuously with position, especially close to the β/β' interface. Thirdly, in alloys with high precipitate volume fractions, as the inter-particle distances are small, the strain field around neighboring precipitates overlaps. Lattice parameter measurements in the constrained microstructure of the two-phase system therefore present additional difficulties due to strains leading to peak broadening and changes in the peak profile [128].

Several techniques have been used to measured the lattice parameters of γ and γ' phases in Ni-based superalloys, including convergent beam electron diffraction (CBED), XRD, and ND. For CBED, there are a number of factors, which may restrict the accuracy of the results [129]. In this technique, the higher order Laue zone (HOLZ) lines in the bright field disc of the diffraction pattern are used to provide a highly sensitive measurement of lattice misfit. In the standard aged specimen, where a considerable amount of strain is present, the diffuse nature of the HOLZ lines makes precise determination of the positions of γ and γ' difficult. This can lead to a significant amount of error, especially in alloys with small misfit values where the shifts in the line positions between the two phases are minimal. In addition, local strains may result in deviations from the cubic symmetry, a phenomenon which is particularly evident in the over-aged specimens. Additionally, surface relaxation in the foil can distort the HOLZ lines. Consistent choice of regions in the material is necessary if segregation occurs in the alloy. Overall, the data from this technique display a high degree of scatter and, therefore, a large number of patterns must be collected and analyzed for a reasonable accurate determination of the lattice misfit [129].

The diffraction techniques by XRD and ND are more accurate than the others [130]. In the case of Ni-based superalloys, although XRD generally gives a better resolution than ND, it was not adequate to resolve the overlapping γ and γ' peaks [128]. ND is able to probe a larger specimen volume, allowing the easy measurement of samples with a thickness of around 2-3 mm, which is representative of bulk samples in industrial applications. In addition, it was reported that ND data provided high reflection intensities for the fundamental γ and superlattice γ' reflections [131]. Therefore, ND is very well suited for the purpose to measure the lattice misfit between β and β' phases in the current studied alloy system. The Rietveld refinement of ND data has been used to provide volume fractions for both γ and γ' phases in the Ni-based superalloys [131]. ND has also been used to characterize the residual microstrains arising from the plastic deoformation of pollycrystallline Ni-based superalloys [132].

CHAPTER 3 ALLOY PROCESSING

3.1 Alloy Design

The selection of the alloy compositions will be guided primarily by the computational results [133]. The nominal compositions of the alloys are listed in Table 3.1 (in wt.%). The FBB-1 alloy is the base composition. The additions of 10% of Ni and 10% of Al are used to form the NiAl-type precipitates. 10% Cr is added for the oxidation resistance improvement. The alloying of 3.4% Mo is to control the misfit between the β and β' phases and to solid-solution strengthen the β matrix. 0.25% of Zr or Hf is added to promote the slow diffusion in the matrix. 0.005% B was included to enhance the grain-boundary cohesion. In FBB-4, Nb, V, and C are utilized for the formation of extra strengthening carbides. The addition of W in FBB-5 and FBB-6 is for extra solid-solution strengthening. From FBB-7 to FBB-13, different amounts of Al will be added to examine the effects of Al on the ductility at room temperature and creep resistance. The partitioning behavior of Zr will be studied in FBB-14 and FBB-15. The possible formation of Heusler precipitates by the addition of Ti will be investigated in FBB-16. From FBB-18 to FBB-19, varying amounts of Ni will be added to investigate their effects on the creep resistance. Although more than 20 alloys will be fabricated, only those alloys exhibiting significantly different mechanical properties (creep resistance and ductility) will be selected for the detailed study.

3.2 Fabrication

Vacuum arc-melting (VAR) will be used to prevent the contamination from air and

remove dissolved gases. For prescreening tests, small ingots will be melted and drop into a Cu mold with a dimension of 12.7 mm × 12.7 mm × 76.2 mm. A representative ingot image is shown in Figure 3.1a. After the optimal composition is identified, larger ingots will be fabricated for detailed study. Wet chemical analyses will be used to verify the exact concentrations of every alloying element after fabrication. A preliminary wet chemical analysis of FBB-2 and FBB-3 is summarized in Table 3.2. The results are consistent with the nominal compositions and clearly indicate the existence of 0.25% Hf in FBB-2 and 0.25% Zr in FBB-3. These results proved that the alloys in our research can be fabricated successfully by the approach described above.

3.3 Hot Rolling

Hot rolling will be used to refine the grain size and reduce the metallurgical defects for selected alloys. The hot rolling was performed at 750°C and a total reduction of 80% in thickness. A representative hot rolled material is shown in Figure 3.1b. To refine the grain size, the recrystallization temperature needs to be carefully measured. In this thesis, it is determined by microhardness tests and verified by SEM micrographs. For most metallic materials, the recrystalllization can be empirically estimated by 0.4 T_m, where T_m is the melting temperature. The DSC curves in Figure 3.2 show that T_m is ~1,400°C. Therefore, the samples were heat-treated at 6 different temperatures varying from 500°C to 1,000°C for 1 hour.

The microhardness test results vs. annealing temperature are plotted in Figure 3.3. As

can been seen, the significant drop of the hardness from 482 to 385 (Hv_{500}) at the temperature 700°C indicates that the recovery process begins at this temperature. The hardness increases very quickly back to 480 at 800°C, and drops slightly to 446 at 900°C. One reason for the hardness increase during this temperature range is that the grain size refinement starts at this temperature. Another explanation is the formation of strengthening NiAl precipitates as the DSC study (Figure 3.2) shows that the transition from B2 to α-Fe begins at a temperature of ~750°C. At a temperature lower than 750°C, there is no B2 precipitate formed from the over-saturated α-Fe. Therefore, the hardness of samples aging from 500°C to 800°C is predominately controlled by only the recovery process. At the temperatures range between 800°C to 1,000°C, both recrystallization and precipitate hardening contribute to the hardness increase. The slight drop of hardness at 900°C is possibly due to the precipitate and grain size coarsening.

The hardness tests results indicates that the recrystalllization temperature should be a temperature around 800°C. The SEM investigation was conducted to verify this estimation. The SEM micrographs are shown in Figure 3.4. At 800°C, the grains are still elongated as the hot-rolled materials. However, refined structures with a size less than 1μm were formed at the temperature of 900°C. At 1,000°C, the grains grow to 20 μm, and at 1,200°C to more than 100 μm. Therefore, the recrystallization process was conducted at a temperature of 850°C for 1 hour in our study.

3.4 Heat Treatment

Due to the multi-component nature of the alloy system in this research, the solvus temperature of the B2 phase will be changed by different additions elements, as shown in Figure 3.2. A proper heat-treatment process must be developed to avoid the excessive grain growth at the solution-treatment temperature. DSC will be utilized to measure phase-transformation temperatures, including the solvus temperature of the NiAl phases and the melting temperature of the alloys. The aging time is another important factor to control the microstructure features. A preliminary hardness test of the alloys aged for different times is shown in Figure 3.5. The hardness decreases as the aging time increases and changes only slightly after a long period of aging (100 h). A Vickers microhardness of 450 is reached after annealing for 100 hours.

CHAPTER 4 CHARACTERIZATION OF NANOSCALE NIAL-TYPE PRECIPITATES BY ATOM PROBE TOMOGRAPHY (APT)

4.1 Introduction

Similar to the γ/γ' Ni-based superalloys [134], the creep resistance of the NiAl-strengthened ferritic steels is expected to be a strong function of the microstructural characteristics of the β' precipitates, such as the volume fraction, average size, lattice parameter, and chemistry. Previous studies of Fe-Al-Ni based alloys focused on the coarsening kinetics of β' precipitates [19, 135] and their interactions with dislocations [19, 22-23, 136]. However, further improvement of the creep properties and understanding of the creep behavior require a systematic microstructural characterization of these strengthening precipitates. Specifically, the phase transformation processes and resulting microstructures, composition of the β' precipitates, and the partitioning behavior of the alloying elements in relation to the alloy chemistry, have not been thoroughly investigated.

In this Chapter, we report the microstructural characterization in a recently designed [137] β'-strengthened ferritic alloy (FBB-8) with a nominal composition of Fe-12.7Al-9Ni-10.2Cr-1.9Mo (the composition is in atomic percent throughout this chapter, unless specified otherwise). Previous study [137] showed that FBB-8 has the optimal combined bending ductility (~1%) and hardness (435 Hv_{500}) at room temperature among a series of designed Fe-Al-Ni-Cr-Mo alloys. Figure 4.1 compares the Larson-Miller parameter (LMP) of FBB-8 to the other Fe-based materials candidates for steam turbine applications [138]. As

can be seen, FBB-8 does not show superior creep resistance than the other candidates at high stresses (> 100 MPa). However, considering that the application stress for steam turbines is only 35 MPa, FBB-8 is comparable to the other candidate materials at 80 MPa and higher than most materials except HR-1200 at 60 MPa.

In an effort to establish the composition-processing-microstructure relationsship, our goal is to characterize NiAl-type precipitates in FBB-8 with the combined use of transmission electron microscopy (TEM), analytical electron microscopy (AEM), and atom probe tomography (APT). This is a part of our current research to design and study NiAl-strengthened ferritic steels with optimal properties for high temperature applications.

4.2 Experimental

The alloy ingot of FBB-8 was fabricated by the approach introduced in Section 3.2, Chapter 3. A rod with a length of 20 mm was subsequently cut from the ingot. They were solution-treated at 1,200 °C for 30 min. in evacuated and sealed quartz tubes, followed by air cooling, and then aged at 700 °C for 100 h. The cooling rate was roughly estimated to be 60°C/min. A HITACHI-8100 TEM and HITACHI HF-2000 AEM, both operating at 200 kV, were used in this study. The AEM is equipped with an ultrathin window Link energy dispersive X-ray (EDX) detector. The X-ray collection time was between 300 and 500 s, and the electron probe size was about 10 nm. Care was taken to avoid a two-beam condition in order to minimize electron-channeling effects [139]. The background subtracted integrated intensities of the EDX spectra were converted to compositions, the details of which may be

found elsewhere [140-141]. The local electrode atom probe (LEAP®) was performed with a pulse repetition rate of 200 kHz, a voltage pulse fraction of 0.2, and a specimen temperature of 60K.

4.3 Results and Discussions

Figure 4.2 presents the dark field TEM micrograph showing primary β' precipitates. The inset shows the corresponding [100] zone axis electron diffraction pattern. Strain contrast imaging, along with the absence of interfacial dislocations, confirmed that the β' precipitates are fully coherent with the α matrix. The lattice parameters of both phases in the aged sample were measured by neutron high-resolution powder diffraction (HRPD). At room temperature, the measured lattice parameter is 2.8858 Å for the ferritic matrix (a_α) and 2.8876 Å for the β' precipitate ($a_{\beta'}$), corresponding to a lattice misfit ($\delta = \frac{|a_\alpha - a_{\beta'}|}{a_\alpha}$) of 0.06%. The lattice parameters of pure Fe and stoichiometric NiAl are 2.8665 Å and 2.8864 Å, respectively [8]. Therefore, in the model FBB-8 alloy, the Fe matrix is dilated by alloying elements more than that of the β' precipitates, primarily due to preferential partitioning of Mo in the Fe matrix, which is discussed further below for all the alloying elements. The measured lattice misfit is consistent with the results reported by Calderon et al. [19], where the traditional X-ray diffraction (XRD) technique was used to determine the misfit. The near zero lattice misfit decreases the driving force for particle coarsening, as reported for Ni-based superalloys [27], which is beneficial for the creep resistance.

The spherical morphology of β' precipitates in Figure 4.2a is also consistent with the

low misfit strain. It is well known that elastic interactions between misfitting particles affect their shape, spatial arrangement, and coarsening behavior. The relative dominance of strain and interfacial energies on the shape of coherent precipitates has been discussed by Voorhees et al [142]. When the interfacial energy dominates the equilibrium shape yields a spherical morphology [142], as has been observed in other alloys [141].

In Figure 4.2a, the phase separation in primary β' precipitates resulting nanoscale dark domains (less than 20 nm in diameter) may also be noticed. Since Figure 4.2a was acquired using a (100)-type superlattice reflection, the dark regions observed inside the β' precipitates by TEM are believed to be the disordered (α-Fe solid solution) phase, which results from the precipitation of the excessive Fe in the NiAl during air-cooling from 1,200 ˚C and/or during aging at 700 ˚C. A similar phenomenon, i.e., the γ precipitates inside γ' has also been reported for γ/γ' Ni-based superalloys [143].

To gain further insight into the dark domains observed within the β' precipitates, APT was conducted. Figure 4.2b exhibits the Al atom map and the 15% Al iso-concentration surface inside a β' precipitate. It clearly reveals the existence of several precipitates, corresponding to the dark domains in Figure 4.2a. The atom maps of the other elements presented in Figures 4.2c-f indicate that this phase is enriched with Fe and Cr, depleted of Ni and Al, while Mo does not show significant partitioning preference. The APT data was used to determine the composition of nano-domains inside the β' precipitate and was found to be $Fe_{73.1}Al_{8.1}Ni_{4.2}Cr_{11.4}Mo_{2.5}$, which is close to that of the α-Fe matrix, as will be discussed in the

following sections.

Besides the primary β' precipitate shown in Figure 4.2a, the APT study also revealed the formation of another type of precipitates in the α matrix, but with a significantly smaller size compared to the primary β' precipitate. The representative APT data for the two types of precipitates is shown in Figure 4.3a. Note that those precipitates are not observed in Figure 4.2a. The β' precipitates in Figure 4.2a were imaged using a β' diffraction spot that didn't image the much smaller precipitates. Stallybrass et. al [24] noticed such ultrafine precipitates in the Fe-Al-Ni-Cr systems, but did not characterize them any further. Most of the secondary ultrafine precipitates are spheroidal, as presented in Figure 4.3b, and their diameters vary from 1 nm to 5 nm. The selected atom map exhibited in Figure 4.3c indicates that the secondary precipitate is an Al-enriched NiAl phase. These fine precipitates are believed to have formed during air-cooling, due to the reduced solubility of other elements in NiAl. Similar duplex precipitates were also observed in several Ni-based alloys [144-145]. As reported in a previous study of an experimental Ni-based alloy [144], the presence of such ultrafine precipitates can significantly decrease the effective width of the matrix channels, producing strong effects on the creep resistance. However, these secondary β' precipitates in our alloy may not have any effect on the creep properties at 700°C [137], which is higher than their dissolution temperature. Nevertheless, these secondary precipitates were reported [24] to be the reasons contributing to the brittleness of the NiAl-strengthened ferritic steels at room temperature. They may need to be eliminated by heat treatments for sufficient workability in as-cast and subsequent fabrication stages of the designed alloys.

By analyzing the APT data, the composition of primary and secondary β' precipitates are determined to be $Ni_{41.2}Al_{43.6}Fe_{12.7}Cr_{0.8}Mo_{1.4}$ and $Ni_{26.3}Al_{41.6}Fe_{26.9}Cr_{3.3}Mo_{1.7}$, respectively. The proximity histogram composition profiles of both the primary and secondary NiAl precipitates are compared in Figures 4.4a and b. The composition differences between these two kinds of precipitates indicate that they have formed within different temperature regions. The compositions of the secondary β' precipitates suggest that some Ni atoms are replaced by Fe, which in turn reinforces the conjecture that the phase separation of β' at lower temperatures [7] may cause the precipitation of *B*2-type FeAl or (α-Fe), depending on the starting alloy composition and temperature.

The partitioning behaviors for all the alloying elements can be observed clearly from the atom maps shown in Figure 4.3. The Mo atom map in Figure 4.3d indicates that most of Mo remains in the α matrix, with a small amount partitioning into the NiAl precipitates. As Mo has a larger atomic size than Fe, this is beneficial for controlling the lattice misfit. The Cr atom map in Figure 4.3e shows that it preferentially remains in the Fe matrix, and the formation of β' precipitates does not deplete the Cr in the matrix for the corrosion and oxidation resistance. Another feature should be noted is that there is a significant amount of Al (> 7 %) remaining in the α matrix, as shown in Figure 4.3f, which is one of the reasons for the observed brittleness problem of the FBB-8 alloy at room temperature [48]. This issue has been discussed in detail elsewhere [137].

A comparison of the compositional analysis by AEM and APT is summarized in Table

4.1. In the AEM technique, the average compositions of α and primary β' phases are determined by analyzing 25 EDS spectra acquired from each phase [137]. Nevertheless, the results show a good agreement between AEM and APT techniques. In the case of primary β' precipitates, two major discrepancies are due to Fe and Mo. The discrepancy in the Fe composition is due to the presence of nanoscale domains of α within the primary β', as discussed above. Some of these nano-domains are much smaller than the probe size used in AEM, as a result they might have contributed to the X-ray generation. Consequently, the AEM data yields higher average Fe-contents in primary β' precipitate than APT. Regarding the Mo-content in both α and β', poor X-ray counting statistics in AEM, as only the Mo-K_α peak was considered, has contributed to the observed disagreement with the APT data.

Ignoring the secondary β' precipitates and assuming that the alloying elements only partition to the primary precipitates, the volume fraction of β' can be estimated based on the lever rule:

$$V_{\beta'} = \frac{C_0 - C_\alpha}{C_{\beta'} - C_\alpha} \tag{4.1}$$

where C_0, C_α, and $C_{\beta'}$ are the compositions of the alloy, α matrix, and β' precipitate, respectively. The nominal concentration (C_0) for each element minus the solute content in the α matrix (C_α) is plotted versus the difference in the composition between β' and α ($C_{\beta'}$-C_α) in Figure 4.4c. The slope of the best-fit line for all elemental compositions determined by both AEM and APT shows the volume fraction (V_f) of β' phase to be ~ 0.15 - 0.16.

4.4 Summary

In summary, phase transformations and the resulting microstructure, structure, coherency, chemistry, and volume fraction of nano-scaled NiAl-type (β') precipitates in a model ferritic steel (Fe-12.7Al-9Ni-10.2Cr-1.9Mo) were studied using the combined techniques of TEM, AEM, APT and neutron diffraction. Upon air-cooling from 1,200 ˚C and subsequent aging at 700 ˚C yield primary β' precipitates with an average diameter of 130 nm. Ultrafine secondary β' precipitates with an average diameter of 5 nm are formed during air cooling from 700 ˚C. The primary and secondary β' precipitates have compositions of $Ni_{41.2}Al_{43.6}Fe_{12.7}Cr_{0.8}Mo_{1.4}$ and $Ni_{26.3}Al_{41.6}Fe_{26.9}Cr_{3.3}Mo_{1.7}$, respectively, and that of the α matrix is $Fe_{75.1}Al_{8.1}Ni_{3.0}Cr_{11.9}Mo_{3.1}$. Phase separation leading to precipitation of α inside primary β' was also confirmed by TEM and APT. The APT analysis showed that the α precipitates inside β' has a composition of $Fe_{73.1}Al_{8.1}Ni_{4.2}Cr_{11.4}Mo_{2.5}$, which is very close to that of the α matrix. The β' precipitates are coherent with the α matrix with a lattice misfit of 0.06%. Due to a low misfit strain, the morphology of primary β' precipitates is governed by the interfacial energy. Based on the composition data, the volume fraction of the primary β' precipitates is estimated to be about 0.16.

CHAPTER 5 NEUTRON DIFFRACTION STUDY AND MODELING OF THE LATTICE PARAMETERS

5.1 Introduction

Similar to the Ni-based γ/γ' superalloys, the lattice misfit between the β and β' phase is a parameter of significant importance in controlling the creep resistance. It was reported that the coarsening rates of the precipitates in the alloys with larger lattice misfits were higher [19, 135, 146]. However, the measurement of the lattice misfit is not simple. As the lattice parameters of β and β' phases are very similar, their fundamental reflections are often not clearly resolved and sometimes completely overlapped. The accuracy of lattice parameter determinations may therefore depend largely on the peak deconvolution procedure adopted. In the case of Ni-based superalloys, many studies have been devoted to finding suitable techniques for measuring the γ/γ' lattice misfit accurately [128-130, 147]. The measurements by x-ray diffraction (XRD), convergent beam electron diffraction (CBED), and neutron diffraction (ND) were previously compared [129]. The diffraction techniques are generally more accurate than other methods, especially the inherent accuracy and reliability of XRD is well known [128]. However, ND was reported to have its own advantages in some cases [128, 131].

The material used in this study is one of the recently developed FBB series β/β' alloys, FBB-18, which exhibits very promising creep resistance. As shown in Figure 5.1, the Larson-Miller parameter (LMP) of this alloy is higher than most of the ferrite-based potential steam turbine materials. The characterizations of the precipitate microstructure and mechanical

behaviors of FBB alloys were previously investigated [137, 148]. However, the lattice misfit between the β and β' phases has not been accurately measured. In order to understand the effects of lattice misfits on the creep resistance, the lattice parameters needs to be firstly determined. In the current study, the lattice parameters were measured by ND as a function of temperature. Synchrotron high energy XRD was also conducted to validate the results at room temperature. Furthermore, the compositional dependence of the lattice parameters was modeled to predict the lattice misfit, thus may help accelerate the alloy development process.

5.2 Experimental

Neutron-diffraction experiments were carried out, using the spectrometer for materials research at temperature and stress (SMART) at Lujan neutron scattering center (LANSCE). The incident beam size is 5 mm × 7 mm, and the bulk sample size is 12.7 mm × 12.7 mm × 1 mm. The lattice parameters were measured as a function of temperatures (room temperature, 525 K, 750 K, 873 K, 973 K, and 1,073K). The measuring time for each temperature is ~ 20 min.

Synchrotron high energy XRD was conducted at the Advanced Photon Source, Argonne National Laboratory. One bar with a cross-section of 12.7 × 12.7 mm^2 and a thickness of ~ 1 mm was machined by EDM from the bulk material. The specimens were X-rayed in transmission with a high-energy X-ray (115 keV), and the diffraction patterns were recorded by a MAR-345 two-dimensional detector.

The composition of the Fe-matrix and B2 precipitates was determined by atom probe tomography (APT). To prepare the samples for APT, a thin blank with a dimension of 0.25 mm × 0.25 mm × 10 mm was cut from the bulk material by electrical-discharge machining (EDM) for the micropolishing. The electrolyte for the first stage micropolishing was 75 volume percent (vol.%) acetic and 25 vol.% perchloric acid, and for the second stage was 98 vol.% butoxyethanol and 2 vol.% perchloric acid. After a sharp needle tip was obtained by the micropolishing, it was focused-ion beam (FIB) milled to form a sharper needle tapering with a semiangle of ~ 10° and an apex between 50 and 150 nm in radius. The local electrode atom probe (LEAP®) analysis was carried out on a LEAP 4000X HR with a pulse repetition rate of 200 kHz and a voltage pulse fraction of 0.2, and at a specimen temperature of 60K.

5.3 ND Analyses

Figure 5.2 shows a typical ND spectrum obtained from the studied alloy, with the intensity plotted vs. the d-spacing. The Rietveld refinement technique [126] is used to analyze the neutron spectrum using the General Structures and Analysis System (GSAS) code developed by Larson and Von Dreele [149-150] at the Los Alamos Neutron Scattering Center (LANSCE). Details of which can be referred to the literature [126, 149-150].

With the small lattice misfit between the two phases, direct separation of the fundamental peaks into the contributions from the two-phase constituents was not achieved. The determination of the accurate values of the lattice parameter involves a single-peak-fitting procedure in GSAS [126, 149]. In the case of current study, the

superlattice reflection (100) was used to determine the d-spacing d_{100} for the β' phase, as shown in the inset of Figure 5.2. For the fundamental (110) reflection, d_{110} of β' equals $d_{100}/\sqrt{2}$. The position of the β reflection can be obtained by fitting the sum of two Gaussian peaks to the data for the composite reflections, subject to the following two constraints [132]. First, the intensity ratio of β' to β was determined from the structure factor and volume fraction, using the following equation [132]:

$$\frac{I^{\beta'}_{h\,k\,l}}{I^{\beta}_{h\,k\,l}} = \frac{\left|F^{\beta'}_{h\,k}\right|^2_l}{\left|F^{\beta}_{h\,k}\right|^2_l}\frac{v_f}{1-v_f} \tag{5.1}$$

$$F_{hkl} = b_{co}e^{2\pi i(0h+0k+0l)} + b_{ce}e^{2\pi(1h+1k+1l)} \tag{5.2}$$

where b_{ce} and b_{co} are the scattering lengths of the corner and center atoms, respectively, F_{hkl} the structure factor, and v_f the volume fraction of β'. For the β matrix phase, which has a disordered bcc structure, $F_{hkl} = b_{ce} + b_{co}$ where (hkl) are all even, and $F_{hkl} = 0$ where (hkl) are of mixed character. For the β' precipitate phase which has an ordered BCC structure, $F_{hkl} = b_{ce} + b_{co}$ where (hkl) are all even, and $F_{hkl} = b_{ce} - b_{co}$ where (hkl) are of mixed character. The values of scattering lengths are functions of the actual compositions of phases, expressed by:

$$b^{\beta'}_{ce} = \sum c^{\beta'}_{i,ce} b_i \tag{5.3}$$

$$b^{\beta'}_{co} = \sum c^{\beta'}_{i,co} b_i \tag{5.4}$$

$$b^{\beta}_{co} = b^{\beta}_{ce} = \sum c^{\beta}_{i} b_i \tag{5.5}$$

where $c^{\beta'}_{i,ce}$ is the atomic concentration of element i in the β' phase that occupy the body-centered position, $c^{\beta'}_{i,co}$ is the corresponding atomic concentration for those elements that occupy the corner position, b_i the scattering length of neutrons by the atom of element i, which can be obtained from the literature [151], c^{β}_{i} is the atomic concentration of element i

in the β phase. The site preferences of the alloying elements in the *β*' phase were taken from Jiang's study [152], which used first-principles to calculate the fractions of Fe, Cr, and Mo occupying the Al sublattice as a function of temperature and composition of NiAl. In the current study, the compositions were determined by APT. The representative atom maps of Al and Cr (Figures 5.3a and b) clearly show an interface between the matrix and precipitates. Details of the APT characterization of a similar alloy have been presented elsewhere [148]. The results summarized in Table 5.1 revealed that the β' NiAl precipitate phase is nearly stochiometry in the studied alloy. The precipitate volume fraction can be estimated by lever rule. The nominal concentration (C_0) for each element minus the solute content in the α matrix (C_α) is plotted versus the difference in composition between *β*' and α ($C_{\beta'}$-C_α) in Figure 5.3c. The slope of the best-fit line for all elemental compositions shows the volume fraction (V_f) of *β*' phase to be ~ 0.28. With all the parameters calculated above, the intensity ratio was determined to be 0.29 by Eq. (5.1).

The second constraint for the deconvolution is to assume the widths of the two peaks were taken to be equal and background was flat. The combined peak profile for the (110) reflection can be subsequently deconvoluted to two separate β and β' peaks, as shown in Figure 5.4. From the position of the β peak, the lattice parameter of the β phase can be calculated. The position of the β' peak is on the left side of that of β, indicating that the lattice parameter of β' is smaller than that of β, resulting in a negative lattice misfit, as calculated by:

$$\delta = 2(a_{\beta'} - a_\beta)/(a_{\beta'} + a_\beta) \tag{5.7}$$

Using the same approach described above, the lattice misfit at different temperatures can be calculated. The results plotted in Figure 5.5 show that the misfit decreases as increasing the temperature.

5.4 X-ray Diffraction

Figure 5.6 presents a representative XRD pattern of the studied alloy at room temperature. There was no peak splitting was observed, indicating that the lattice misfit is very small. The intensities of the superlattice reflections are relatively low as compared to those of the ND pattern. This feature is due to the intensity of the β' superlattice reflections depends on the difference in the scattering between Ni and Al atoms, and this difference is quite small in the case of X-rays [128]. Using the same single peak fitting procedure for the ND pattern, it yields a lattice parameter of 2.8772 ± 0.0016 A for β'. The determination of the lattice parameter of β can be achieved by the same approach adopted in the ND measurement. Considering the variance is relatively larger, this value is still in good agreement with the ND result.

5.5 Lattice Parameter as a Function of Temperature

The lattice parameters of both β and β' phases increase with increasing the temperature, as shown in Figure 5.7 and Table 5.2. Using the equation $V_i = a_i^3$, the lattice volume for both phases can be expressed as a function of temperature by fitting the data polynomially:

$$V_\beta = 23.46(1 + 5.1\times10^{-5}T - 5.5\times10^{-8}T^2) \quad (5.8)$$

$$V_{\beta'} = 23.08(1 + 7.2\times10^{-5}T - 4.9\times10^{-8}T^2) \quad (5.9)$$

The coefficients of thermal expansion (α) can be subsequently determined by:

$$\alpha = \frac{1}{V}\frac{\partial V}{\partial T} \tag{5.10}$$

The calculated values of α for the β matrix and β' precipitates at room temperature are 1.8 × 10^{-5} K^{-1} and 4.3 × 10^{-5} K^{-1}, respectively. The reported thermal-expansion coefficients of NiAl and α-Fe are 1.3 × 10^{-5} K^{-1} [80] and 1.2 × 10^{-5} K^{-1} [153] at room temperature, which are both lower than the measured values in our study.

The intensity ratio between (100) and (110) reflection at different temperatures can be used to indicate how the β' precipitate volume fraction change with the temperature. The intensity of the reflections is proportional to the β' precipitate volume fraction and can be expressed by:

$$I_{hkl} \propto \frac{V j N_0^2 F_{hkl}^2}{\sin\theta_{hkl} \sin 2\theta_{hk}} \tag{5.11}$$

where N_0 is the number of unit cells per unit volume, F_{hkl} the structure amplitude factor of the unit cell, V the volume of the sample in the neutron beam, j the multiplicity of the diffracting planes {hkl}, θ_{hkl} the Bragg angle of the reflection. The values of the integrated intensity of (100) and (110) reflections can be obtained by the single peak fitting procedure. The measured ratio between I_{100} and I_{110} reflections at different temperature were determined to between 0.17-0.19. Accounting for the standard errors of these measurements are 0.02, the values of I_{100}/I_{110} can be considered invariant, i.e. more β' phase precipitate did not form in the studied temperature range. This finding is consistent with a previous DSC study [137], which revealed that the precipitation of β' occurred at a temperature higher than 923K.

5.6 Modeling of Lattice Parameters at Room Temperature

The composition dependence of the lattice parameters of bcc binary Fe-Al [154-156], Fe-Ni [157-158], Fe-Cr [157-158], Fe-Mo [157, 159] alloys have been systematically investigated previously. Vegard's law can be subsequently applied to predict the lattice parameters of the alloy system consisting of these elements. However, Ghosh's study [160] revealed that the composition dependence of the lattice parameters of some Fe-X subsystem exhibited a strong non-linearity with an asymmetric and a deviation from Vegard's law. To account for this effect, we use the Ghosh's model [160] to predict the lattice parameters in the current studied Fe-Al-Ni-Cr-Mo system. The lattice parameter of bcc Fe matrix can be expressed by [160]:

$$a_{matrix} = 3.0287\,x_{Al} + 2.7801\,x_{Ni} + 2.8847\,x_{Cr} + 2.8665\,x_{Fe} + 3.1470\,x_{Mo} + x_{Cr}x_{Fe}$$
$$[0.0029496 - 0.022928(x_{Cr} - x_{Fe})] + x_{Fe}x_{Mo}\,0.06507 + x_{Fe}x_{Ni}[0.0778 + \quad (5.12)$$
$$0.0743(x_{Fe} - x_{Ni})]$$

Using the concentration values determined by APT (Table 5.1), the lattice parameter of bcc Fe matrix is calculated to be 2.8852 ± 0.0044 A, which is in a good agreement with the experimentally determined value of (2.8827 ± 0.0011 A) by ND.

In the case of the β' phase, the volume V of N unit cells of non-stoichiometric NiAl can be given by [161]:

$$V = (N - x_{Ni}n_i)\Omega_{Ni} + (N - x_{Al}n_i)\Omega_{Al} + n_i\Omega_i = Na^3 \quad (5.13)$$

where x_{Ni} is the fraction of atom i located in the Ni sites, x_{Al} the fraction of atom i located in the Al sites, n_i the number of atom i in the NiAl lattice, Ω_{Ni}, Ω_{Al}, and Ω_i are the atomic volume of Ni, Al, atom i in NiAl, respectively. The atomic fraction of atom i is given by:

$$x_i = \frac{n_i}{2N} \tag{5.14}$$

Differentiating V in Eq. 5.13 and x_i in Eq. 5.14, with respect to n_i gives:

$$\Omega_i - x_{Al}\Omega_{Al} - x_{Ni}\Omega_{Ni} = \frac{3}{2}a^2\frac{da}{dx_i} \tag{5.15}$$

Kitabjian et al. [161] determined the values of Ω_{Al} and Ω_{Ni} to be 0.0134 nm^3 and 0.0106 nm^3, respectively. Therefore, the atomic volume of atom i (Fe, Cr, Mo) in NiAl can be calculated by Eq. 5.15 from the available literature data [162-164]. Table 5.3 listed all the calculated results. With the assumptions that the atomic volume of a constituent is independent of the site it occupies, and there is no vacancy in the B2 phase, the lattice parameter of B2 NiAl can be calculated to be 2.8747 ± 0.0034 A by:

$$a^3 = 2\left(x_{Al}\Omega_{Al} + x_{Ni}\Omega_{Ni} + x_{Fe}\Omega_{Fe} + x_{Cr}\Omega_{Cr} + x_{Mo}\Omega_{Mo}\right) \tag{5.16}$$

The modeled result is also in good accordance with the experimentally determined value (2.8752 ± 0.0004 A).

5.7 Discussions

The results shown in Sections 5.3 and 5.4 revealed that the value of the lattice parameters of β' precipitates measured by ND is in good agreement with that of XRD. The comparison of these two methods to accurately measure the lattice parameters had been reported in the study of Ni-based superalloys [128]. It is generally believed that the lattice misfit is connected with high-resolution diffraction which is normally better measured by synchrotron and X-ray diffraction instruments [131]. One of the advantages of using ND was reported to be the intensity of superlattice reflection is stronger than that of XRD [128]. This

is due to the intensity of superlattice depends on the difference in the scattering between Ni and Al atoms, and their difference is quite small in the case of XRD [128]. As shown in Figure 5.2, the neutron diffraction data provided a higher reflection intensity {100} reflection than that of XRD, which is consistent with the previous studies [128, 131, 165]. The intensity ratio between (100) and (110) reflections in XRD can be calculated by applying the same approach shown in Section 5.3. Using the form factors of different elements reported in the literature [166], this ratio was calculated to be ~2%, which is much lower than the value of ND. This finding, along with the previous results on the Ni-based superalloys [128, 131, 165], suggests that ND may have advantages for the lattice parameter measurement in some cases.

With the measured lattice parameters at different temperatures, thermal-expansion coefficient (α) of β phase can be determined and is slightly higher than that of the pure bcc Fe. In a multi-component system, α is a complicated function of thermal and elastic properties of the alloying elements [167]. The slightly higher measured value of α may be explained by the existence of ~10% of Al in the matrix, which has a higher thermal-expansion coefficient of 2.31×10^{-5} K^{-1} [153]. In addition, it is reported that grain boundaries have an enhanced effect on the thermal expansion coefficient due to their excess volume [168], especially in the nano-crystalline materials, which contains a high amount of grain boundaries. However, the grain size of the studied alloy was previously reported to be ~100 μm [137]. Under these circumstances, the grain boundary effect should not play an important role. Nevertheless, one could still justify the measured α of the matrix, based on the reported α of different steels varying from $1.1 \sim 1.7\times 10^{-5}$ K^{-1} [153]. On the contrary, the α of β' phase is much higher than

the reported value. The APT results shows that the β' phase contains 10.6% of Fe. As the α of Fe is lower than that of β'. The composition does not appear to be the dominant factor contributing to the discrepancy. A higher value of thermal-expansion coefficient of the spherical coherent precipitates was previously reported in several alloy systems [169]. The rationale lies in that the temperature derivative of the matrix-inclusion contact stress for nearly equal values of the matrix and inclusion lattice parameters, although the amounts of deviation were found to vary in different alloy systems [169].

The slightly higher α of the β' phase results in a decrease of the lattice misfit between the β and β' phases as increasing the temperatures. Similar to the Ni-based superalloy system, the coarsening rate is expected to be affected by the lattice misfit at the temperature concerned [170]. Calderon [19, 135, 146] investigated this relationship in a Fe-Al-Ni-Mo alloy system. It was reported [19, 135, 146] that the lowest initial lattice misfit gives rise to the slowest coarsening rate of the precipitates. As shown in Figure 5.1, this may be one of the reasons which contribute to the fact that the creep resistance of the studied alloy is superior to the other candidate materials.

The results in Section 5.6 shows that the lattice parameters of both the β and β' phases can be modeled reasonably accurately as a function of alloy compositions. This approach involves the determination of the elemental partitioning and their occupancy in the lattice. The first parameter can be measured experimentally by APT, and the second can be predicted by first-principles calculations. It is observed that the deviations of the predicted lattice

parameters are larger than that of experimentally determined. In the case of APT, the standard error (σ) of the concentration estimated by APT is ~ 0.03%, given by $\sigma = \sqrt{C(1-C)/N}$, where C is the concentration, and N is the total number of atoms in the measured volume. It clearly show that the standard error decreases as increasing the number of collected ions. In order to obtain a more accurate modeled lattice parameter, it needs to collect more ions during the APT experiments. In addition, the measured volume by APT (~ 1×10^{-3} μm^3) is much smaller as compared to that by ND. This extreme localization of the zone analyzed may not give a statistically accurate composition of the bulk material, especially for those that are not perfectly homogeneous. Similar findings were reported in the Ni-based superalloys [171]. The errors of other factors, including those from the first-principles calculation [152], models to predict the lattice parameters of Fe [160] and NiAl [161], have been discussed individually elsewhere. Nevertheless, the estimation of the lattice misfit in a given alloy can be still predicted reasonably accurately by the approach described above. The calculation of the lattice misfit can be subsequently achieved. This will provide an efficient guideline for the selection of the alloy which may exhibit promising creep resistance. The modeling of the lattice parameters will significantly accelerate the alloy design process of Fe based β/β' alloys.

5.8 Summary

In this Chapter, neutron diffraction was utilized to measure the lattice parameters of a NiAl-type precipitate strengthened ferritic steel as a function of temperatures. Single peak fitting and a peak deconvolution approach were utilized to separate the overlapping

fundamental reflections. The values of the lattice parameters can be subsequently measured. The results at room temperature were validated by the results of synchrotron high energy X-ray diffraction. The intensity of the superlattice reflection in the case of XRD was found to be weaker. ND was more suited for the purpose of measuring the lattice misfit in the current studied alloy system. A negative misfit value of ~ 0.3% was determined at room temperature. The slightly higher thermal expansion coefficient of the precipitate phase results in the decrease of the absolute value of the lattice misfit.

With the experimentally determined phase compositions by APT, models were proposed to predict the lattice parameters as a function of the phase compositions at room temperature. The modeled results are in very good accordance with those determined experimentally by ND. The calculation of the lattice misfit of a given alloy can be therefore achieved. This model will provide an efficient guideline for the selection of the alloy which may exhibit promising creep resistance. The modeling of the lattice parameters for a given alloy system will significantly accelerate the alloy design process of Fe based β/β' alloys.

CHAPTER 6 EFFECTS OF AL ON THE MICROSTRUCTURE AND DUCTILITY AT ROOM TEMPERATURE

6.1 Introduction

Creep resistance is one of the most important properties of materials for high-temperature structural applications. Consequently, several studies on β'-strengthened ferritic steels have focused on the creep behavior and related microstructural characterizations [17-18, 20, 22-24, 172]. However, there is no systematic study of the ductility of these materials. Only recently, Stallybrass and Sauthoff [24] reported that the Fe-Ni-Al-Cr alloys with a high volume fraction (0.37) of β' exhibited a bending ductility less than 1.5% even at temperatures higher than 1,000 °C. The reason for this low ductility of these materials has not been fully understood. Nevertheless, the steam turbine materials generally require a tensile ductility of about 10% at room temperature for sufficient workability in as-cast and subsequent fabrication stages.

In two-phase materials, such as Fe-based β/β' alloys, it is expected that many properties will be closely related to the intrinsic properties of these two phases. Therefore, we present a brief summary of the room temperature ductility of β and β', as reported in literature, particularly the influence of chemistry.

The effects of various alloying elements on the ductility and toughness of the β phase have been reported in literature [34, 48, 173]. Leslie [34] has summarized the effect of many

alloying elements on the strength, ductility, and toughness of the β solid solution. Specifically, it has been established that Co, Ni, Rh, Ir, and Pt increase toughness (decrease notch-impact transition temperature), while Si and P decrease toughness (increase notch-impact transition temperature) and also to a lesser extent by Cr, Mn, and Re. In this regard, Al behaves analogously to Si in the β solid solution. Recently, Herrmann et al [48] reported the tensile strength and ductility of Fe-(4 to 18) Al (atomic percent) solid solution at room temperature. With increasing the Al content, an increase in the strength and a concomitant decrease in the ductility were observed. Furthermore, α-Fe is known to exhibit cleavage fracture, particularly at low temperatures, due to the limited number of active slip systems.

Pugh [37] proposed that the ductility of pure metals is related to the ratio of bulk modulus to shear modulus (K/G). The rationale is that with decreasing K/G, more energy is stored as dilation rather than shear deformation. In fact, the measurement of polycrystalline elastic constants of β solid solutions show a marked increase in K/G when Ni and Pt are added to Fe, leading to an increase in fracture toughness. On the other hand, K/G slightly decreases when Cr and Mn are added, leading to decrease in fracture toughness. However, such a simplistic correlation fail in many cases [34]. A more fundamental hypothesis is that the elements, which increase ductility, also change bonding so as to increase the cross slip of screw dislocations in α-Fe [34].

Polycrystalline NiAl with the $B2$ structure exhibits no tensile ductility at room temperature due to the lack of five independent slip systems to satisfy the von Mises'

criterion for the polycrystalline plasticity [74]. Like many BCC metals and *B*2 aluminides, NiAl exhibits cleavage fracture. However, the cleavage plane is not well defined [174-175]. It has been observed that in *B*2 NiAl, fracture of {511} transient planes may proceed before cleavage on {110} planes [174-175]. Darolia et al. [175] reported that small additions of Fe, Ga, and Mo significantly improve the tensile ductility, but Fe is the most effective. For example, NiAl along <110> has a tensile ductility of only 0.8%, but with the addition of 0.25 at.% Fe (substituting for Al in NiAl), the tensile ductility increases to 5.9% [98]. In another study, Field et al. [87] reported that the addition of Cr promotes the activation of the <111> slip system. Rachinger et al. [99, 176] suggested that Cr, Mn, and Fe lower the ordering energy of NiAl and favor <100> slip, but this argument was disputed by Cotton et. al [177]. Small additions of Mo were also reported to increase the ductility of polycrystalline NiAl at room temperature [96], while Hahn and Vedula [74] demonstrated that small deviations from the stoichiometric composition make NiAl even more brittle at low temperatures.

Based on the available literature, it is implicit that the dissolved Al in the β solid solution, and the volume fraction and stoichiometry of the NiAl precipitates are expected to be the major factors controlling the ductility of β/β' alloys. To investigate these factors, we have carried out a systematic study. Specifically, six β/β' (FBB) alloys with the nominal compositions of Fe-xAl-10Ni-10Cr-3.4Mo-0.25Zr-0.005B (x = 3 - 10 wt.%) were fabricated to investigate the effects of Al on the phase transformation, microstructure, partitioning behavior of alloying elements, precipitate volume fraction, and bending ductility at room temperature [Note that all the compositions are in weight percent throughout this Chapter,

unless specified otherwise]. An attempt was made to improve the ductility of the NiAl-strengthened ferritic steels by optimizing the Al concentration.

6.2 Experimental

The alloys were prepared by the approach described in Section 3.2 of Chapter 3. From the heat-treated rods, strips with a size of 19.05 mm × 3.17 mm × 0.76 mm for three-point-bending tests were cut by electron discharge machining (EDM), and then tested at a strain rate of 2×10^{-4} s^{-1} at room temperature. The fracture surfaces were investigated by scanning electron microscopy (SEM) to identify the fracture mechanisms. A differential scanning calorimeter (DSC), NETZSCH 404C, was used to study the phase transformation in model alloys. A small piece of sample with a mass of about 50 mg was measured in an Al_2O_3 crucible under an argon atmosphere at a constant heating rate of 40 K/min. from 20 to 1,500 °C.

To characterize the microstructure of prototype alloys, both transmission electron microscopy (TEM) and analytical electron microscopy (AEM) techniques were conducted at Northwester University. A HITACHI-8100 TEM and HITACHI HF-2000 AEM, both operating at 200 kV, were used. Thin foils were prepared by a Fischione dual jet polisher. The AEM is equipped with an ultrathin window (ATW) Link energy dispersive X-ray (EDX) detector. The take-off angle for the X-ray detector was 68˚. The X-ray collection time was between 300 and 500 s, and the electron probe size was about 10 nm. Care was taken to avoid a two-beam condition in order to minimize electron-channeling effects [139]. The

background-subtracted integrated intensities of EDX spectra were converted to compositions. The details may be found elsewhere [140, 178]. The elemental partitioning data of FBB-13 was determined by atom probe tomography (APT), details of which has been described in Section 5.2, Chapter 5.

6.3 Phase Transformation

Preliminary DSC studies on the as-cast materials revealed that there was no strong peak observed around the solvus temperature of NiAl due to the formation of a limited amount of NiAl phase. Therefore, it was not able to determine the phase transition temperatures, especially the solvus temperature of NiAl precipitates. Consequently, aged materials were used for DSC studies to form a sufficient amount of NiAl precipitates. The DSC heating curves of the alloys are compared in Figure 6.1a. All curves show that the transformation from β' to β starts at a temperature [$T_{\beta'(NiAl)}$] of about 750 °C and completes at a temperature (T_{β}) around 1,050 °C. Therefore, the solution-treatment temperature (1,200 °C) used in this study was adequate. There is another exothermic transition peak at a temperature higher than $T_{\beta'(NiAl)}$ for the alloys containing less Al (FBB-8 and FBB-12). This feature is most likely to be the FeAl phase separation (also a β' phase) inside the NiAl particles, which was suggested by the investigation of an Al-rich Fe-23.2Al-4.1Ni alloy system by Liu et al [179]. They revealed that two kinds of *B*2 phases (NiAl and FeAl) coexist in a Fe-Ni-Al system when the as-quenched alloy was aged at a temperature around 725 °C. In other words, this separation depends on the alloy composition, as this transition peak was not observed in the alloys with higher Al contents (FBB-3 and FBB-7). To determine whether the formation

of a possible FeAl phase occurred during the aging or solution-treatment process, the DSC studies were also carried out on the solution-treated alloys FBB-3 and FBB-8. A comparison of the DSC curves in the solution-treated and aged conditions is shown in Figure 6.1b. As can be seen, the DSC curves of FBB-3 did not reveal the FeAl peak in neither solution-treated nor aged condition. The FeAl phase peak was not observed in the solution-treated but in the aged FBB-8, which suggests that the formation of FeAl phase most likely occurred during the aging process.

In Figure 6.1a, the endothermic peak at a temperature of ~650˚C is most likely the solvus temperature of the secondary NiAl precipitates [24]. However, the ferromagnetic to paramagnetic transition temperature (T_c) of the Fe-Al-Ni system was reported [180] to be also between 600-700˚C. Therefore, further studies will need to be carried out to verify this phase transition. Another small endothermic peak (T_τ) is observed in all alloys except FBB-12 around 1,250˚C, i.e., between T_β and the melting temperatures (T_m). Marcon et al. reported that depending on the composition, the γ-Fe loop exists in the isoplethal section from the Fe corner to NiAl in the Fe-Ni-Al system [180]. Therefore, this reveals a possibility of a small amount of α-Fe transforming to γ-Fe. However, it was reported that [7] this transformation can be suppressed by the small addition of Al (2.5 at.%) in the Fe-NiAl pseudo-binary phase diagram. The difference might be due to the much complex alloy systems in our study. Also, as indicated in Figure 6.1, T_m shows a slight decrease with increasing the Al content.

6.4 Microstructure Characterization

Three representative alloys with high (FBB-3), medium (FBB-8), and low (FBB-12) amounts of Al additions were selected to conduct the TEM study. Figure 6.2 shows the bright field (BF)-TEM micrographs of these alloys. In all cases, a mixture of cuboidal (larger) and spherical (smaller) β' precipitates are observed. The average diameter lies between 130 and 150 nm. In addition, ultrafine β' precipitates with a diameter of about 20 nm are also observed. It is believed that they have precipitated from the β matrix during the air cooling from 700 °C, similar to that reported in an earlier work [24].

The evidence of the phase separation (by nucleation and growth processes) within the β'(NiAl) phase may also be observed. For example, in Figure 6.2b, many nano-scale (10 - 15 nm in diameter) domains in several β' precipitates are seen. These dark domains inside β' particles have formed during aging at 700 ˚C, as described in the previous section. Depending on the alloy composition, the dark domains inside β' can be either an FeAl-type *B*2 phase [179] or a disordered (α-Fe) phase due to the precipitation of the excessive Fe in β'(NiAl) during aging at 700 ˚C. It should be noted that *B*2-FeAl and *B*2-NiAl form a continuous solid solution at high temperatures. In this study, we have noticed that the alloy composition has a strong influence on the amount of the FeAl-type *B*2 phase, as it was observed in only few β' particles in FBB-3.

6.5 Partitioning Behavior of the Alloying Elements

The compositions of the β and β' phases in FBB-3, FBB-8, and FBB-12 were

determined by analyzing 25 EDX spectra of each phase collected in AEM. Representative EDX spectra of β and β' phases in FBB-8 are shown in Figure 6.3. Following our earlier work on the quantitative analysis of EDX spectra [140, 178], the average compositions of β and β' in three alloys are summarized in Table 6.1. The partitioning ratio, defined as the ratio of the element fraction in the Fe matrix to the precipitates in at.%, of Ni and Al is presented in Figure 6.4.

All alloys show the evidence of Fe partitioning to β' precipitates. In Table 6.1, it is seen that β' may contain up to 14 at.% Fe as in FBB-8. This is consistent with the results of Bradley [14] who found that β' may dissolve up to 20 at.% Fe at 750 ˚C. The Cr content in β' is about 1 at.%. Earlier studies on bulk NiAl have shown that the solubility of Cr in NiAl is strongly temperature dependent, ranging from less than 8 at. % at 1,290 ˚C [181], less than 2 at.% at 1,043 ˚C [87], to less than 0.2 at.% at 550 ˚C [182]. Therefore, our data of 1.1 to 1.5 at.% Cr in β' is in good agreement with the published data. Due to rather low partitioning of Cr to β', the β matrix is not significantly depleted of Cr, which helps retain its corrosion and oxidation resistance at high temperatures.

As earlier studies have demonstrated [34], Ni in the β matrix is beneficial for improving its ductility and toughness. Table 6.1 suggests that by decreasing the Al content in the alloy, the Ni content in the β matrix increases from 2 at.% in FBB-3 to 3.3 at.% in FBB-12. The partitioning of Mo to β' is almost negligible, therefore it exerts significant influence in dilating the lattice of the β matrix, leading to a reduction in the lattice misfit [19].

6.6 Volume Fraction of β'

With the knowledge of the compositions of β and β' phases, the volume fraction ($V_{\beta'}$) of the latter can be estimated using the lever rule:

$$V_{\beta'} = \frac{C_0 - C_\beta}{C_{\beta'} - C_\beta} \tag{6.1}$$

where C_0, C_β, and $C_{\beta'}$ are the compositions of the alloy, β matrix, and β' precipitate, respectively. Considering Al, Cr, and Ni, we obtain $V_{\beta'}$ = 0.179, 0.178, and 0.135 for FBB-3, FBB-8, and FBB-12, respectively. In the AEM composition analysis, we have neglected the ultrafine precipitates and considered only 25 EDX spectra of β and β' phases. Further AEM data as well as atom probe tomography (to include ultrafine precipitates) may be needed for the accurate estimation of $V_{\beta'}$.

6.7 Three-Point-Bending Experiment and Fracture Behavior

Three-point-bending tests were performed to assess the ductility of model alloys. In this test, the bending flexural strain of a strip is calculated as [183]

$$\varepsilon_f = 6Dt/L^2 \tag{6.2}$$

where ε_f is the strain on the outer surface, D is the maximum deflection at the center of the strip (mm), t is the thickness (mm), and L is the support span (mm). The calculated bending ductility and measured hardness are shown in Figure 6.5. Reducing the Al concentration from 10 % to 3 % improves the failure bending strain from 0.5% to more than 5%. The hardness decreases slightly when the Al content is reduced from 10 % to 6.5 % below which the hardness drops significantly.

The SEM fractographs of FBB-3, FBB-8, and FBB-9 are shown in Figures 6.6a-c. The flat facets in all cases exhibit river patterns, which are the characteristic feature of a brittle cleavage fracture. The sharp drop in hardness and a concomitant increase in ductility from FBB-12 (5 % Al) to FBB-13 (3 %Al) suggest a possible change of fracture mode. Figure 6.6d shows the bending fracture surface of the alloy FBB-13. It exhibits a mixture fracture mode of cleavage and ductile. The representative ductile fracture is shown as inset in Figure 6.6d.

6.8 Discussions

Following the brief discussion in Introduction, it is implicit that many properties of β/β' alloys are expected to be governed by the intrinsic properties of the constituent phases. Specifically, the bulk NiAl exhibits only a limited ductility, and that of the α-Fe is strongly influenced by alloying elements, such as Al. In addition, it has been reported that the ductility of the polycrystalline alloys decreases as the volume fraction of the strengthening particles increases [49].

Our TEM and AEM studies show that the microstructures of model alloys consist of the β matrix and spherical/cuboidal β' strengthening precipitates. In this class of alloys, we find that two major factors governing the ductility: viz. the volume fraction of β' and the Al-content in the α-Fe matrix. In model alloys containing 4 to 10 % Al, the volume fraction of β' lies in the range of 0.13 to 0.18. When the Al content is reduced while keeping Ni-content the same, three microstructural changes take place simultaneously: (i) the volume

fraction of β' decreases, (ii) the Al content in the β matrix decreases, and (iii) the Ni content in the β matrix slightly increases. It is believed that due to these factors, FBB-13 (3 % Al) exhibits the most improved ductility. To verify this, the elemental partitioning data of FBB-13 was determined by APT. The results along with the AEM data were presented in Table 6.1. The precipitate volume fraction of FBB-13 was estimated to be ~7% by a thermodynamic model [184]. From the APT results, it clearly shows that the Al solubility is 1.3 at.%, which is the lowest among all the alloys. Therefore, the improvement in ductility is related to the decrease in both the precipitate volume fraction and Al solubility in Fe. However, among these two factors, which one is decisive to the ductility is not clear at this stage, as both of them change when increasing the Al additions. To understand each of their individual effects, we need to control one of those factors at a constant value, while changing the other. The thermodynamic model [184] being developed will be able to predict the elemental partitioning and precipitate volume fraction. By the guidance of this model, alloys will be fabricated according to the calculation results and investigate the individual effects of each factor in the future study.

Although the volume fraction of β' decreases moderately from FBB-3 to FBB-12, the Al content in the β matrix decreases significantly from 18.6 at.% in FBB-3 to 4.7 at.% in FBB-12. In their study, Herrmann et al. [48] reported that the presence of DO_3–type chemical order may also lower the ductility of Fe-Al alloys. However, in our model alloys, the presence of DO_3–type could not be seen in TEM diffraction patterns, thus its influence on ductility is ruled out. Among other alloying elements in the β matrix, the dissolved Cr and Mo

may also cause a decrease in the ductility and toughness of Fe [34]. Nevertheless, this can not explain the ductility differences for FBB-3 to FBB-12 alloys, as AEM results reveal that the dissolved Cr and Mo in the β matrix are almost the same. In addition, AEM results also reveal that the Al- and Ni-contents in the β matrix have decreased and increased, respectively, from FBB-3 to FBB-12. Therefore, both these factors have contributed to the improvement in the ductility of FBB-12.

Several studies [98, 175, 185] have shown that the dissolved Fe modifies the preferred slip vector of polycrystalline NiAl, and thus improves the ductility. Also, Kovalev et al.s' study [186] found that the addition of 2 at.% Fe decreases the ductile-brittle transition temperature of NiAl by about 200°C. Our AEM results show that the Fe content in β' precipitates varies from 15.3 % in FBB-3 to 18.1 % in FBB-8, which indicates that the softening effects in FBB-8 may be higher than in FBB-3. The AEM results also reveal the chemistry of the β' has changed from Al-rich in FBB-3 to slightly Ni-rich in FBB-12 due to a reduction in the Al content in the alloy. It has already been shown [99] that a small deviation from the stoichiometric composition makes NiAl even more brittle at low temperatures. Due to insignificant partitioning of Cr and Mo to β', the ductility of the β' precipitates in FBB-8 should be the highest. However, the ductility of all model alloys with the Al content higher than 4% is nearly the same, implying that the intrinsic ductility of the β' precipitates is nearly the same. Therefore, the two major factors governing the poor ductility of the β'-strengthened ferritic steels are the volume fraction of NiAl-type precipitates and the Al-content in the α-Fe matrix.

It should be noted that the ultrafine secondary NiAl precipitates observed by TEM may also contribute to the loss of ductility. For example, Kakehi [144] observed ultrafine precipitates (γ') in an experimental Ni-based superalloy, causing a decrease in the net width of the matrix channels irrespective of primary precipitates. This in turn causes brittleness although they exert a strong influence on the creep resistance. In this study, the ultrafine β' secondary precipitates were observed in FBB-3, while FBB-8 and FBB-12 mainly consist of primary β' particles. This feature might have contributed to the poor bending ductility of FBB-3 and 7.

Although the ductility of β'-strengthened ferritic steels can be improved by reducing the Al content, concomitantly the hardness decreases, as shown in Figure 6.5. This is due to the decrease in the volume fraction of β', and also due to the decrease in solid solution strengthening of the β matrix as the dissolved Al is reduced. A major objective of this research is to design a creep-resistant ferritic steel with a decent ductility at room temperature for sufficient fabricability. A certain amount of Al is needed for the formation of sufficient β' precipitates for both the creep and oxidation resistance. Combining the ductility and hardness of the model alloys shown in Figure 6.5, an optimal balance appears to be at about 6.5 % Al. The tensile ductility of the alloy with 6.5% Al can be further improved to more than 10% by thermal mechanical treatments, which will be discussed elsewhere [187].

6.9 Summary

To demonstrate the composition-microstructure-property relationships, we have

investigated a class of ferritic Fe-based alloys strengthened by NiAl-type precipitates. The phase transformation and microstructural characterizations of several model alloys are performed using DSC, TEM, and AEM techniques. We have also investigated their hardness, bending ductility, and fracture behavior.

The DSC results show a transition peak between the transformation temperatures of β' to β in the alloys with low Al contents. The AEM analyses verify that this transformation is most likely to be the FeAl phase separation inside the β' (NiAl) precipitates. The TEM study exhibits that the microstructure of the model alloys consists of β Fe matrix and β' (NiAl-type) precipitates with a diameter between 130 and 150 nm. The volume fraction of β' lies in the range of 0.07 to 0.18 for the studied alloys.

The three-point-bending test reveals that the model alloys, containing 4 to 10 % Al, exhibit very limited ductility (< 2%) at room temperature, and their fracture mode is predominantly cleavage type. Two major factors governing the poor ductility are the volume fraction of NiAl-type precipitates and the Al content in the α-Fe matrix. Among these two factors, it is necessary to undertake further studies with alloys along a particular tie-line by keeping the volume fraction of β' constant but varying Al-content. This study may help establish the dominance of either of these two factors. A bending ductility of more than 5% can be achieved by lowering the Al concentration in alloys to 3 %. However, the alloy containing about 6.5 % Al is found to have an optimal combination of hardness and ductility.

CHAPTER 7 EFFECTS OF PRECIPITATE MICROSTRUCTURE AND HOT ROLLING ON THE ROOM TEMPERATURE DUCTILITY

7.1 Introduction

As mentioned in Chapter 6, the recent development of these materials [24, 137] revealed that poor ductility at room temperature is a critical issue restricting their applications. For example, Stallybrass and Sauthoff reported [24] that the Fe-Ni-Al-Cr alloy system with a high volume fraction (0.37) of β' exhibited a bending ductility of near zero at room temperature. However, the steam turbine materials generally require a tensile ductility of ~ 10% at room temperature for sufficient workability in the as-cast condition and subsequent fabrication stages. The reasons for this kind of poor ductility have not been well investigated.

Since the ferritic alloys without β' precipitates exhibit a tensile ductility of up to 25% at room temperature [188], the reduction of the ductility most likely comes from the formation of β' precipitates and/or the compositional change associated with the partitioning of the alloying elements. The effects of precipitates microstructures (volume fraction, particle size, and inter-particle spacing) on the ductility of several precipitate-hardened alloys have been previously reported [54, 57, 65, 72, 189-193]. However, general agreement was not established among different materials. The results were strongly dependent on the properties of the matrix material [192], fracture mode after deformation [190], or some microstructural features of the precipitates [65]. How the β' precipitate microstructure affects the ductility of NiAl-strengthened ferritic steels has not been investigated.

Another possible factor contributing to the poor ductility, the compositional change of both the β matrix and β' precipitates by alloying, also needs to be carefully addressed. The influences of several alloying elements on the ductility of Fe have been investigated in previous studies [34, 48, 173, 194], respectively. Among the alloying elements included in the alloys of the current study, Ni was reported to have a softening effect on Fe and lower its cleavage transition temperature [173, 194]. On the contrary, Al decreases the ductility of Fe with increasing its addition [48]. Alloying elements were also reported to affect the ductility of polycrystalline NiAl [73, 80]. It is well known that the tensile ductility of NiAl at room temperature was low, ranging from 0 to a maximum of ~ 4% [76, 81, 86]. Since NiAl deforms predominantly by <100> slip on {110} type planes, there are only three independent slip systems are available, which is less than the five independent deformation modes considered necessary for extensive, uniform, crack free deformation [85]. Small addition of Mo and Fe were found to increase the ductility of NiAl by promoting additional slip systems [93]. Although the effects of alloying on the ductility of α-Fe and NiAl have been investigated individually, the compositions of the β' NiAl precipitates in the α-Fe matrix have not been determined due to its nano-scaled size. Therefore, the compositional effects on the ductility of the composite alloys have not been clearly identified.

The objective of the study in this Chapter is to investigate the effects of the β' precipitate volume fraction, size and inter-particle spacing, along with the compositions of both β and β', on the room temperature ductility. The base alloy composition in the current study is one recently developed alloy, FBB-8 [Fe-12.7Al-9Ni-10.2Cr-1.9Mo, Note that all the compositions are in atomic percent (at.%) throughout this Chapter, unless specified otherwise], which exhibited

promising creep resistance but limited ductility [137, 148]. This alloy was aged for different time periods to study the effects of the precipitate size and inter-particle spacing. Five other alloys with different β' precipitate volume fractions (V_f) were carefully designed to study the effects of V_f and elemental partitioning. The results of these investigations are subsequently discussed to gain insights into the dominant microstructural features associated with the ductility. Furthermore, hot rolling was used as an attempt to improve the ductility of the studied alloys with controlled grain size.

7.2 Experimental

7.2.1 Fabrication

The alloys were fabricated by the approach described in Section 3.2 in Chapter 3. The nominal compositions (at.%) are listed in Table 7.1. In alloys FBB-3 through FBB-19, various amounts of Al and Ni were added to form different β' volume fractions. The actual composition of the as-cast FBB-8 was determined by wet chemical analyses. The results summarized in Table 7.1 verified that the fabricated alloys exhibit the same composition as the nominal, indicating that the studied alloys can be fabricated accurately by the method described above.

7.2.2 Heat treatment and thermo-mechanical treatment

The ingots were subsequently cut into rods with a length of 20 mm by electrical discharge machining (EDM). They were solution-treated at 1,200°C for 30 min. in evacuated and sealed quartz tubes, followed by air cooling, and then aged at 700°C for 100 h and

air-cooled. In order to study the effects of different β' precipitate sizes, samples of alloy FBB-8 were also aged at 700°C for 500 and 1,000 h, respectively. For the grain size refinement study, FBB-8 was hot rolled in air at 750°C for 80% reduction in thickness, followed by recrystallization at 850°C for one hour.

7.2.3 Microstructure characterization

To characterize the microstructure of the precipitates, a combination of atom probe tomography (APT), transmission electron microscopy (TEM), and ultra small angle x-ray scattering (USAXS) techniques were utilized. The Imago Scientific Instruments Corporation local electrode atom probe (LEAP®) experiments were performed to quantify the compositions of both the β matrix and β' precipitates. The compositions of these phases can be determined by counting the number of ions collected from each phase. The β' volume fraction can be estimated by lever rule based on the obtained compositions. APT was conducted with a pulse repetition rate of 200 kHz, a voltage pulse fraction of 0.2, and a specimen temperature of 60 K. Due to the limitation of the analysis volume, it is not easy to determine the average size of β' accurately by APT. TEM was conducted to quantify the β' precipitate size in the alloy FBB-8 aged for different time periods. A HITACHI-8100 TEM operating at 200 kV was used. Thin foils were prepared by a Fischione dual jet polisher. As a complementary technique for TEM, USAXS was utilized to measure the inter-particle spacing of selected bulk materials. USAXS was performed using the synchrotron source at the 32 ID beam line of the Advanced Photon Source (APS), Argonne National Laboratory. X-rays of a 16.85 keV energy and a beam size of 1.6 × 0.8 mm were used for these experiments. The grain size of the aged materials was

measured by the optical microscopy and the grain/subgrain size of the hot-rolled materials was determined by electron backscatter diffraction (EBSD). The EBSD mapping was performed on a Philips XL 30 SEM equipped with a field emission gun (FEG) and an EDAX's TSL orientation imaging microscopy (OIM) system. The SEM was operated at 15 kV, and the orientation mapping involving automatic beam scanning was used with step sizes of 0.25 μm.

7.2.4 Mechanical Behavior

Three-point-bending tests were performed to assess the ductility of the model alloys, details of which have been presented in Section 6.7 of Chapeter 6. For the hot-rolled materials, the ductility was measured at a strain rate of 10^{-3} s^{-1} by tensile tests. The rectangular tensile test piece has a geometry of 12.7 mm in the gage length, 3.18 mm in width, and 1.27 mm in thickness. Both bending and tensile tests were performed on an Instron mechanical tester. The fracture surfaces of the bending/tension tested samples were investigated by SEM to identify the fracture modes.

7.3 Initial Microstructure and Ductility

Representative microstructures of the based material (FBB-8) in our study are shown in Figure 7.1. The average grain size is ~ 100 μm (Figure 7.1a). β' precipitates have an average diameter of ~ 130 nm (Figure 7.1b) and a spherical morphology. Figure 7.1c presents the USAXS intensity (I) versus scattering vector (Q) curves of the FBB-8 alloys aged for different lengths of time. Each curve has a peak at $Q = 1 \sim 6 \times 10^{-3}$ A^{-1}. Details regarding the quantitative analyses of the USAXS spectrum can be found in the literature [195]. Briefly, the establishment

of the peak is due to the interaction of the precipitates developed during the heat treatment. The inter-particle spacing (λ) thus can be calculated by $\lambda = 2\pi/\text{peak Q}$. The value of λ is determined to be 217 nm for the alloy aged for 100 h, which is consistent with the projected average distance between the precipitates in the TEM micrograph, as shown in Figure 7.1b (~ 210 nm). The compositions of both phases determined by APT are listed in Table 7.2. Applying the lever rule to all the elements, the β' precipitate volume fraction is estimated to be ~ 18%.

Although the compositions of each phase in different alloys vary, the distributions of the elements exhibit some similarities, as shown in the representative atom maps of the based alloy FBB-8 in Figure 7.2. The interface between the matrix and the precipitate can be clearly identified by the different concentrations of the alloying elements in each phase. As can be seen in Figures 7.2a and b, the concentrations of Ni and Al are much higher than the other elements in the precipitate, indicating that the precipitates are NiAl-type. Cr prefers to remain in the Fe matrix (Figure 7.2c), which is beneficial for the oxidation resistance of the alloy. The content of Mo in the β matrix is higher than that of β' (Figure 7.2d). As a larger atomic element than Fe, Mo helps dilate the lattice parameter of the BCC Fe, thus reducing the lattice misfit between the Fe matrix and the NiAl precipitates. This low lattice misfit will influence the coarsening behavior of the precipitates, which in turn imposes important effects on the creep resistance. The partitioning of a large amount of Fe into the β' precipitates (Figure 7.2e) may affect the ductility of the precipitate.

A bending load-deflection curve of FBB-8 has been shown in Figure 1.6a. The calculated

bending strain by Eq. (6.2) at the failure point is ~ 0.94%, which is much lower than the required ductility of ~ 10%. The flat facets of the fracture surface in Figure 1.6b exhibit river markings, characterizing a brittle cleavage fracture. Details regarding the fracture surfaces of the unrolled NiAl-strengthened ferritic steels have been presented elsewhere [137].

7.4 Precipitate Microstructure

7.4.1 Alloy FBB-8 aged for different lengths of time

Using the techniques of TEM and USAXS, the β' size and the inter-particle spacing of the alloy FBB-8 aged for different lengths of time can be determined and plotted in Figure 7.3a. Both of these two parameters increase as increasing the aging time. In alloys strengthened by spherical precipitates, the inter-particle spacing (λ) is a function of the precipitate volume fraction V_f and precipitate radius r [196]:

$$\lambda = \frac{4(1-V_f)r}{3V_f}. \tag{7.1}$$

Figure 7.3b exhibits that λ has a near linear relationship with r, suggesting that the precipitate volume fraction remains almost invariant during the aging process. This finding is consistent with a previous study [197] on a Fe-Ni-Al system, which showed that the nucleation of B2 precipitates can not be suppressed even by quenching the liquid alloy by a melt-spinning process, thus there was no formation of extra precipitates in the subsequent aging procedure. The β' volume fraction can be calculated to be ~ 20% based on the slope of the best linear fit of the data in Figure 7.3b, which is in a good agreement with the value estimated by APT (18%). This consistency verifies that the measurements of the microstructural parameters in the current study are reasonably accurate. Figure 7.3a suggests that the bending ductility of the alloy

FBB-8 does not change with increasing the aging time. In other words, the ductility is independent of both the precipitate size and inter-particle spacing in the current studied range.

7.4.2 Alloys with different β' precipitate volume fractions

Table 7.2 summarizes the compositions of β and β' in all the alloys determined by APT, along with the β' volume fractions estimated by lever rule. All these data are in a very good agreement with the previous prediction of a thermodynamic model [184]. The bending ductility, shown in Figure 7.4, increases from less than 1% to more than 5% when decreasing the precipitate volume fraction from 37.5% (FBB-19) to 7.3% (FBB-13). When we plot the ductility as a function of the elemental solubility in the β matrix, shown in Figure 7.5, it is found that the ductility improvement appears strongly related to the reduction of the Al solubility. In addition, Figure 7.5 exhibits that the ductility increases consistently with increasing the Ni solubility in β. Due to the relatively smaller absolute value, the effect of Ni solubility in β does not appear as obvious as that of Al. Nevertheless, the increase from 1.5% in FBB-19 to 3.0% in FBB-13 represents a marked difference of ~ 50%. In view of the solubility of Mo, a consistent trend of the relationship with the ductility was not found, although its value varies slightly in different alloys. The solubility of Cr remains almost a constant (~ 12%). Consequently, the solubility of Mo and Cr are not considered as the major factors contributing to the ductility difference.

As shown in Table 7.2, the elemental partitioning in the β' is not able to be clearly related to the ductility. One characteristic should be mentioned is that there is a pronounced amount of

Fe partitioning into β' in all the alloys, varying from 10.4% in FBB-19 to 18.1% in FBB-13. Several studies [98, 175, 185] have shown that the dissolved Fe modifies the preferred slip vector of polycrystalline NiAl, and thus improves the ductility. Furthermore, a study by Kovalev et al. [186] found that the addition of 2 at.% Fe decreases the ductile-brittle transition temperature of NiAl by ~ 200 °C.

7.5 Hot Rolling

The microstructure of the hot-rolled material after recrystallization at high magnification is shown in Figure 7.6a. The average grain size decreases from ~ 100 μm (Figure 7.1a) in the unrolled material to ~ 1 μm after rolling. However, it should be noted that the high angle grain boundaries were not clearly visualized from the SEM image, which suggests that the refined grains may be substructures inside a large grain. Figure 7.6b shows an EBSD map of three elongated grains in the hot-rolled FBB-8. The inset gives different colors that represent the crystallographic direction of the local grains normal to the rolling direction. The thicker lines are high angle boundaries with a misorientation > 15°, whereas the thinner lines are low angle boundaries with misorienatition < 15°. The fraction of low angle boundaries was quantified to be ~ 88%, indicating that most of the refined structures with a size of ~ 1 μm are in fact the subgrains inside one grain.

The bending tests of hot-rolled FBB-8 revealed its ductility is higher than 5%. Due to the maximum measurable bending ductility of the current experimental set-up is 5%, tensile tests were conducted instead. The tensile ductility of the hot-rolled FBB-8 is ~ 10%, as shown

in Figure 7.7a, representing a significant improvement as compared to that of the unrolled material. The fracture surface in Figure 7.7b exhibits a mixture mode of cleavage and ductile rupture. A higher magnification image shown in Figure 7.7c exhibits that the precipitates can be observed in some of the dimples in the ductile rupture area, as well as the surface of the cleavage rupture area. The morphology of the β' precipitates on the fracture surface is spherical but not faceted, indicating that the precipitates were not fractured during the tension deformation.

To gain further insight into the factors contributing to the ductility improvement in the hot-rolled materials, APT was also performed. The results listed in Table 7.3 indicate that there is no significant difference between the compositions of the unrolled and hot-rolled materials. The SEM images of the APT samples in Figure 7.8 revealed that the B2 precipitates coarsened from a diameter of ~ 130 nm to ~ 250 nm during the hot-rolling process. However, as shown in Section 7.4.1, the effect of the NiAl precipitate size in this range on the ductility is almost negligible. Consequently, the formation of subgrains after hot rolling is believed to be the main factor accounting for the ductility improvement.

7.6 Discussions

The results described above clearly indicate that the ductility of the model NiAl-strengthened ferritic steels is influenced by: (1) the β' precipitate volume fraction, (2) the solubility of Al and Ni in the Fe matrix, and (3) hot rolling. The ductility was found to be independent of the β' precipitate size and inter-particle spacing in the studied range. As the

effect of the β' volume fraction on the ductility has been studied and discussed previously [137], the following discussion will focus on the effects of precipitate size/inter-particle spacing, elemental solubility in β matrix, and hot rolling. Some suggestions on the approaches to improve the ductility will be given.

7.6.1 Effects of inter-particle spacing

As shown in Figures 7.3a and b, the inter-particle spacing exhibits a linear relationship with the particle size, thus their effects on the ductility exhibit the same trend. Therefore, only the influences of inter-particle spacing will be discussed here. The ductility in precipitate strengthened materials is expected to be a function of the inter-particle spacing according to Baker's theory [72]. The critical inter-particle spacing where an optimal ductility is achieved can be calculated by [72]

$$\lambda_{crit} = \frac{\pi G b^2}{\gamma(1+\nu)} + 2r_s \tag{7.2}$$

where λ_{crit} is the critical inter-particle spacing, G the shear modulus, b the magnitude of the Burgers' vector, γ the surface energy, ν the Poisson's ratio, and r_s the precipitate radius. For the BCC Fe, the Burger's vector b = $\frac{1}{2}$**[**111**]** can be calculated to be 0.248 nm. Other parameters can be obtained from the available literature data: G = 82 GPa [198], ν = 0.29 [198], γ = 15 J/m^2 [199-201], and r_s = 65 nm. Therefore, the calculated λ_{crit} is equal to 132 nm. Baker's model [72] also proposed that there is a λ_{max}, which can be calculated by

$$\lambda_{max} = \frac{G}{\sigma_0}\left\{\left[\frac{(1+\nu)\gamma}{\pi\sigma_0}\right]^{1/2} + \left[\frac{(1+\nu)\gamma}{\pi\sigma_0} - b\right]^{1/2}\right\}^2 + 2r_s \tag{7.3}$$

where σ_0 is the lattice resistance and equal to 70 - 90 MPa for ferritic steels [202]. λ_{max} is

calculated to be 56 μm. Between λ_{crit} and λ_{max}, as predicted by Baker's model, the ductility decreases as the inter-particle spacing increases. As the calculated results show, the inter-particle spacing λ of all the aging samples are larger than λ_{crit}, but much smaller than λ_{max}. Considering the inter-particle spacing range [132 nm, 56 μm] is very large, the slight increase of the inter-particle spacing from 217 nm (aged for 100 h) to 480 nm (aged for 1,000 h) should have very limited effects on the ductility. This is in good accordance with the observation in the current study.

7.6.2 Effects of Al and Ni solubility in the Fe matrix

The most significant difference of the elemental solubility in the β matrix comes from Al, varying from 2.6% in FBB-13 to 14% in FBB-3 (Figure 7.5). The results showed that the alloy with the lowest Al solubility exhibits the optimal ductility. This trend is in a good agreement with the study conducted by Herrmann et. al [48] on the deformation behavior of Fe-(4 to 18) Al (at.%) solid solution at room temperature. The loss of the ductility is associated with the retardation of cross-slip occasioned by the onset of short range atomic order as increasing the addition of Al [203], resulting in a slower dislocation mobility [48]. However, it should be noted that the alloy FBB-19, which contains only 4.9% of Al in the matrix, still exhibits very low bending ductility (0.66%). This finding suggests that although increasing the Al solubility decreases the ductility of α-Fe, it is not the sole factor in controlling the ductility of the alloys in our study. As presented in Figure 7.4, the ductility decreases consistently as the precipitate volume fraction increases regardless of the elemental solubility and partitioning. This trend indicates that the ductility can not be significantly

improved by adjusting the elemental solubility in Fe when the precipitate volume fraction is sufficiently high.

The results in Figure 7.5 indicate that increasing the solubility of Ni in β matrix improves the ductility. As shown in Table 7.2, the solubility of Ni in the alloys with the improved ductility is ~ 3%. A previous study [173] on the effects of Ni on ferritic steels revealed that the addition of this amount of Ni not only decreases the yield strength of the steel matrix, but also increases the cleavage strength, which in turn enhances ductility. Wolff's study [194] on high Cr ferritic steels reported that Ni is associated with an increased incidence of mechanical twinning, thus increasing the brittle fracture resistance. However, twinning was not observed in the current study, thus the softening effects of Ni is believed to be the major reason contributing to the ductility improvement.

7.6.3 Effect of hot-rolling

The effect of subgrains on the mechanical properties was reported to be very similar to those of the refined grains, depending on how the recovery proceeds [204], except when they are well under 1 μm in size. As can be seen from Figure 7.6b, the average size of the subgrains in our materials is ~ 1 μm, thus the ductility improvement may be explained in terms of the Cottrell-Petch [205-206] mechanism. This theory was well established to explain the grain size refinement effects on the ductility, in light of the dependencies of fracture stress and yield stress on the grain size. Schulson [101] reported that below a certain value of grain size, the yield stress is less than the fracture stress and plastic deformation occurs before the

flow stress reaches the fracture stress, leading to a ductility increase. It should be mentioned that hot-rolling and the subsequent aging processes generally affect the dislocation density and structure, especially when the formation of submicron grains occurs [207], which in turn may pose important effects on the ductility. Further understanding of this influence will require the study of the dislocation behavior in the hot-rolled material.

7.6.4 Approaches to improve the ductility

Based on the above experimental results and discussions, the effective approaches to improve the ductility of the NiAl-strengthened alloys at room temperatures are: (i) the grain size refinement/subgrain formation, (ii) the reduction of β' precipitate volume fraction, and (iii) the decrease of the Al solubility and increase of the Ni solubility in the β matrix. The first approach can be realized by the hot rolling and following recrystallization process as described in our current study. However, the grain size refinement may increase the steady-state-creep rate [208], which is undesirable as the creep resistance is the other important requirement for the application of this material. To achieve an alloy to satisfy the microstructural features described in the latter two approaches, intensive work will need to be performed on many multi-component systems if a purely experimental approach is used. A strategy of integrating thermodynamic calculations with focused experiments will be used to efficiently locate the alloy compositions that have the potentials to show those microstructures. The development of such thermodynamic models is being conducted in another study [184]. Furthermore, as an austenite-forming element, the addition of Ni also needs to be controlled to avoid the formation of the FCC Fe, since this study focuses on developing the BCC

Fe-based alloys. As a complicated alloy design process, how to control the above parameters to strike a balance between the room temperature ductility and the creep resistance will need to be addressed in future.

7.7 Summary

This Chapter focuses on investigating the relationships between the precipitate microstructure and the room temperature ductility of a series of carefully designed NiAl-strengthened ferritic steels. Specifically, the volume fraction, size, inter-particle spacing, and composition of the NiAl precipitates were investigated by the combination of TEM, APT, and USAXS techniques. The ductility was examined by three-point bending and tensile tests. Hot-rolling was used to further improve the ductility. Based on the framework above, it was found out that ductility is closely related to the precipitate volume fraction and elemental solubility in the Fe matrix, but independent of the precipitate size and inter-particle spacing in the studied range. A ductility increase from ~1% to ~10% has been achieved by hot-rolling. The compositions of both the matrix and precipitates were found to be nearly invariant after rolling. The formation of subgrains with a size of ~1 μm revealed by electron backscatter diffraction (EBSD) is believed to contribute to the ductility improvement. Whether hot rolling will affect the creep resistance and how to balance all the required properties for steam turbine materials will need to be further studied.

CHAPTER 8 DESIGN OF ALLOY WITH BALANCED CREEP RESISTANCE AND DUCTILITY AT ROOM TEMPERATURE

8.1 Introduction

As mentioned in Chapter 1, there are two critical issues restricting the applications of NiAl-strengthened ferritic steels: poor room temperature ductility and insufficient creep resistance at temperatures higher than 600°C. As a potential material for ultra-supercritical steam turbine applications, the alloy must satisfy two major requirements: (1) a steady state creep rate of approximately 10^{-11} s^{-1} at a temperature of 760°C, and a stress level of 35 MPa, and (2) good tensile ductility at room temperature for sufficient workability in the as-cast condition and subsequent fabrication stages [1, 3]. Since the creep resistance is one of the most important properties for high temperature applications, previous research on the Fe-Al-Ni alloy system has focused on the phase stability [7, 209-210], microstructures [19, 23], and properties [20, 24] related to the creep behavior. However, the ductility issue has been rarely mentioned [24]. In particular, the microstructural features required to satisfy the combined creep and ductility properties have not been carefully identified.

The purpose of the study in this Chapter is to investigate how the creep resistance and ductility of the Fe-Ni-Al-Cr-Mo alloys relate to the alloy composition, the volume fraction of the β' B2-ordered phase, and the elemental partitioning between the β' B2 precipitate and β BCC-A2 matrix phases. It is not difficult to imagine how much intensive experimental work needs to be performed on the multi-component systems to fulfill such a goal if a purely experimental

approach is used. The strategy adopted in this study is to integrate thermodynamic calculations with focused experiments to efficiently understand such relationships and identify the alloy compositions that have the potentials. In particular, this study pursues the following procedures: (1) thermodynamic calculations are firstly conducted on several alloys based on the Fe-Ni-Al-Cr-Mo system to predict the microstructural features (phase composition and volume fraction), and validated by the experimentally measured results, (2) preliminary creep and ductility experiments are then performed on the same alloys to identify the key factors (such as the volume fraction of β' phase and elemental partitioning) which are closely related to the properties, (3) thermodynamic calculations validated in step (1) are subsequently used to quantify the β' volume fraction and the elemental partitioning as a function of alloy composition and temperature to identify the potential alloy compositions that have the balanced ductility and creep resistance; and (4) further experiments are then conducted on the potential alloys to either confirm the predictions or provide suggestions for the future studies.

8.2 Experimental

8.2.1 Fabrication and heat treatments

Five alloy ingots with different β' volume fractions were fabricated and heat-treated by the approached described in Section 3.2 of Chapter 3. The nominal compositions of all the alloys are listed in Table 8.1 (Note that all the compositions are in atomic percent throughout this chapter, unless specified otherwise). The alloy FBB-8 is the base alloy composition. From alloys FBB-9 to FBB-18, various amounts of Al and Ni are added to form different volume fractions of B2 precipitates.

8.2.2 Thermodynamic property characterization

The thermodynamic properties closely related to the mechanical properties in this study are the compositions of both the β matrix and β' precipitates, and the β' volume fraction. These data can be experimentally determined by atom probe tomography (APT). Details of the APT experiments have been presented in Section 5.2. Representative atom maps of different elements in one of the studied alloys (FBB-8) are shown in Figures 8.1b-f.

By counting the collected ions from APT, the compositions of the β matrix and β' precipitates can be determined. The β 'volume fraction can be estimated by applying the lever rule to all the elements. It should be pointed out that this kind of estimation is based on the assumption that only the β matrix and β' precipitate are present in the microstructure. If a third phase is present in the microstructure or there is a significant solute segregation to other microstructural features, such as grain boundaries or dislocations, the estimated β' volume fraction will need to be modified.

To verify the phases existing in FBB-12 and FBB-13, synchrotron high-energy X-ray diffraction was conducted for these two alloys at the Advanced Photon Source, Argonne National Laboratory. One bar with a cross-section of 12.7 × 12.7 mm^2 and a thickness of ~ 1 mm was machined by EDM from the bulk materials of FBB-12 and FBB-13, respectively. These specimens were X-rayed in transmission mode with a high-energy X-ray (115 keV), and the diffraction patterns were recorded by a MAR-345 two-dimensional detector.

8.2.3 Mechanical behaviors

Three-point bending tests were performed to study the ductility behavior of the alloys at room temperature, details of which have been presented in Section 6.7. Constant load tension creep tests were performed at 700°C under 140 MPa. Dog-bone samples with a gauge length of 28 mm and diameter of 3.17 mm were used for the tension creep tests. Three tests were conducted for each alloy composition to determine the average steady-state-creep rate.

8.3 Thermodynamic Calculations and Experimental Validation in the Fe-Ni-Al-Cr-Mo System

The isothermal section of Fe-Ni-Al-10Cr-2Mo (weight percent, wt.%) at 700^{o}C is calculated. Figure 8.2 locates the compositions of the five model alloys (listed in Table 8.1) on the figure. It should be mentioned that wt.% is used for this figure as the additions of Cr and Mo in the studied alloy systems are fixed at 10 wt.% and 2 wt.%, respectively, whereas their at.% varies slightly. To plot an isothermal section of a five-component system, two elements need to have fixed compositions. As can be seen, except for alloy FBB-13, all the other 4 alloys locate in the BCC-A2 + B2 two-phase field, which is consistent with a previous experimental observation [148]. It is noted that along the BCC-A2 + B2/ BCC-A2 + FCC-A1 phase boundary, the composition of FBB-13 is in the BCC-A2 + B2 + FCC-A1 three-phase field, while FBB-12 is in the BCC-A2 + B2 two-phase field. To verify the phases existing in FBB-12 and FBB-13, synchrotron high-energy X-ray diffraction was conducted on these alloys. The diffraction patterns in Figure 8.3a indicate that FBB-12 contains BCC-A2 and B2 only, whereas several weak peaks shown in Figure 8.3b reveal a possible existence of the FCC Fe in FBB-13. As the materials with

a FCC structure are well known to show very different behaviors in both ductility and creep properties, the alloy FBB-13 will not be used to compare with the others. The objective of this study is to develop an alloy which consists of only BCC-A2 and B2 phases, thus the additions of Al and Ni must be carefully controlled to avoid the formation of the FCC-Fe phase.

The calculated and experimentally determined phase compositions for the β matrix phase and the β' precipitate phase of three selected alloys are listed in Table 8.2 and compared in Figure 8.4. It is observed that all the data points locate along the diagonal reference line of the plot, indicating that a good accordance between the calculated and experimental results is obtained. Furthermore, the β' volume fractions are calculated and compared with the APT determined values by the lever rule. The results shown in Table 8.2 reveal that a good agreement is also obtained.

Both thermodynamic calculations and APT results exhibit that the β' precipitates are NiAl-type with some Fe partitioning inside (Table 8.2 and Figures 8.1b-d). Cr preferentially remains in the Fe matrix (Figure 8.1e), suggesting that the formation of NiAl-type precipitates does not deplete Cr in the matrix. This feature is beneficial for the alloy design, since the main reason for the addition of Cr is to increase the oxidation resistance of the Fe matrix. It should be also noted that there is a significant amount of Al remaining in the Fe matrix (Figure 8.1b) for some of the alloys, which is a cause of the low ductility problem of the studied alloys. A relatively large discrepancy between the calculated and measured results occurs for the Mo content in the B2-ordered precipitates (Table 8.2). This difference can be explained by the existence of α-Fe

particles inside some of the B2-ordered precipitates, which was shown in a previous study [148]. As revealed in Table 8.2, the Fe matrix contains a higher level of Mo than the B2-ordered precipitates. Consequently, the measured Mo compositions for the β' precipitate are higher than the calculated values. The detailed characterization of the β' precipitates has been presented elsewhere [148].

8.4 Creep Behavior

Figure 8.5a shows a representative tension creep curve of the studied alloys tested at a temperature of 700°C and a stress of 140 MPa. It exhibits the characteristics of a typical creep curve, which consists of three well developed stages. The creep rate firstly decreases gradually with time, then reaches a steady state in which the creep rate changes only very slightly with time, and finally the creep rate increases rapidly with time until the material ruptures. The average value of the creep rate in the steady state region is used as a parameter to compare the creep resistance of different materials. The results shown in Figure 8.5b reveal that the steady state creep rates decrease significantly with increasing the β' precipitate volume fraction. This trend is consistent with several previous creep studies [23-24] on a similar alloy system. The interaction between dislocation and precipitates in the crept samples was investigated by transmission electron microscopy (TEM) and has been presented elsewhere [211]. The strengthening mechanism was found to involve a coexistence of dislocation local climb and Orowan bowing [211]. In the precipitate-strengthened materials, the Orowan stress σ_{Or} [49] and the threshold stress σ_{LC} for local climb [212] are given by the expressions:

$$\sigma_{Or} = \frac{0.81Gb}{\pi\left[\left(\frac{2\pi}{3f}\right)^{1/2} - 1.63\right] r(1-\nu)^{1/2}} \ln\left(\frac{1.63r}{b}\right) \tag{8.1}$$

$$\sigma_{LC} = \frac{\sigma_{Or}}{\sqrt{2}}, \tag{8.2}$$

where G is the matrix shear modulus, υ the Poissons ratio, b the Burgers vector, and r the precipitate radius. A previous microstructural characterization [137] of these materials revealed that the precipitate radius (r) remains invariant regardless of the alloy composition, if the heat treatments are the same. Consequently, based on Eqs. (8.1) and (8.2), the values of both σ_{Or} and σ_{LC}, i.e. the creep resistance, increase with increasing the β' precipitate volume fraction f.

For the purpose to compare with other Fe-based candidate materials for steam turbine applications, the Larson-Miller parameters (LMP) of the alloys were calculated by:

$$\mathrm{LMP} = \mathrm{T}(25 + \log \mathrm{t})/1000, \tag{8.3}$$

where T is the temperature in Kelvin (K), and t is the rupture time in hour (h). The LMP values of FBB-8 and FBB-18 at a stress of 140 MPa were calculated by Eq. (8.3) to be 24.6 and 26.9, respectively. The LMP at 140 MPa of the other candidate materials, such as 10CrMoV steels, were reported to be ~ 26 [138]. In this regard, FBB-18 is clearly a very promising ferrite-based candidate, although the ductility studies in the following section reveal that it is very brittle at room temperature.

8.5 Ductility Behavior

The calculated three-point-bending ductility at room temperature for all the alloys from Eq. (8.1) is plotted as a function of the β' volume fraction in Figure 8.6. The results clearly

indicate that the ductility increases as the volume fraction of the β' phase decreases. This kind of trend was observed in the ductility study of several particle-strengthened alloys [49]. Brown and Embury [213] developed a model using the void growth and coalescence mechanism at the particles to explain this behavior, details of which can be found in the literature [49, 213]. Results regarding the study of the fracture surfaces have been presented elsewhere [137]. On the other hand, it is found that the ductility seems to be inversely related to the solubility of Al in the matrix BCC Fe phase, as shown in Figure 8.6. The alloy with a lower Al solubility in the matrix phase (FBB-12) exhibits improved ductility. This finding is in good accordance with the study of Herrmann et al. [48] on the strength and ductility of an Fe-Al alloy system. They [48] reported that Al has an ordering effect on the BCC Fe, and the dislocation mobility decreases with increasing the Al content, which lead to the low ductility of the alloys.

8.6 Search for Alloys with Balanced Properties

From the results presented in Sections 8.4 and 8.5 for the model alloys, it is clearly indicated that both the creep resistance and ductility are closely related to the volume fraction of β' precipitates. The creep resistance increases with increasing the β' precipitate volume fraction, whereas the opposite trend is observed for the ductility. Ductility was also found to be related to the solubility of Al in the Fe matrix, as the lower solubility favors the ductility. To strike a balance between the creep resistance and ductility, the following microstructural features should be satisfied: (1) a β' precipitate volume fraction of 20%, which is in between FBB-12 (13.5%, good ductility, but low creep resistance), and FBB-18 (28%, good creep resistance, but low ductility), (2) a solubility of Al in the β matrix phase lower than 4 % (Figure 8.6) to favor the ductility, and

(3) balanced Ni and Al compositions to avoid the formation of the FCC phase in the alloy since the focus of this study is on BCC-A2 + B2 alloys.

Thermodynamic calculations were carried out by Dr. Fan Zhang from Computherm LLC. to predict the alloy satisfying these microstructural requirements. As the β' volume fraction and the solubility of Al are mostly controlled by the amount of Ni and Al in the alloy, calculations were conducted for 3 alloy systems: Fe-10Cr-2Mo-10Al-(9-15)Ni, Fe-10Cr-2Mo-11Al-(9-15)Ni, and Fe-10Cr-2Mo-12Al-(9-15)Ni (at.%) to study the effect of Al and Ni on the alloy properties. The calculation results are shown in Figure 8.7. Figures 8.7a, c, and e are plots of phase fractions as a function of the Ni content in the alloy for the three alloys containing 10, 11, and 12% Al, respectively. The elemental solubilities in the β matrix phase for these three alloys are given in Figures 8.7b, d, and f, respectively. As observed from these plots, a low Al content in the alloy leads to the formation of FCC-A1 (Figures 8.7a and c), which is consistent with the calculated isotherm shown in Figure 8.2. The solubilities of Cr and Mo remain nearly constant while changing the contents of Al and Ni, which are also in good agreements with the APT results (Table 8.2).

It is observed from Figures 8.7a and b that the addition of 10% Al in the alloy system is too low. When 10% Al is used, at least 14.5% Ni needs to be used to satisfy the requirement of the 20% B2-ordered phase. However, if this amount of Ni is used, FCC-A1 will precipitate in addition to the B2-ordered phase, as is seen in Figure 8.7a. Figures 8.7c and d show that 11% Al seems to work well. When 11% Al is used, ~ 13.5% Ni is needed to reach a 20% β' precipitate,

and no FCC-A1 phase will form at this composition (Figure 8.7c). On the other hand, for the alloys containing 11%Al and 13.5%Ni, the solubility of Al in the β matrix phase is ~ 4% (Figure 8.7d), which satisfies the ductility requirement. If 12% Al is used, then 12.5% Ni is needed for the 20% B2 (Figure 8.7e), and at this composition, the solubility of Al in the β matrix phase is higher than 5%, as presented in Figure 8.7f, which is slightly high to satisfy the Al solubility requirement, as mentioned above. In summary, Fe-10Cr-2Mo-11Al-13.5Ni (at.%), is thus a potential alloy that should have the balanced creep resistance and ductility.

Based on these calculations, the alloy FBB-21 with this optimized composition was fabricated and heat-treated by the methods described in Section 8.2, and its mechanical properties were studied. The results are compared with two other model alloys: FBB-8 and FBB-18, as shown in Figure 8.8a. The ductility of FBB-21 is higher than that of FBB-18, but lower than that of FBB-8, while its creep resistance is higher than FBB-8, but lower than that of FBB-18. In other words, a balance can be indeed achieved between the creep resistance and ductility by adjusting the β' precipitate volume fraction and elemental partitioning, which verifies the prediction of the thermodynamic calculations. Figure 8.8b shows that the LMP values of the designed materials are comparable to the current state-of-the-art ferrite based materials for steam turbine applications. Using the approach described above, a further optimization of the properties is expected to achieve.

The results demonstrated in the current study show an example of combining thermodynamic calculations with focused experiments in the development of materials. The

phase stability, compositions, and volume fractions in the multi-component alloy systems can be calculated, based on the available thermodynamic descriptions of the phases. APT provides an unique technique to determine these microstructural features in the alloy system with nano-scale phases, thus validating the thermodynamic prediction. Several previous studies [214-217] demonstrated the application of integrating thermodynamic calculations with experimental reassessments in other multi-component alloy systems. In addition, the current study determined the dominant microstructural features controlling the ductility and creep resistance. Thermodynamic modeling can be subsequently applied to search for the appropriate alloy compositions and processing parameters to achieve an optimal microstructure combination. This combined approach was shown to significantly accelerate the alloy design process, which can be applied to similar alloy systems.

8.7 Summary

In this study, a thermodynamic modeling approach was integrated with focused experiments to study the ductility and creep resistance of steel alloys based on the Fe-Ni-Al-Cr-Mo system. The results calculated by thermodynamic modeling were in good agreements with those determined experimentally by the APT study. The mechanical property investigations showed that the creep resistance increases with increasing the β' precipitate volume fraction, while the opposite trend is observed for the ductility. Ductility was also found to be related to the solubility of Al in the Fe matrix, and lower solubility generally favors a ductility increase. To strike a balance between the creep resistance and ductility, the alloy should satisfy the following requirements: (1) a β' precipitate volume fraction of 20%, (2) the solubility of Al in

the β matrix lower than 4 at% to favor the ductility, and (3) balanced Ni and Al concentrations to avoid the formation of the FCC phase.

Thermodynamic calculations were used to quantify the volume fraction of β' precipitates and the elemental partitioning as a function of the alloy composition and temperature to identify the potential alloy compositions that satisfy the above requirements. The predicted alloy, FBB-21, with a composition of Fe-10Cr-2Mo-11Al-13.5Ni, was identified and experimentally studied. The experimental results showed that this alloy indeed exhibited a balanced room temperature ductility and high temperature creep resistance. This integrated thermodynamic modeling and focused experiments approach demonstrated in this study was found to be very effective in the alloy development.

CHAPTER 9 SUMMARY AND CONCLUSIONS

In this dissertation, the processing-microstructure-property relationship of a series of as-designed NiAl-strengthened ferritic steels was studied. Specifically, the alloys were fabricated by vacuum arc-melting, heat-treated, and hot-rolled to obtain the required microstructure. The microstructures of the Fe matrix and NiAl precipitates were characterized by a combination of optical microscopy, SEM, TEM, DSC, XRD, ND, EBSD, and APT. The effects of the microstructures on the ductility and creep resistance were investigated by three point bending, tension, and creep tests. The key microstructure features in controlling the properties were identified. Moreover, models were developed to predict the alloy compositions with favorable microstructure to accelerate the alloy design process. Based on the framework described above, the following conclusions can be drawn:

1) The primary and secondary β' precipitates in the alloy FBB-8 have compositions of $Ni_{41.2}Al_{43.6}Fe_{12.7}Cr_{0.8}Mo_{1.4}$ and $Ni_{26.3}Al_{41.6}Fe_{26.9}Cr_{3.3}Mo_{1.7}$, respectively, and that of the Fe matrix is $Fe_{75.1}Al_{8.1}Ni_{3.0}Cr_{11.9}Mo_{3.1}$. Based on the composition data, the volume fraction of the primary β' precipitates is estimated to be about 0.16.
2) Phase separation leading to the precipitation of Fe inside primary β' was confirmed by TEM and APT. The APT analysis showed that the precipitates inside β' has a composition of $Fe_{73.1}Al_{8.1}Ni_{4.2}Cr_{11.4}Mo_{2.5}$, which is very close to that of the Fe matrix.
3) Single peak fitting and a peak deconvolution approach can be used to separate the overlapping fundamental reflections obtained from ND measurements. The values of the

lattice parameters can be subsequently determined. The results at room temperature were validated by the results of synchrotron high energy X-ray diffraction.

4) The intensity of the superlattice reflection in the case of XRD was found to be weaker. ND was more suited for the purpose of measuring the lattice misfit in the current studied alloy system.

5) With the experimentally determined phase compositions by APT, models were developed to predict the lattice parameters as a function of the phase compositions at room temperature. The modeled results are in very good accordance with those determined experimentally by ND. The calculation of the lattice misfit in a given alloy can be therefore achieved.

6) Ductility is closely related to the precipitate volume fraction and elemental solubility in the Fe matrix, but independent of precipitate size and inter-particle spacing in the studied range.

7) A ductility increase from ~1% to ~10% has been achieved by hot-rolling. The compositions of both the matrix and precipitates were found to be nearly invariant after rolling. The formation of subgrains with a size of ~1 μm revealed by electron backscatter diffraction (EBSD) is believed to contribute to the ductility improvement.

8) The creep resistance increases with increasing the β' precipitate volume fraction, while the opposite trend is observed for the ductility. Ductility was also found to be related to the solubility of Al in the Fe matrix, and lower solubility generally favors a ductility increase.

9) To strike a balance between the creep resistance and ductility, the alloy should satisfy the following requirements: (1) a β' precipitate volume fraction of 20%, (2) solubility of Al in the

β matrix lower than 4 at.% to favor the ductility, and (3) balanced Ni and Al concentrations to avoid the formation of the FCC phase.

10) Thermodynamic calculations were used to to identify the potential alloy compositions that satisfy the above requirements. The predicted alloy, FBB-21, with a composition of Fe-10Cr-2Mo-11Al-13.5Ni (at.%), was identified and experimentally studied. The experimental results showed that this alloy indeed exhibited a balanced room temperature ductility and high temperature creep resistance. This integrated thermodynamic modeling and focused experiments approach demonstrated in this study was found to be very effective in the alloy development.

CHAPTER 10 FUTURE WORK

A NiAl-strengthened ferritic alloy with balanced ductility and creep resistance has been achieved by the studies included in this dissertation. However, further improvements of the mechanical properties of this alloy will be needed for the applications as steam turbine materials. The following studies may contribute an in-depth understanding of the mechanical properties and provide possible approaches to improve the properties of the designed alloys.

1) Although the creep resistance increases with increasing the NiAl precipitate volume fraction in the current studied range, there should be a critical value that the optimal creep resistance can be achieved. The determination of this value requires a systematic creep behavior study on the alloys with higher precipitate volume fractions (>30%).
2) The fracture mechanisms at room temperature have not been clearly identified. The dislocation structures before and after the tensile fracture will need to be investigated, especially for the hot rolled materials. Understanding the interaction between the dislocations and the solutes will provide the insights into the effects of the alloying elements on the ductility of the alloy.
3) Hot rolling has been shown to improve the room temperature ductility significantly. However, how it is going to affect the creep resistance has not yet studied. The optimal grain size to achieve the balanced ductility and creep resistance will need to be determined.
4) As a high temperature material, oxidation and corrosion resistance are the other important property to be studied. Long- term oxidation/corrosion tests in both air and

water-vapor conditions will need to be conducted.

5) More alloying elements will be considered to add into the alloy system to study their effects on both ductility and creep resistance. For example, Co can be added to provide additional strengthening and improve the cleavage strength of the alloy.
6) Large ingots (~ 50 kg) will be fabricated to investigate the differences between their properties and the previously fabricated experimental scale ingots.
7) Kinetic models will be proposed to predict the precipitate size and distribution, as these features are believed to have significant effects on the creep resistance.

References

[1] Viswanathan R. Materials for ultra-supercritical coal-fired power plant boilers. International Journal of Pressure Vessels and Piping 2006;83:778.

[2] Bhadeshia HKDH. Design of ferritic creep-resistant steels. Isij Int 2001;41.

[3] Dogan CP, Wright IG. Materials for ultra-supercritical steam turbines. 28th International Technical Conference on Coal utilization & Fuel Systems. Clearwater, FL, 2003.

[4] Hagen IV, Bendick W. Creep resistance ferritic steels for power plants. Mannesmann Forschungsinstitut GmbH.

[5] Blum R, Vanstone RW. Materials development for boilers and steam turbines operating at 700°C. Frendericia, Denmark and Rugby, United Kingdom: Elsam engineering A/S and Alstom Power Ltd.

[6] Bradley AJ, Taylor A. An X-ray study of the iron-nickel-aluminium ternary equilibrium diagram. Proc R Soc Lon Ser-A 1938;166:0353.

[7] Hao SM, Takayama T, Ishida K, Nishizawa T. Miscibility gap in Fe-Ni-Al and Fe-Ni-Al-Co systems. Metall. Trans. A 1984;15:1819.

[8] Villars P, Calvert LD. Pearson's handbook of crystallographics data for intermetallic phases. Metal Park, OH: ASM, 1985.

[9] Liaw PK, Liu CT, Fine ME, Ghosh G, Asta MD, Huang S, Teng ZK, Worthington D, Wang G. Computational design and prototype evaluation of aluminide-strengthened ferritic superalloys for power-generating turbine applications up to 1,033 K. Office of Fossil Energy, 2006.

[10] Banerjee BR, Hauser JJ, Capenos JM. ASM Trans. Quart. 1964;57.

[11] Blavette D, Martin C, Gallop G. Atomic probe analysis of precipitates in a FeCr20Ni2Al2 alloy. Scripta Metall. 1982;16:59.

[12] Hughes H. Precipitation in alloy steels containing chromium, nickel, aluminium and titanium. J. Iron Steel Inst. 1965;203.

[13] Bradley AJ. Microscopical Studies on the Iron-Nickel-Aluminium System .1. Alpha + Beta-Alloys and Isothermal Sections of the Phase Equilibrium Diagram. J Iron Steel I 1949;163:19.

[14] Bradley AJ. Microscopical Studies on the Iron Nickel Aluminium System .2. The Breakdown of the Body-Centred Cubic Lattice. J Iron Steel I 1951;168:233.

[15] Bradley AJ. Microscopical Studies on the Iron-Nickel-Aluminium System .3. Transformations of the Beta-Phase and Beta'-Phase. J Iron Steel I 1952;171:41.

[16] Marcon G, Peffen R, Lemaire H. Fe-Ni-Al Phase-Diagram in Alni Type Permanent-Magnets Related Area. Ieee T Magn 1978;14:685.

[17] Kolesar SC. Precipitation Processes in Fe-base Ferritic NiAl Alloys. vol. PhD: Northwestern University, 1971.

[18] Calderon-Bonavides HA. Oswald ripening of NiAl Precipitates in Fe Base Ni-Al-Mo Alloys. vol. PhD: Northwestern University, 1986.

[19] Calderon HA, Fine ME, Weertman JR. Coarsening and Morphology of B-'-Particles in Fe-Ni-Al-Mo Ferritic Alloys. Metall Trans A 1988;19:1135.

[20] Stallybrass C, Sauthoff G. Ferritic Fe-Al-Ni-Cr Alloys with Coherent Precipitates for High-temperature Applications. Mat Sci Eng a-Struct 2004;387-389:985.

[21] Miller MK, Hetherington MG. Atom Probe Analysis of Beta' Precipitation in a Model

Iron-based Fe-Ni-Al-Mo superalloy. Journal de Physique 1989;50:C8425.

[22] Jung I. Untersuchung des Verformungsverhhalten Ferritischer Zweiphasiger Fe-Ni-Al Legierungen mit Groben Antelen der Intermetallischen (Fe,Ni)Al-phase bei Hohen Temperaturen. vol. PhD: Technischen Hochschule Aachen, 1986.

[23] Zhu SM, Tjong SC, Lai JKL. Creep Behavior of a Beta '(NiAl) Precipitation Strengthened Ferritic Fe-Cr-Ni-Al alloy. Acta Mater 1998;46:2969.

[24] Stallybrass C, Schneider A, Sauthoff G. The Strengthening Effect of (Ni,Fe)Al Precipitates on the Mechanical Properties at High Temperatures of Ferritic Fe-Al-Ni-Cr alloys. Intermetallics 2005;13:1263.

[25] Rawers JC, Mattlin EM. Oxidation of Fe-7cr-12ni-(0-6)Al-(0-7)Si Alloys. Metall Trans A 1987;18:1805.

[26] Thornton DV, Mayer KH. Advanced Heat Resistant Steels for Power Generation. London: IOM Communications Ltd., 1999.

[27] Sims CT. The Superalloys. New York: John Wiley & Sons, Inc., 1972.

[28] Mott NF, Nabarro FRN. Report of the Conference on Strength of Solids. Physical Society, 1948. p.1.

[29] Pelloux RMN, Grant NJ. Solid Solution and 2nd Phase Strengthening of Nickel Alloys at High and Low Temperatures. T Am I Min Met Eng 1960;218:232.

[30] Fleischer RL. Substitutional Solution Hardening. Acta Metallurgica 1963;11:203.

[31] Fleischer RL. The Strengthening of Metals. Reinhold, New York, 1964.

[32] Davies RG, Stoloff NS. Trans. Met. Soc. AIME 1965;233:714.

[33] Mok CM. Effects of Alloying Elements on Steels.

http://users6.nofeehost.com/mestijaya/cmm/.

[34] Leslie WC. Iron and Its Dilute Substitutional Solid-Solutions. Metall Trans 1972;3:5.

[35] Suzuki H. Nachr. Gott. Akad. Wiss. 1971.

[36] Vanderpl.J, Deruytte.A. Solution Hardening of Lead Single Crystals at Liquid Air Temperature. J Mater Sci 1969;4:499.

[37] Pugh SF. Relations between the Elastic Moduli and the Plastic Properties of Polycrystalline Pure Metals. Philos Mag 1954;45:823.

[38] Crutchley DE, Reid CN. High Temperature Materials. Reutte, Tyrol: Metallwerke Plansee AG, 1969.

[39] Crutchley DE, Reid CN, Webster TH. Proc. 2nd Int. Conf. Strength Metals and Alloys. ASM, vol. 1. Cleveland, Ohio, 1970. p.127.

[40] Speich GR, Schwoeble AJ, Leslie WC. U. S. Steel Corp.

[41] Justusson W, Zackay VF, Morgan ER. Trans. ASM 1957;49.

[42] Morgand P, Mouturat P, Sainfort G. Structure and Mechanical Properties of Iron - Aluminium Alloys. Acta Metallurgica 1968;16:867.

[43] Sykes C, Bampfylde JW. JISI 1934;130.

[44] McKamey CG. Physical Metallurgy and Processing of Intermetallic Compounds. London: Chapman & Hall, 1996.

[45] Bannykh OA, Sudin IF, Kashin WI, Prokoshkin DA, Samarin AN. Proc Symp Metallurgy, Metallography and Physico-Chemical Methods of Investigations. Moscow, 1963. p.68.

[46] Koster W, Godecke T. Z Metallk 1980;71:765.

[47] Kalugin AS, Terenteyev ON. Russian Metallurgy 1983;19:95.

[48] Herrmann J, Inden G, Sauthoff G. Deformation Behaviour of Iron-rich Iron-aluminum Alloys at Low Temperatures. Acta Mater 2003;51:2847.

[49] Martin JW. Micromechanisms in Particle-hardened Alloys. Cambridge, Great Britain: The Press Syndicate of the University of Cambridge, 1980.

[50] Goods SH, Brown LM. Nucleation of Cavities by Plastic-Deformation - Overview. Acta Metallurgica 1979;27:1.

[51] Brown LM, Embury JF. The Microstructure and Design of Alloys. Proceedings of the Third International Conference on the Strength of Metals and Alloys, vol. 1. Cambridge, the institute of metals, 1973. p.164.

[52] Palmer IG, Smith GC. Fracture of Internally Oxidized Copper Alloys. AIME conf oxide dispersion strengthening. Bolton Landing, New York: Gordon and Breach, 1967. p.1967.

[53] Ebeling R, Ashby MF. Dispersion Hardening of Copper Single Crystals. Philos Mag 1966;13:805.

[54] Ashby MF. Work Hardening of Dispersion-Hardened Crystals. Philos Mag 1966;14:1157.

[55] Palmer IG, Smith GC, Warda RD. Some Aspects of Ductile Fracture in Metals. Conf Physical Basis of Yield and Fracture. London: Insititute of Physics and Physical Society, 1967. p.53.

[56] Pelloux RMN. Met Eng Quart 1965;5:26.

[57] Gurland J. Trans AIME 1963;227:1146.

[58] Turkalo AM, Low JRJ. Trans AIME 1958;212:750.

[59] Edelson BI, Baldwin WMJ. Trans ASM 1962;55:230.

[60] Lewandowski JJ, Liu C, Hunt WH. Effects of Matrix Microstructure and Particle Distribution on Fracture of an Aluminum Metal Matrix Composite. Mat Sci Eng a-Struct 1989;107:241.

[61] Lloyd DJ. Particle-Reinforced Aluminum and Magnesium Matrix Composites. Int Mater Rev 1994;39:1.

[62] Stone IC, Tsakiropoulos P. The Effect of Reinforcement on the Notched and Unnotched Room Temperature Tensile Properties of Al-4wt%Cu/SiCp MMCs. Mat Sci Eng a-Struct 1998;241:19.

[63] Lloyd DJ. Aspects of Fracture in Particulate Reinforced Metal Matrix Composites. Acta Metall Mater 1991;39:59.

[64] Lloyd DJ, Morris PL, Nehme E. Fabrication of Particulates Reinforced Metal Composites. Materials Park, OH: ASM International, 1990.

[65] Edelson BI, Baldwin WM. Trans. AMER. Soc. Met. 1962.

[66] Rogers HC. The Effects of Material Variables on Ductility: Taylor & Francis, 1968.

[67] Dieter GE. Mechanical Metallurgy: The McGraw-Hill Companies, Inc, 1988.

[68] Smith E. Physical Basis of Yield and Fracture. Conference Proceedings, Institute of Physics, Physical Society. Oxford, 1966. p.36.

[69] Kotilainen H, Torronen K. In: Taplin DMR, editor. Proceedings of the Forth International Conference on Fracture, vol. 2. Waterloo, Canada: University of Waterloo Press, 1977. p.57.

[70] Jaffee RI, Hahn GT. Nation Physical Laboratory Symposium, vol. 15. London, 1963. p.707.

[71] Petch NJ. The Cleavage Strength of Polycrystals. J Iron Steel I 1953;174:25.

[72] Baker I. Improving the Ductility of Intermetallic Compounds by Particle-induced Slip Homogenization. Scripta Mater 1999;41:409.

[73] Miracle DB. Overview No-104 - the Physical and Mechanical-Properties of Nia1. Acta Metall Mater 1993;41:649.

[74] Hahn KH, Vedula K. Room-Temperature Tensile Ductility in Polycrystalline B2 Nial. Scripta Metallurgica 1989;23:7.

[75] Ball A, Smallman RE. Deformation Properties and Electron Microscopy Studies of Intermetallic Compound Nial. Acta Metallurgica 1966;14:1349.

[76] Rozner AG, Wasilews.Rj. Tensile Properties of Nial and Niti. J I Met 1966;94:169.

[77] Lautensc.Ep, Kiewit DA, Brittain JO. Influence of Point Defects Upon Compressive Strength of Ni-Al. T Metall Soc Aime 1965;233:1297.

[78] Baker I, Nagpal P, Liu F, Munroe PR. The Effect of Grain-Size on the Yield Strength of Feal and Nial. Acta Metall Mater 1991;39:1637.

[79] Vandervo.RR, Mukherje.AK, Dorn JE. Elevated-Temperature Deformation Mechanisms Inbeta'-Nial. ASM Trans Q 1966;59:930.

[80] Noebe RD, Bowman RR, Nathal MV. Physical and Mechanical Properties of the B2 Compound NiAl. Int Mater Rev 1993;38:195.

[81] George EP, Liu CT. Brittle-Fracture and Grain-Boundary Chemistry of Microalloyed Nial. J Mater Res 1990;5:754.

[82] Law CC, Blackburn MJ. Rapidly Solidified Lightweight Durable Disk Material. West Palm Beach, FL: United Technologies Corp., Pratt and Whitney Group, 1985.

[83] Graham RB. vol. ME. Hanover, NH: Dartmouth College, 1984.

[84] Bowman RR, Noebe RD, Raj SV, Locci IE. Correlation of Deformation Mechanisms with the Tensile and Compressive Behavior of Nial and Nial(Zr) Intermetallic Alloys. Metall Trans A 1992;23:1493.

[85] Groves GW, Kelly A. Independent Slip Systems in Crystals. Philos Mag 1963;8:877.

[86] Nagpal P, Baker I. The Effect of Grain-Size on the Room-Temperature Ductility of Nial. Scripta Metall Mater 1990;24:2381.

[87] Field RD, Lahrman DF, Darolia R. Slip Systems in (001) Oriented Nia1 Single-Crystals. Acta Metall Mater 1991;39:2951.

[88] Seybolt AU, Westbrook JH. Metals for the Space Age. Plansee Seminar Proc., 1964. p. 845.

[89] Kruisman JJ, Vitek V, Dehosson JTM. Atomic-Structure of Stoichiometric and Non-Stoichiometric Grain-Boundaries in A3b Compounds with L12 Structure. Acta Metallurgica 1988;36:2729.

[90] Chaki TK. Mechanism of Boron-Induced Strengthening of Grain-Boundaries in Ni3al. Phil Mag Lett 1991;63:123.

[91] Vitek V, Chen SP. Modeling of Grain-Boundary Structures and Properties in Intermetallic Compounds. Scripta Metall Mater 1991;25:1237.

[92] Petton G, Farkas D. Grain-Boundary Structure Simulations in B2-Ordered Nial. Scripta Metall Mater 1991;25:55.

[93] Miracle DB. Deformation in Nial Bicrystals. Acta Metall Mater 1991;39:1457.

[94] Fraser HL, Loretto MH, Smallman RE. Plastic-Deformation of Nial Single-Crystals between 300 Degrees K and 1050 Degrees K 2. Mechanism of Kinking and Uniform

Deformation. Philos Mag 1973;28:667.

[95] Groves GW, Kelly A. Change of Shape Due to Dislocation Climb. Philos Mag 1969;19:977.

[96] Grala EM. Mechanical Properties of Intermetallic Compounds. Wiley, New York, 1960.

[97] Darolia R. Nial Alloys for High-Temperature Structural Applications. Jom-J Min Met Mat S 1991;43:44.

[98] Darolia R, Lahrman D, Field R. The Effect of Iron, Gallium and Molybdenum on the Room-Temperature Tensile Ductility of Nial. Scripta Metall Mater 1992;26:1007.

[99] Rachinger WA, Cottrell AH. Slip in Crystals of the Caesium Chloride Type. Acta Metallurgica 1956;4:109.

[100] Miracle DB, Russell S, Law CC. Temperature Ordered Intermetallic Alloys III. In: Liu CT, Taub AI, Stoloff NS, Koch CC, editors. MRS, vol. 133, 1989. p. 225.

[101] Schulson EM, Barker DR. A Brittle to Ductile Transition in Nial of a Critical Grain-Size. Scripta Metallurgica 1983;17:519.

[102] Nathal MV, Diaz JO, Miner RV. Mater. Res. Soc. Symp. Proc. 1989;133:269.

[103] Noebe RD, Whittenberger JD. Unpublished Research. Cleveland, OH: NSA Lewis Research Center, 1991.

[104] Polvani RS, Tzeng WS, Strutt PR. High-Temperature Creep in a Semi-Coherent Nial-Ni2alti Alloy. Metall Trans A 1976;7:33.

[105] Whittenberger JD. Effect of Composition and Grain-Size on Slow Plastic-Flow Properties of Nial between 1200 and 1400 K. J Mater Sci 1987;22:394.

[106] Nathal MV, Ebert LJ. Elevated-Temperature Creep-Rupture Behavior of the

Single-Crystal Nickel-Base Superalloy Nasair 100. Metall Trans A 1985;16:427.

[107]Whittenberger JD, Viswanadham RK, Mannan SK, Kumar KS. 1200-K to 1400-K Slow Strain Rate Compressive Behavior of Small Grain-Size Nial/Ni2alti Alloys and Nial/Ni2alti-Tib2 Composites. J Mater Res 1989;4:1164.

[108]Whittenberger JD, Gaydosh DJ, Kumar KS. 1300-K Compressive Properties of Several Dispersion Strengthened Nial Materials. J Mater Sci 1990;25:2771.

[109]Whittenberger JD, Ray R, Jha SC, Draper S. 1000-1300 K Slow Strain Rate Properties of Nial Containing Dispersed Tib2 and Hfb2. Mat Sci Eng a-Struct 1991;138:83.

[110]Jha SC, Ray R, Whittenberger JD. Carbide-Dispersion-Strengthened B2 Nial. Mat Sci Eng a-Struct 1989;119:103.

[111]Sikka VK, Ward CT, Thomas KC. Modified 9Cr-1Mo Steel-An Improved Alloy for Steam Generator Application. Ferritic Steels for High Temperature Applications. Warren, PA, 1981.

[112]Canonico DA. Thick-Walled Pressure Vessels for Energy Systems. Technical Program and Data Package for Use of Modified 9Cr-1Mo Steel, ASME Sect. I and VIII, 1982.

[113]Blum R. Newly Developed High-Temperature Ferritic-Martensitic Steels from USA, Japan, and Europe. VGB Kraftwerkstechnik (English Issue) 1994;74:553.

[114]Kelly TF, Miller MK. Invited Review Article: Atom probe tomography. Rev Sci Instrum 2007;78.

[115]Blavette D, Cadel E, Deconihout B. The Role of the Atom Probe in the Study of Nickel-based Superalloys. Mater Charact 2000;44:133.

[116]Miller MK. Contributions of Atom Probe Tomography to the Understanding of

Nickel-based Superalloys. Micron 2001;32:757.

[117]Thomson RC, Miller MK. Atom Probe Characterisation of High Temperature Materials. Mater Sci Tech Ser 2000;16:1199.

[118]Hyde JM, Miller MK, Hetherington MG, Cerezo A, Smith GDW, Elliott CM. Spinodal Decomposition in Fe-Cr Alloys - Experimental-Study at the Atomic-Level and Comparison with Computer-Models .2. Development of Domain Size and Composition Amplitude. Acta Metall Mater 1995;43:3403.

[119]Hyde JM, Miller MK, Hetherington MG, Cerezo A, Smith GDW, Elliott CM. Spinodal Decomposition in Fe-Cr Alloys - Experimental-Study at the Atomic-Level and Comparison with Computer-Models 3. Development of Morphology. Acta Metall Mater 1995;43:3415.

[120]Miller MK, Hyde JM, Hetherington MG, Cerezo A, Smith GDW, Elliott CM. Spinodal Decomposition in Fe-Cr Alloys - Experimental-Study at the Atomic-Level and Comparison with Computer-Models 1. Introduction and Methodology. Acta Metall Mater 1995;43:3385.

[121]Hono K. Overview No. 133 - Atom Probe Microanalysis and Nanoscale Microstructures in Metallic Materials. Acta Mater 1999;47:3127.

[122]Miller MK. Atom Probe Tomography Characterization of Solute Segregation to Dislocations. Microsc Res Techniq 2006;69:359.

[123]Marquis EA, Seidman DN, Asta M, Woodward C, Ozolins V. Mg Segregation at Al/Al3Sc Heterophase Interfaces on an Atomic Scale: Experiments and Computations. Phys Rev Lett 2003;91.

[124]Larson DJ, Petford-Long AK, Ma YQ, Cerezo A. Information Storage Materials: Nanoscale Characterisation by Three-dimensional Atom Probe Analysis. Acta Mater

2004;52:2847.

[125]Guinier A. X-ray diffraction in Crystals, Imperfect Crystals, and Amorphous Bodies: Dover Publications, Inc., 1994.

[126]Rietveld HM. A Profile Refinement Method for Nuclear and Magnetic Structures. J Appl Crystallogr 1969;2:65.

[127]Rietveld HM. Line Profiles of Neutron Powder-Diffraction Peaks for Structure Refinement. Acta Crystallogr 1967;22:151.

[128]Gilles R, Mukherji D, Hoelzel M, Strunz P, Toebbens DM, Barbier B. Neutron and X-ray Diffraction Measurements on Micro- and Nano-sized Precipitates Embedded in a Ni-based Superalloy and after Their Extraction from the Alloy. Acta Mater 2006;54:1307.

[129]Lahrman DF, Field RD, Darolia R, Fraser HL. Investigation of Techniques for Measuring Lattice Mismatch in a Rhenium Containing Nickel-Base Superalloy. Acta Metallurgica 1988;36:1309.

[130]Kuhn HA, Biermann H, Ungar T, Mughrabi H. An X-Ray Study of Creep-Deformation Induced Changes of the Lattice Mismatch in the Gamma-'-Hardened Monocrystalline Nickel-Base Superalloy Srr-99. Acta Metall Mater 1991;39:2783.

[131]Tiley J, Srinivasan R, Banerjee R, Viswanathan GB, Toby B, Fraser HL. Application of X-ray and Neutron Diffraction to Determine Lattice Parameters and Precipitate Volume Fractions in Low Misfit Nickel Base Superalloys. Mater Sci Tech Ser 2009;25:1369.

[132]Stone HJ, Holden TM, Reed RC. On the Generation of Microstrains during the Plastic Deformation of Waspaloy. Acta Mater 1999;47:4435.

[133]Liaw PK, Liu CT, Fine ME, Ghosh G, Asta MD, Huang S, Teng ZK, Worthington D,

Wang G. Computational Design and Prototype Evaluation of Aluminide-strengthened Ferritic Superalloys for Power-generating Turbine Applications up to 1,033 K. Office of Fossil Energy, 2006.

[134]Bhadeshia HKDH. Design of Ferritic Creep-resistant Steels. Isij Int 2001;41:626.

[135]Calderon HA, Weertman JR, Fine ME. Effect of Cyclic Plastic-Deformation on Elevated-Temperature Ostwald Ripening of an Alloy with Coherent Precipitates. Scripta Metallurgica 1984;18:587.

[136]Zhu SM, Tjong SC. Dislocation/particle Interactions in Beta'(NiAl) Precipitation Strengthened Ferritic Fe-19Cr-4Ni-2Al alloy. Metall Mater Trans A 1997;28:1095.

[137]Teng ZK, Liu CT, Ghosh G, Liaw PK, Fine ME. Effects of Al on the Microstructure and Ductility of NiAl-strengthened Ferritic Steels at RoomTtemperature. Intermetallics 2010;18:1437.

[138]Viswanathan R, Bakker W. Materials for Ultrasupercritical Coal Power Plants - Turbine Materials: Part II. J Mater Eng Perform 2001;10:96.

[139]Goldstein JI, Williams DB, Cliff G. Principles of Analytical Electron Microscopy. New York: Plenum Press, 1986.

[140]Ghosh G, Olson GB. Precipitation of Paraequilibrium Cementite: Experiments, and Thermodynamic and Kinetic modeling. Acta Mater 2002;50:2099.

[141]Jung J, Ghosh G, Isheim D, Olson GB. Precipitation of Heusler phase (Ni2TiAl) from B2-TiNi in Ni-Ti-Al and Ni-Ti-Al-X (X = Hf, Zr) Alloys. Metall Mater Trans A 2003;34A:1221.

[142]Voorhees PW, Mcfadden GB, Johnson WC. On the Morphological Development of

2nd-Phase Particles in Elastically-Stressed Solids. Acta Metall Mater 1992;40:2979.

[143]Oblak JM, Doherty JE, Giamei AF, Kear BH. Precipitation of Gamma in Gamma' of Nickel-Base Superalloys. Metall Trans 1974;5:1252.

[144]Kakehi K. Effect of Primary and Secondary Precipitates on Creep Strength of Ni-base Superalloy Single Crystals. Mat Sci Eng a-Struct 2000;278:135.

[145]Wusatowska-Sarnek AM, Ghosh G, Olson GB, Blackburn MJ, Aindow M. Characterization of the Microstructure and Phase Equilibria Calculations for the Powder Metallurgy Superalloy IN100. J Mater Res 2003;18:2653.

[146]Calderon H, Fine ME. Coarsening Kinetics of Coherent Nial-Type Precipitates in Fe-Ni-Al and Fe-Ni-Al-Mo Alloys. Mater Sci Eng 1984;63:197.

[147]Ecob RC, Ricks RA, Porter AJ. The Measurement of Precipitate Matrix Lattice Mismatch in Nickel-Base Super-Alloys. Scripta Metallurgica 1982;16:1085.

[148]Teng ZK, Miller MK, Ghosh G, Liu CT, Huang S, Russell KF, Fine ME, Liaw PK. Characterization of Nanoscale NiAl-type Precipitates in a Ferritic Steel by Electron Microscopy and Atom Probe Tomography. Scripta Mater 2010;63:61.

[149]Larson AC, Von Dreele RB. General Structure Analysis System (GSAS). Los Alamos National Laboratory Report LAUR, 1994. p.86.

[150]VonDreele RB. Quantitative texture analysis by Rietveld refinement. J Appl Crystallogr 1997;30:517.

[151]Neutron News, 1992.

[152]Jiang C. Site preference of transition-metal elements in B2NiAl: A comprehensive study. Acta Mater 2007;55:4799.

[153]CRC Handbook of Chemistry and Physics. In: Haynes WM, Lide DR, editors. Property of Solids, 2011.

[154]Basinski ZS, Humerothery W, Sutton AL. The Lattice Expansion of Iron. Proc R Soc Lon Ser-A 1955;229:459.

[155]Bradley AJ, Jay AH. The Formation of Superlattices in Alloys of Iron and Aluminium. P R Soc Lond a-Conta 1932;136:210.

[156]Taylor A, Jones RM. Constitution and Magnetic Properties of Iron-Rich Iron-Aluminum Alloys. J Phys Chem Solids 1958;6:16.

[157]Abrahams.Ep, Lopata SL. Lattice Parameters and Solubility Limits of Alpha Iron as Affected by Some Binary Transition-Element Additions. T Metall Soc Aime 1966;236:76.

[158]Sutton AL, Humerothery W. The Lattice Spacings of Solid Solutions of Titanium, Vanadium, Chromium, Manganese, Cobalt and Nickel in Alpha-Iron. Philos Mag 1955;46:1295.

[159]Gulyaev AP, Trusova EF. *Zakonomernosti Izmeneniya Svoistv V Tverdykh Rastvorakh. Zh Tekh Fiz+ 1950;20:66.

[160]Ghosh G. Lattice Parameter Modeling of Disordered and Ordered BCC Phases in the Fe-Al-Co-Cr-Ni-Mo System. EPRI, 1999.

[161]Kitabjian PH, Nix WD. Atomic Size Effects in Ni-Al based Solid Solutions. Acta Mater 1998;46:701.

[162]Frommeyer G, Fischer R, Deges J, Rablbauer R, Schneider A. APFIM Investigations on Site Occupancies of the Ternary Alloying Elements Cr, Fe, and Re in NiAl. Ultramicroscopy 2004;101:139.

[163]Latreche H, Bozzolo G, Masset PJ, Weber T, Schutze M. Measurements of the Coefficient of Thermal Expansion (CTE) of NiAlMo Alloys and Comparison with Modelling Predictions. Mat Sci Eng a-Struct 2010;527:5837.

[164]Lipson H, Taylor A. Defect Lattices in Some Ternary Alloys. Proc R Soc Lon Ser-A 1939;173:0232.

[165]Gilles R. Neutron scattering, a Powerful Tool in Material Science Considering Superalloys as an Example. Z Metallkd 2005;96:325.

[166]Chantler CT, Olsen K, Dragoset RA, Chang J, Kishore AR, Kotochigova SA, Zucker DS. J. Phys. Chem. Ref. Data 2000.

[167]Reddy BV, Deevi SC. Thermophysical Properties of FeAl (Fe-40 at.%Al). Intermetallics 2000;8:1369.

[168]Zhao YH, Sheng HW, Lu K. Microstructure Evolution and Thermal Properties in Nanocrystalline Fe during Mechanical Attrition. Acta Mater 2001;49:365.

[169]Gilder HM. Calculation of the Intrinsic Coefficient of Thermal-Expansion of Spherical, Coherent Inclusions - Application to Al-Ag, Fe-Cu, and Ni-Al. Phys Rev B 1982;25:650.

[170]Madeleine DC. The Microstructure of Superalloys. Boca Raton, FL: CRC Press, 1997.

[171]Blavette D, Bostel A, Sarrau JM, Deconihout B, Menand A. An Atom-Probe for 3-Dimensional Tomography. Nature 1993;363:432.

[172]Ghosh G, Olson GB, Fine ME. In: Johnson WC, Howe JM, Langhlin DE, SOffa WA, editors. Solid-Solid Phase Transformations. Warrandale, PA: TMS-AIME, 1994. p.611.

[173]Petch NJ. The Influence of Some Substitutional Alloys on the Cleavage of Ferritic Steels. Acta Metallurgica 1987;35:2027.

[174]Chang KM, Darolia R, Lipsitt HA. Cleavage Fracture in B2 Aluminides. Acta Metall Mater 1992;40:2727.

[175]Darolia R, Chang KM, Hack JE. Observation of High-Index (511) Type Fracture Planes and Their Influence on Toughness in Nial Single-Crystals. Intermetallics 1993;1:65.

[176]Law CC, Blackburn MJ. Rapid Solidified Lighweight Durable Disk materials. Air Force Wright Aeronaut Lab, 1987.

[177]Cotton JD, Noebe RD, Kaufman MJ. The Effects of Chromium on Nial Intermetallic Alloys 2. Slip Systems. Intermetallics 1993;1:117.

[178]Jung J, Ghosh G, Olson GB. A Comparative Study of Precipitation Behavior of Heusler Phase (Ni2TiAl) from B2-TiNi in Ni-Ti-Al and Ni-Ti-AI-X (X = Hf, Pd, Pt, Zr) Alloys. Acta Mater 2003;51:6341.

[179]Liu TF, Jeng SC, Wu CC. Phase-Transition in an Fe-23.2al-4.1ni Alloy. Metall Trans A 1992;23:1395.

[180]Marcon G, Preffen R, Lemaire H. Fe-Ni-Al Phase-diagram in AlNi Type Permanent-magnets Related Area. IEEE Trans Magn 1987;14:685.

[181]Tian WH, Nemoto M. Precipitation Behavior of (Al,Ag)(3)Ti and Ti3AlC in L1(0)-TiAl in Ti-Al-Ag system. Intermetallics 1999;7:1261.

[182]Fischer R, Frommeyer G, Schneider A. Chromium Precipitation in B2-ordered NiAl-2 at.% Cr Alloys Investigated by Atom Probe Field Ion Microscopy. Mat Sci Eng a-Struct 2002;327:47.

[183]Standard Test Methods for Flexural Properties of Unreinforced and Reinforced Plastics and Electrical Insulating Materials: American Society for Testing and Materials, 2007.

[184]Teng ZK, Zhang F, Miller MK, Huang S, Chou YT, Tien RH, Liu CT, Chang YA, Liaw PK. New Ferritic Steels with Balanced Creep Resistance and Ductility Designed by Coupling Thermodynamic Calculations with Focused Experiments. 2010.

[185]Patrick DK, Chang KM, Miracle DB, Lipsitt HA. High Temperature Ordered Intermetallic Alloys. In: Johnson L, Stiegler JO, Pope DP, editors. MRS, 1991. p. 213.

[186]Kovalev AI, Barskaya RA, Wainstein DL. Effect of Alloying on Electronic Structure, Strength and Ductility Characteristics of Nickel Aluminide. Surf Sci 2003;532:35.

[187]Teng ZK, Liu CT, Miller MK, Ghosh G, Kenic E, Liaw PK. Room Temperature Ductility of NiAl-strengthened Ferritic Steels: Effects of Precipitate Microstructure and Hot Rolling. 2010.

[188]Ukai S, Nishida T, Okada H, Okuda T, Fujiwara M, Asabe K. Development of Oxide Dispersion Strengthened Ferritic Steels for FBR Core Application 1. Improvement of Mechanical Properties by Recrystallization Processing. J Nucl Sci Technol 1997;34:256.

[189]Amigo V, Ortiz JL, Salvador MD. Microstructure and Mechanical Behavior of 6061Al Reinforced with Silicon Nitride Particles, Processed by Powder Metallurgy. Scripta Mater 2000;42:383.

[190]Brown LM, Embury JF. The Microstructure and Design of Alloys. Third International Conference on the Strength of Metals and Alloys, vol. 1, 1973. p.164.

[191]Mummery P, Derby B. The Influence of Microstructure on the Fracture-Behavior of Particulate Metal Matrix Composites. Mat Sci Eng a-Struct 1991;135:221.

[192]Turkalo AM, Low JR. The Effect of Carbide Dispersion on the Strength of Tempered Martensite. T Am I Min Met Eng 1958;212:750.

[193]Wilcox BA, Clauer AH. Creep of Thoriated Nickel above and Below 0.5 Tm. T Metall Soc Aime 1966;236:570.

[194]Wolff IM, Ball A. Ductility in High-Chromium Super-Ferritic Alloys .2. Plastic-Deformation and Crack-Zone Shielding. Acta Metall Mater 1991;39:2771.

[195]Huang EW, Liaw PK, Porcar L, Liu Y, Liu YL, Kai JJ, Chen WR. Study of Nanoprecipitates in a Nickel-based Superalloy Using Small-angle Neutron Scattering and Transmission Electron Microscopy. Appl Phys Lett 2008;93.

[196]Corti CW, Cotterill P, Fitzpatrick G. Int. Met. Rev. 1974;19.

[197]Ghosh G., Unpublished Research

[198]Kuhn H, Medlin D. Mechanical Testing and Evaluation, ASM Handbook: ASM, 2000.

[199]Chell GG, Curry DA. Development in Fracture Mechanics. London: Applied Science Publishers, 1981.

[200]Curry DA, Knott JF. Met Sci 1978;12.

[201]Oates G. Effect of Temperature and Strain Rate on Cleavage Fracture in a Mild Steel and a Low-Carbon Manganese Steel. J Iron Steel I 1969;207:353.

[202]Sharma RC. Principles of Heat Treatment of Steels: New Age International, 2003.

[203]Marcinkowski MJ, Kayser FX, Taylor ME. Relationship between Atomic Ordering and Fracture in Fe-Al Alloys. J Mater Sci 1975;10:406.

[204]Thompson AW. Substructure Strengthening Mechanisms. Metall Trans A 1977;8:833.

[205]Cottrell AH. The Mechanical Properties of Matter. London: John Wiley, 1964.

[206]Petch NJ. Fracture and Advanced Treatise. New York: Academic Press, 1968.

[207]Imayev RM, Gabdullin NK, Salishchev GA, Senkov ON, Imayev VM, Froes FH. Effect

of Grain Size and Partial Disordering on Ductility of Ti3Al in the Temperature Range of 20-600 Degrees C. Acta Mater 1999;47:1809.

[208]Lasalmonie A, Strudel JL. Influence of Grain-Size on the Mechanical-Behavior of Some High-Strength Materials. J Mater Sci 1986;21:1837.

[209]Eleno L, Frisk K, Schneider A. Assessment of the Fe-Ni-Al system. Intermetallics 2006;14:1276.

[210]Huang SY, Worthington DL, Asta M, Ozolins V, Ghosh G, Liaw PK. Calculation of Impurity Diffusivities in Alpha-Fe Using First-principles Methods. Acta Mater 2010;58:1982.

[211]Huang S, Li X, Ghosh G, Kenik EA, Ilavsky J, Teng ZK, Wang G, Morris EF, Liu CT, Liu L, Liaw PK. 2010.

[212]Mclean M. On the Threshold Stress for Dislocation Creep in Particle Strengthened Alloys. Acta Metallurgica 1985;33:545.

[213]Brown LM, Embury JF. The Institute of Metals 1973;1.

[214]Bei H, Yang Y, Viswanathan GB, Rawn CJ, George EP, Tiley J, Chang YA. Formation, Stability and Crystal Structure of the Sigma Phase in Mo-Re-Si Alloys. Acta Mater 2010;58:6027.

[215]Yang Y, Bei H, Chen SL, George EP, Tiley J, Chang YA. Effects of Ti, Zr, and Hf on the Phase Stability of Mo_ss + Mo3Si + Mo5SiB2 Alloys at 1600 Degrees C. Acta Mater 2010;58:541.

[216]Zhu J, Zhang C, Cao W, Yang Y, Zhang F, Chen S, Morgan D, Chang YA. Experimental Investigation and Thermodynamic Modeling of the Ni-Al-Ru Ternary System. Acta Mater 2009;57:202.

[217]Zhang F, Chang YA, Du Y, Chen SL, Oates WA. Application of the Cluster-site Approximation (CSA) Model to the f.c.c. Phase in the Ni-Al system. Acta Mater 2003;51:207.

APPENDIX

Table 1.1 Compositions of the recently developed creep-resistant ferritic steels

Alloy	C	Si	Mn	Al	Cr	Ni	Mo	W	V	Nb	B	N
T/P91	0.08	0.2	0.3	0.04	8	0.4	0.85	-	0.18	0.06	-	0.03
T/P911	0.09	0.1	0.3	0.04	8.5	0.1	0.9	0.9	0.18	0.06	0.005	0.05
T/P92	0.07	0.5	0.3	0.04	8.5	0.4	0.3	1.5	0.15	0.04	0.001	0.03

Table 2.1 Chemical compositions of creep resistant ferritic steels for power plants

No.	EN-Designation	Comparable ASTM Grade	Chemical Composition (mass-%)													
			C	Si	Mn	Al	Cu	Cr	Ni	Mo	W	Ti	V	Nb	B	N
1	P 235	A	max. 0.16	max. 0.35	0.40 –0.80	min. 0.020	max. 0.30	max. 0.30	max. 0.30	max. 0.08						
2	P 355		max. 0.22	0.15 –0.35	1.00 –1.50	max. 0.060								0.015 –0.10		
3	16Mo3		0.12 –0.20	0.15 –0.35	0.40 –0.80	max. 0.040				0.25 –0.35						
4	9NiCuMoNb5-6-4		max. 0.17	0.25 –0.50	0.80 –1.20	max. 0.050	0.50 –0.80	max. 0.30	1.00 –1.30	0.25 –0.50				0.015 –0.045		
5	13CrMo4-5	T/P11	0.10 –0.17	0.10 –0.35	0.40 –0.70	max. 0.040		0.70 –1.10		0.45 –0.65						
6	11CrMo9-10	T/P22	0.08 –0.15	0.15 –0.40	0.30 –0.70	max. 0.040		2.00 –2.50		0.90 –1.20						
7	8CrMoNiNb9-10		max. 0.10	0.15 –0.50	0.40 –0.80	max. 0.050		2.00 –2.50	0.30 –0.80	0.90 –1.10				min. 10x%C		
8	7CrMoVTiB10-10	T/P24	0.05 –0.10	0.15 –0.45	0.30 –0.70	max. 0.020		2.20 –2.60		0.90 –1.10		0.05 –0.10	0.20 –0.30		0.0015 –0.007	max. 0.010
9		T/P23	0.04 –0.10	max. 0.50	0.10 –0.60	max. 0.030		1.90 –2.60		0.05 –0.30	1.45 –1.75		0.20 –0.30	0.02 –0.08	0.0005 –0.006	max. 0.030
10	X11CrMo9-1	T/P9	0.08 –0.15	0.25 –1.00	0.30 –0.60	max. 0.040		8.0 –10.0		0.90 –1.00						
11	X20CrMoNiV11-1		0.17 –0.23	0.15 –0.50	max. 1.00	max. 0.040		10.0 –12.5	0.30 –0.80	0.80 –1.20			0.25 –0.35			
12	X10CrMoVNb9-1	T/P91	0.08 –0.12	0.20 –0.50	0.30 –0.60	max. 0.040		8.00 –9.50	max. 0.40	0.85 –1.05			0.18 –0.25	0.06 –0.10		0.030 –0.070
13	X11CrMoWVNb9-1-1	T/P911	0.09 –0.13	0.10 –0.50	0.30 –0.60	max. 0.040		8.50 –9.50	0.10 –0.40	0.90 –1.10	0.90 –1.10		0.18 –0.25	0.06 –0.10	0.0005 –0.005	0.050 –0.090
14		T/P92	0.07 –0.13	max. 0.50	0.30 –0.60	max. 0.040		8.50 –9.50	max. 0.40	0.30 –0.60	1.50 –2.00		0.15 –0.25	0.04 –0.09	0.001 –0.006	0.030 –0.070
15		T/P122	0.07 –0.13	max. 0.50	max. 0.70	max. 0.040	0.30 –1.70	10.0 –12.5	max. 0.50	0.25 –0.60	1.50 –2.50		0.15 –0.30	0.04 –0.10	max. 0.005	0.040 –0.100

Table 3.1 FBB Alloy compositions (weight percent, wt.%)

Alloys #	Fe	Al	Cr	Ni	Mo	Hf	Zr	B	Nb	V	C	W	Ti
FBB-1	70	10	10	10	-	-	-	-	-	-	-	-	-
FBB-2	66.3	10	10	10	3.4	0.25	-	0.005	-	-	-	-	-
FBB-3	66.3	10	10	10	3.4	-	0.25	0.005	-	-		-	-
FBB-4	66.1	10	10	10	3.4	-	0.25	0.005	0.1	0.1	0.05	-	-
FBB-5	63.2	10	10	10	3.3	-	-	0.005	-	-	-	3.5	-
FBB-6	65.6	10	10	10	1.7	-	0.25	0.02	-	-	-	2.5	-
FBB-7	68.3	8	10	10	3.4	-	0.25	0.005	-	-	-	-	-
FBB-8	69.8	6.5	10	10	3.4	-	0.25	0.005	-	-	-	-	-
FBB-8W1	67.8	6.3	9.7	9.7		-	0.23	0.005	-	-	-	6.3	-
FBB-8W2	68.8	6.4	9.8	9.8	1.7	-	0.24	-	-	-	-	3.2	-
FBB-9	71.3	5	10	10	3.4	-	0.25	0.005	-	-	-	-	-
FBB-10	71.2	6.5	10	10	2.0	-	0.25	0.005	-	-	-	-	-
FBB-11	72.7	5	10	10	2.0	-	0.25	0.005	-	-	-	-	-
FBB-12	72.3	4	10	10	3.4	-	0.25	0.005	-	-	-	-	-
FBB-13	73.3	3	10	10	3.4	-	0.25	0.005	-	-	-	-	-
FBB-14	69.6	6.5	10	10	3.4	-	0.5	0.005	-	-	-	-	-
FBB-15	69.1	6.5	10	10	3.4	-	1	0.005	-	-	-	-	-
FBB-16	68.8	6.5	10	10	3.4	-	0.25	0.005	-	-	-	-	1
FBB-17	70.3	6	10	10	3.4	-	0.25	0.005	-	-	-	-	-
FBB-18	61.3	10	10	15	3.4	-	0.25	0.005	-	-	-	-	-
FBB-19	56.3	10	10	20	3.4	-	0.25	0.005	-	-	-	-	-

Table 3.2 Concentration of the alloying elements in FBB alloys (wt.%)

Alloys	Fe	Cr	Ni	Al	B	Mo	Zr	Hf
FBB-2 Nominal	Balance	10	10	10	0.005	3.4	-	0.25
FBB-2	66.53	9.88	9.97	9.84	0.005	3.37	-	0.25
FBB-3 Nominal	Balance	10	10	10	0.005	3.4	0.25	-
FBB-3	66.57	9.88	10.05	9.81	0.005	3.37	0.25	-

Table 4.1 Composition (in atomi percent, at.%) of phases in an Fe-12.7 Al-10.2 Cr-9.0 Ni-1.9 Mo (in at.%). In the case of matrix α and primary β' precipitate, both analytical electron microscopy (AEM) and atom-probe tomography (APT) techiniques were employed.

Phase	Technique	**Fe**	**Al**	**Ni**	**Cr**	**Mo**
Matrix α	AEM	75.9	8.2 ± 0.1	2.1 ± 0.2	11.9 ± 0.8	2.1 ± 0.7
	APT	75.1 ± 1.0	7.2 ± 0.6	3.0 ± 0.5	11.9 ± 0.7	3.1 ± 0.4
Primary β' precipitate	AEM	14.3 ± 1.5	44.8 ± 0.6	39.2	1.5 ± 0.2	0.2 ± 0.1
	APT	12.7 ± 0.1	43.6 ± 0.9	41.2 ± 1.1	0.8 ± 0.1	1.4 ± 0.1
Secondary β' precipitate	APT	26.9 ± 2.1	41.6 ± 3.4	26.3 ± 3.7	3.3 ± 0.3	1.7 ± 0.6
α in primary β' precipitate (as in Figure 4.2a)	APT	73.1 ± 3.4	8.1 ± 1.4	4.2 ± 1.4	11.4 ± 1.6	2.5 ± 0.4

Table 5.1 The elemental concentrations in the β/β' phases, and the equivalent scattering lengths

Element	c_i^{β}	$c_i^{\beta'}$	$c_{i,ce}^{\beta'}$	$c_{i,co}^{\beta'}$	b_i (10^{-15} m)	$b_{i,ce}^{\beta'}$ (10^{-15} m)	$b_{i,co}^{\beta'}$ (10^{-15} m)	b_i^{β} (10^{-15} m)
Fe	0.735	0.106	0.045	0.16	9.45	0.4253	1.512	6.9458
Al	0.093	0.436	0.933	0	3.45	3.2188	0	0.3209
Ni	0.017	0.436	0	0.826	10.3	0	8.5078	0.1751
Cr	0.124	0.012	0.016	0.008	3.64	0.0582	0.0291	0.4507
Mo	0.030	0.0056	0.006	0.006	6.72	0.0403	0.0403	0.2015
$\sum$	0.999	0.996	1	1	-	3.7426	10.0892	8.0939

Table 5.2 Lattice parameters as a function of temperature

Temperature (K)	β (A)	β' (A)	δ
300	2.8827 ± 0.0011	2.8752 ± 0.0004	-2.61×10^{-3}
525	2.8953 ± 0.0009	2.8925 ± 0.0003	-0.97×10^{-3}
750	2.9019 ± 0.0008	2.9003 ± 0.0004	-0.55×10^{-3}
873	2.9071 ± 0.0010	2.9071 ± 0.0003	0

Table 5.3 Atomic volumes of alloying elements in the β' NiAl precipitate

Atom	x_{Al}[22]	x_{Ni}[22]	$da/dx_i(nm)$	$\Omega_i(nm^3)$
Fe	0.20	0.80	-0.00267 [33]	0.01080
Cr	0.69	0.31	-0.0115[34]	0.01091
Mo	0.46	0.54	0.0547 [35]	0.01873

Table 6.1 Composition [**mass%** (at.%)] of β and β' phases in prototype FBB alloys, aged at 700˚C for 100 hrs. The alloys FBB-3 to FBB-12 were determined using thin foils in AEM. Alloy FBB-13 was determined by APT.

Alloy#	(α-Fe)-matrix (β)				
	Al	Cr	Ni	Mo	Fe
FBB-3	**9.8 ± 0.3**	**11.8 ± 0.9**	**2.3 ± 0.2**	**4.8 ± 0.9**	**71.3 (bal.)**
	(18.6)	(11.6)	(2.0)	(2.6)	(65.3)
FBB-8	**4.1 ± 0.1**	**11.5 ± 0.9**	**2.3 ± 0.2**	**3.7 ± 0.7**	**78.4 (bal.)**
	(8.2)	(11.9)	(2.1)	(2.1)	(75.7)
FBB-12	**2.3 ± 0.1**	**10.9 ± 0.9**	**3.5 ± 0.3**	**3.7 ± 0.7**	**79.6 (bal.)**
	(4.7)	(11.5)	(3.3)	(2.1)	(78.4)
FBB-13	**1.3**	**11.2**	**3.1**	**3.1**	**81.2**
	(2.6)	(12)	(2.9)	(1.8)	(80.6)
Alloy#	NiAl-type precipitate (β')				
	Al	Cr	Fe	Mo	Ni
FBB-3	**30.2 ± 0.8**	**1.3 ± 0.1**	**15.3 ± 1.3**	**0.6 ± 0.1**	**52.7 (bal.)**
	(48.2)	(1.1)	(11.8)	(0.3)	(38.6)
FBB-8	**27.4 ± 0.7**	**1.8 ± 0.2**	**18.1 ± 1.6**	**0.5 ± 0.1**	**52.2 (bal.)**
	(44.8)	(1.5)	(14.3)	(0.2)	(39.2)
FBB-12	**24.8 ± 0.7**	**1.2 ± 0.1**	**16.9 ± 1.5**	**0.3 ± 0.1**	**56.9 (bal.)**
	(41.5)	(1.1)	(13.6)	(0.1)	(43.7)
FBB-13	**21.2**	**1.9**	**21.7**	**0.5**	**54.5**
	(36.5)	(1.7)	(18.1)	(0.3)	(43.1)

Table 7.1 Nominal compositions of the model alloys (at.%). The actual composition of FBB-8 determined by wet chemical analyses is in a very good agreement with the nominal one.

Alloys #	Fe	Al	Cr	Ni	Mo
FBB-3	60.6	18.9	9.8	8.7	1.8
FBB-8 Nominal	66.1	12.7	10.2	9.0	1.9
FBB-8 Actual	66.3	12.6	10.1	9.0	1.8
FBB-12	70.2	8.0	10.4	9.2	1.9
FBB-13	71.9	6.1	10.5	9.3	1.9
FBB-18	56.1	18.9	9.8	13.0	1.8
FBB-19	51.6	19.0	9.9	17.4	1.8

Table 7.2 Elemental partitioning (at.%) and precipitate volume fractions (V_f) of the studied alloys. The standard error (σ) of the concentration estimated by APT is ~ 0.03%, given by $\sigma = \sqrt{C(1-C)N}$, where C is the concentration, and N is the total number of atoms in the measured volume.

β Matrix	Fe	Al	Ni	Cr	Mo	100-V_f
FBB-3	69.0	14.5	2.2	11.7	2.5	80
FBB-8	75.1	7.2	3.0	11.9	3.1	82
FBB-12	79.3	3.0	3.1	12.1	2.4	86.4
FBB-13	80.6	2.6	3.0	12.0	1.8	92.7
FBB-18	73.5	9.3	1.7	12.4	3.0	72.5
FBB-19	77.0	4.9	1.5	14	2.5	62.5
β' Precipitate	Fe	Al	Ni	Cr	Mo	V_f
FBB-3	12.2	45.2	40.3	1.5	0.8	20
FBB-8	12.7	43.6	41.2	0.8	1.4	18
FBB-12	12.0	38.5	48.2	0.6	0.2	13.6
FBB-13	18.1	36.5	43.1	1.7	0.3	7.3
FBB-18	10.6	43.6	43.6	1.2	0.6	27.5
FBB-19	10.4	43.2	44.1	0.8	1.1	37.5

Table 7.3 Comparison of the compositions (at.%) between the unrolled (HT2) and hot-rolled (HR) alloy FBB-8.

FBB-8	Phase	Fe	Al	Ni	Cr	Mo
HT2	β Matrix	75.1 ± 1.0	7.2 ± 0.6	3.0 ± 0.5	11.9 ± 0.7	3.1 ± 0.4
HR	β Matrix	74.1 ± 3.4	8.1 ± 1.4	3.7 ± 1.4	11.7 ± 1.6	2.1 ± 0.4
HT2	β' Precipitates	12.7 ± 0.1	43.6 ± 0.9	41.2 ± 1.1	0.8 ± 0.1	1.4 ± 0.1
HR	β' Precipitates	14.5 ± 0.4	41.9 ± 0.3	40.7 ± 0.2	1.1 ± 0.1	1.4 ± 0.1

Table 8.1 Nominal compositions of the NiAl strengthened ferritic model alloys (at.%)

Alloys #	Fe	Al	Cr	Ni	Mo
FBB-8	66.1	12.7	10.2	9.0	1.9
FBB-9	68.5	9.9	10.3	9.1	1.9
FBB-12	70.2	8.0	10.4	9.2	1.9
FBB-13	71.9	6.1	10.5	9.3	1.9
FBB-18	56.1	18.9	9.8	13	1.8

Table 8.2 Elemental partitioning by both experimental measurements and thermodynamic predictions (at.%)

(αFe)-Matrix		Fe	Al	Ni	Cr	Mo	V_f
FBB-8	Measured	75.1	8.2	2.1	11.9	2.1	82
	Calculated	*76.5*	*7.0*	*2.3*	*11.9*	*2.2*	*84*
FBB-12	Measured	79.3	3.0	3.1	12.1	2.4	86.4
	Calculated	*77*	*4.6*	*4.7*	*11.6*	*2.1*	*89.2*
FBB-18	Measured	73.5	9.3	1.7	12.4	3.0	72.5
	Calculated	*74.1*	*8.4*	*1.5*	*13.5*	*2.5*	*71.8*
NiAl-type Precipitate		Fe	Al	Ni	Cr	Mo	V_f
FBB-8	Measured	12.7	43.6	41.2	0.8	1.4	18
	Calculated	*11.8*	*43.3*	*44.2*	*0.6*	*0.02*	*16*
FBB-12	Measured	12.0	38.5	48.2	0.6	0.2	13.6
	Calculated	*15.9*	*36.7*	*46.3*	*0.9*	*0.1*	*10.8*
FBB-18	Measured	10.6	43.6	43.6	1.2	0.56	27.5
	Calculated	*11.1*	*45.7*	*42.7*	*0.5*	*0.02*	*28.2*

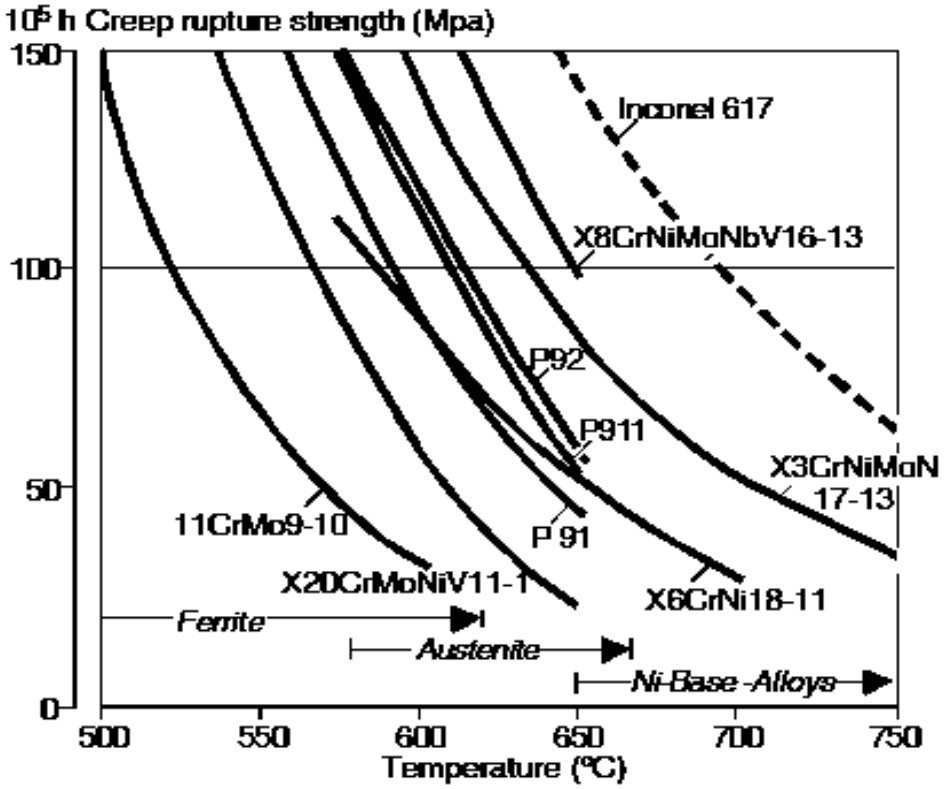


Figure 1.1 The present status of the development of creep-resistant steels for power plants

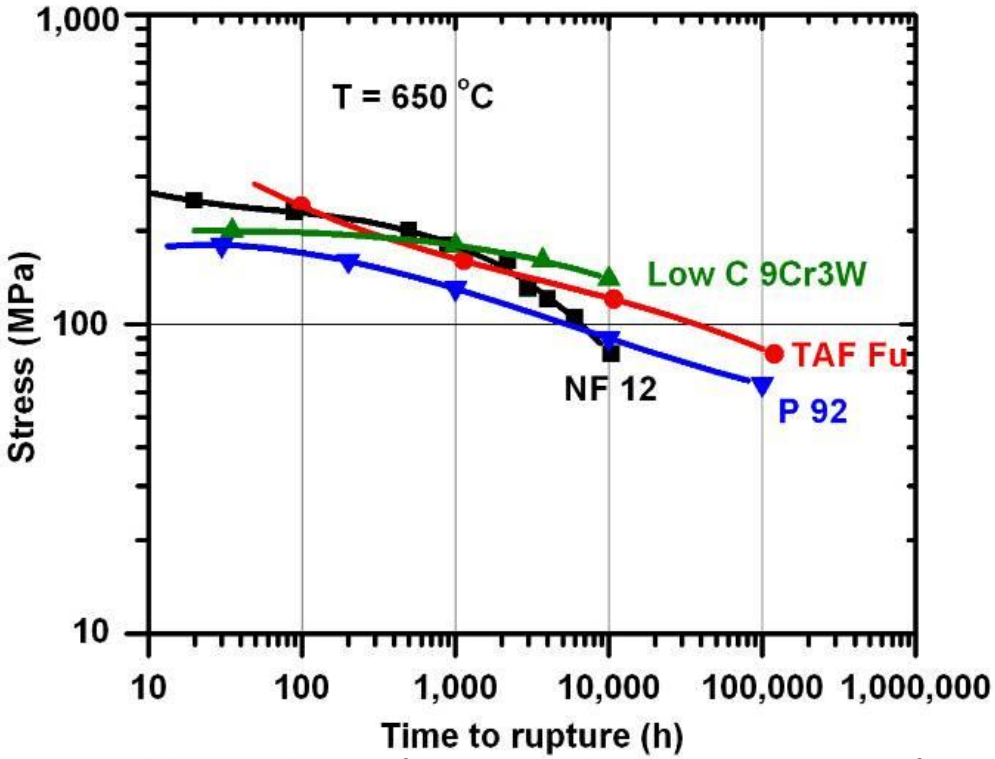


Figure 1.2 Sigmoidal creep behavior of the recently-developed creep-resistant ferritic steels

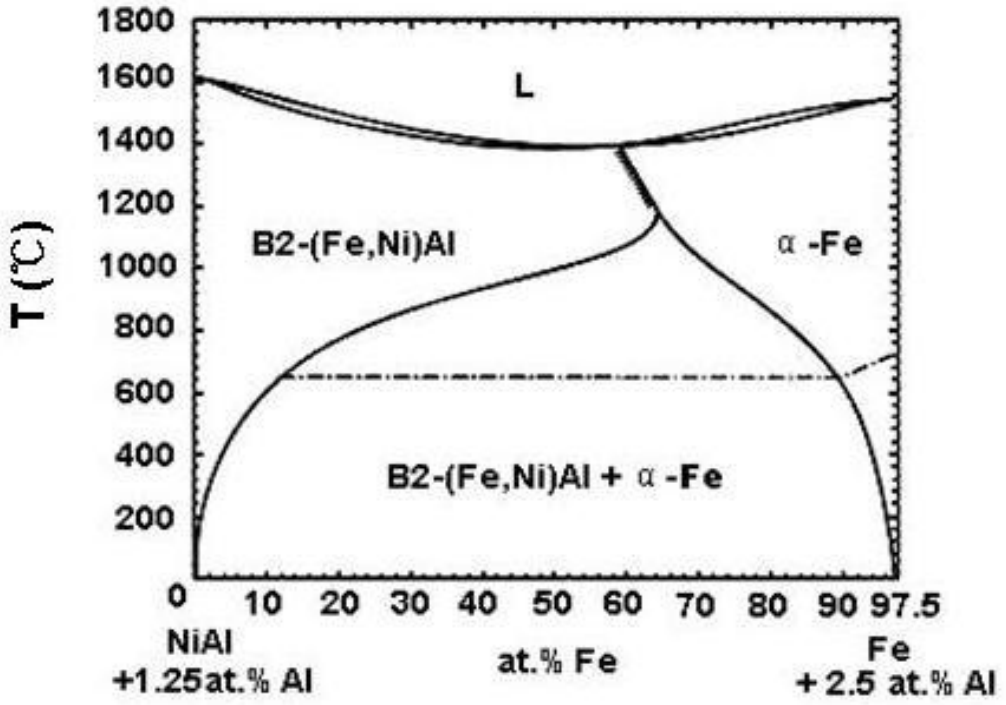


Figure 1.3 Pseudo-binary phase diagram from $Ni_{48.75}Al_{51.25}$ to $Fe_{97.5}Al_{2.5}$: miscibility gap between ordered (B2) and disordered (α-Fe) BCC phases

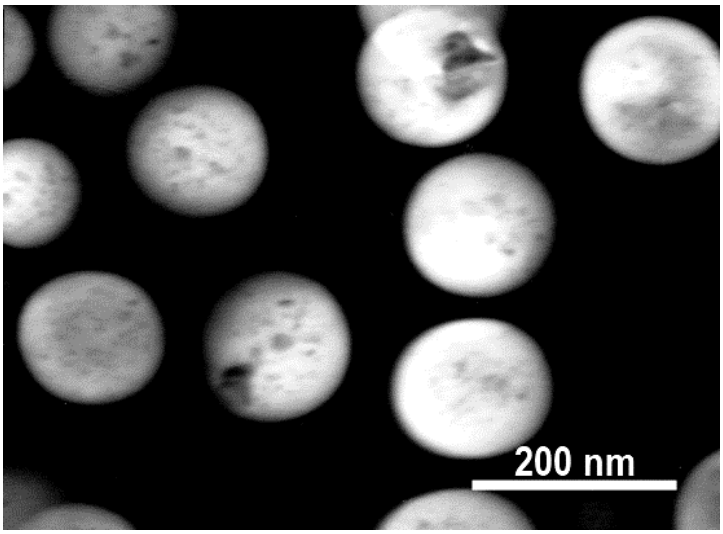


Figure 1.4 TEM microstructures of a Fe-Al-Ni-Cr alloy, solution treated at 1,200°C for 30 minutes, followed by aging at 700 °C for 100 hours, provided by Dr. G. Ghosh from Northwestern University

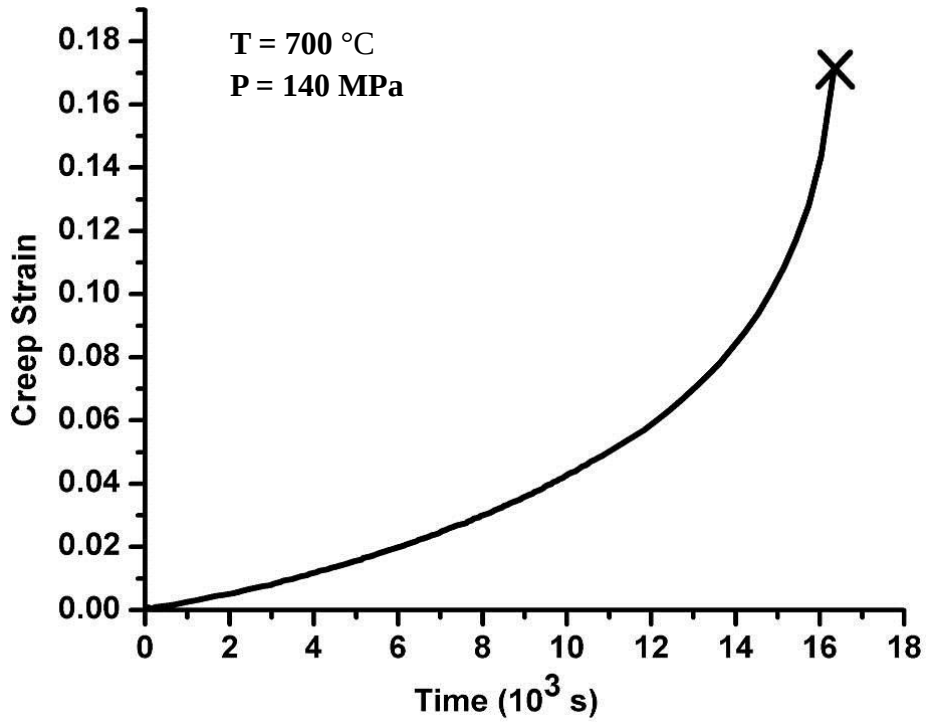
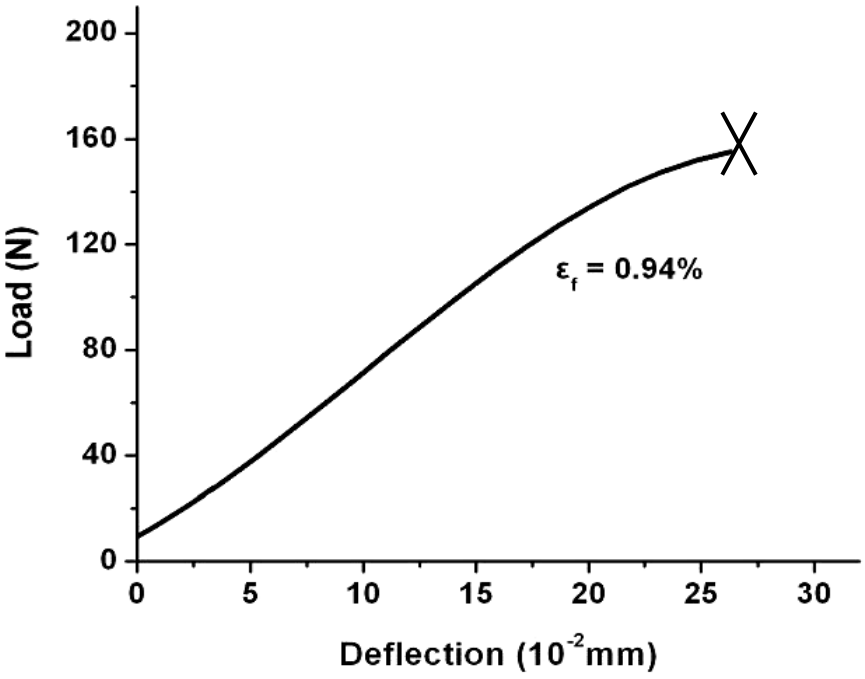
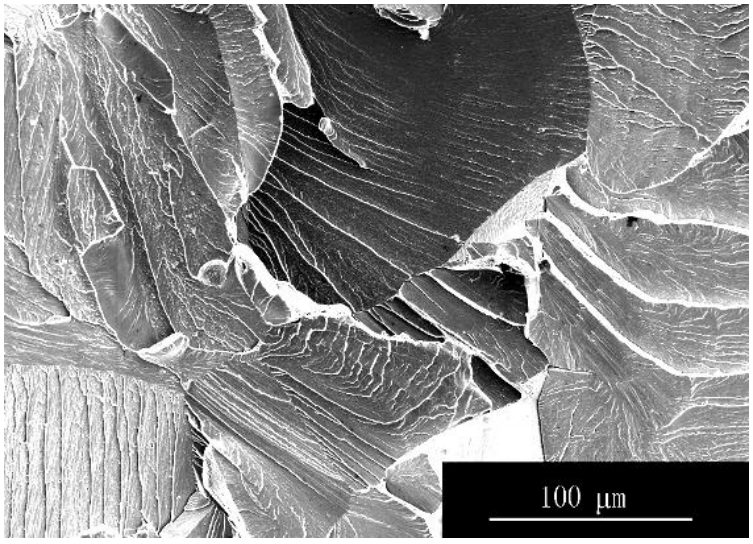


Figure 1.5 Tension creep curve of a previously designed alloy FBB-8 (Fe-6.5Al-10Ni-10Cr) at a load of 140 MPa and a temperature of 700°C



(a)



(b)

Figure 1.6 (a) Bending load and deflection curve of a recently-developed Fe-Al-Ni-Cr ferritic steel (FBB-8) and (b) its fracture surface at room temperature

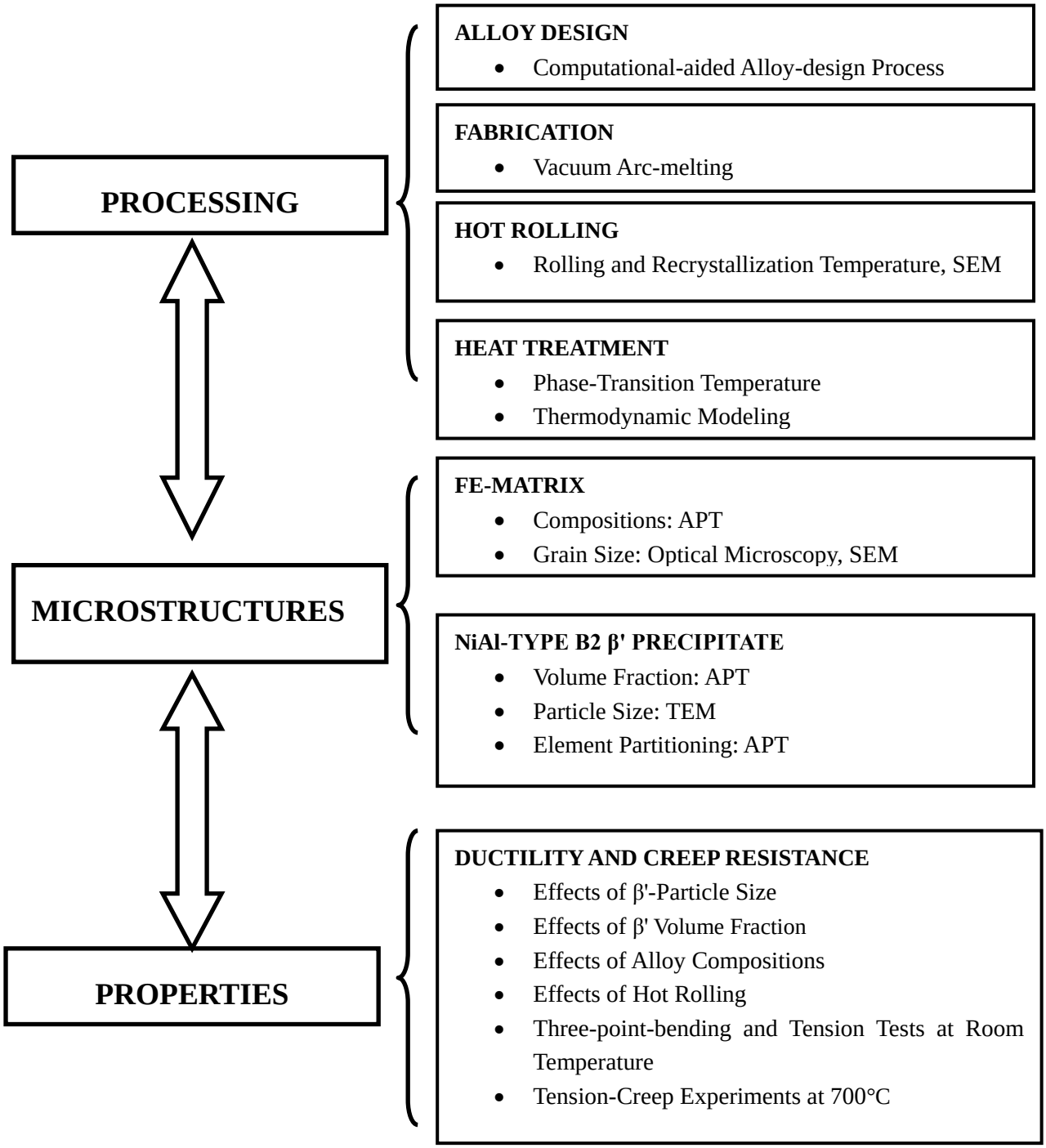


Figure 1.7 Schematic diagram of the proposed research

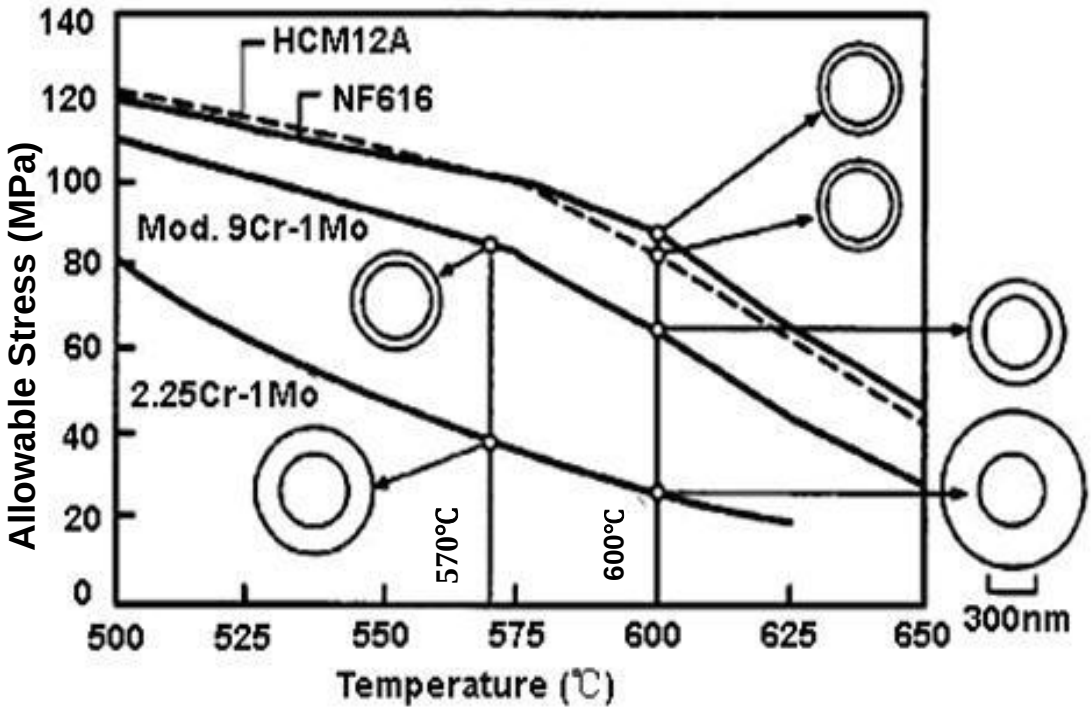
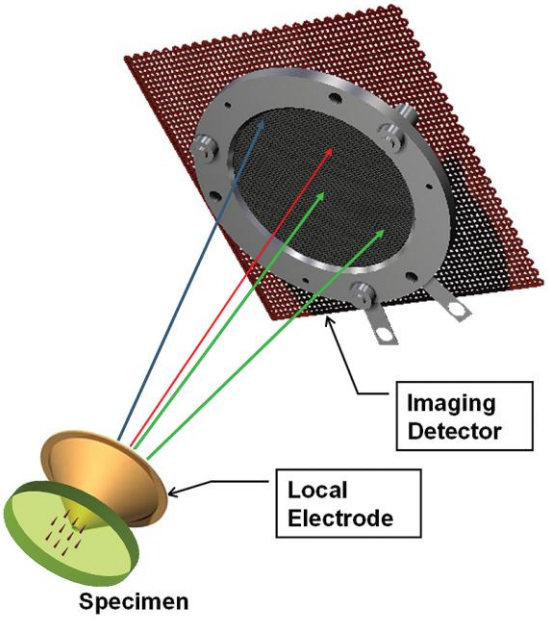
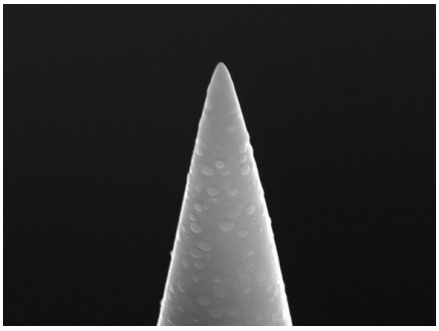


Figure 1.8 Comparison of allowable stresses and a sectional view of main steam pipes designed at 570 and 600℃ [3]



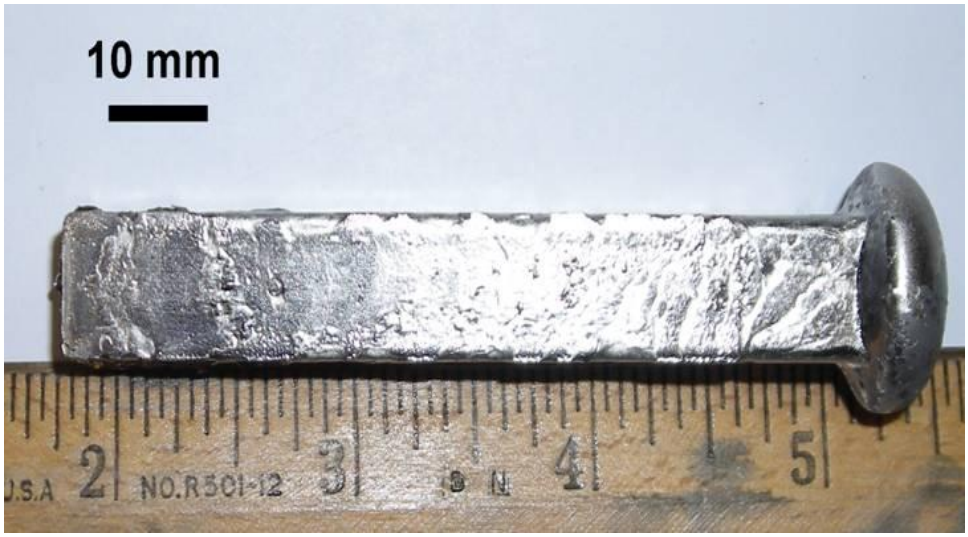
(a)



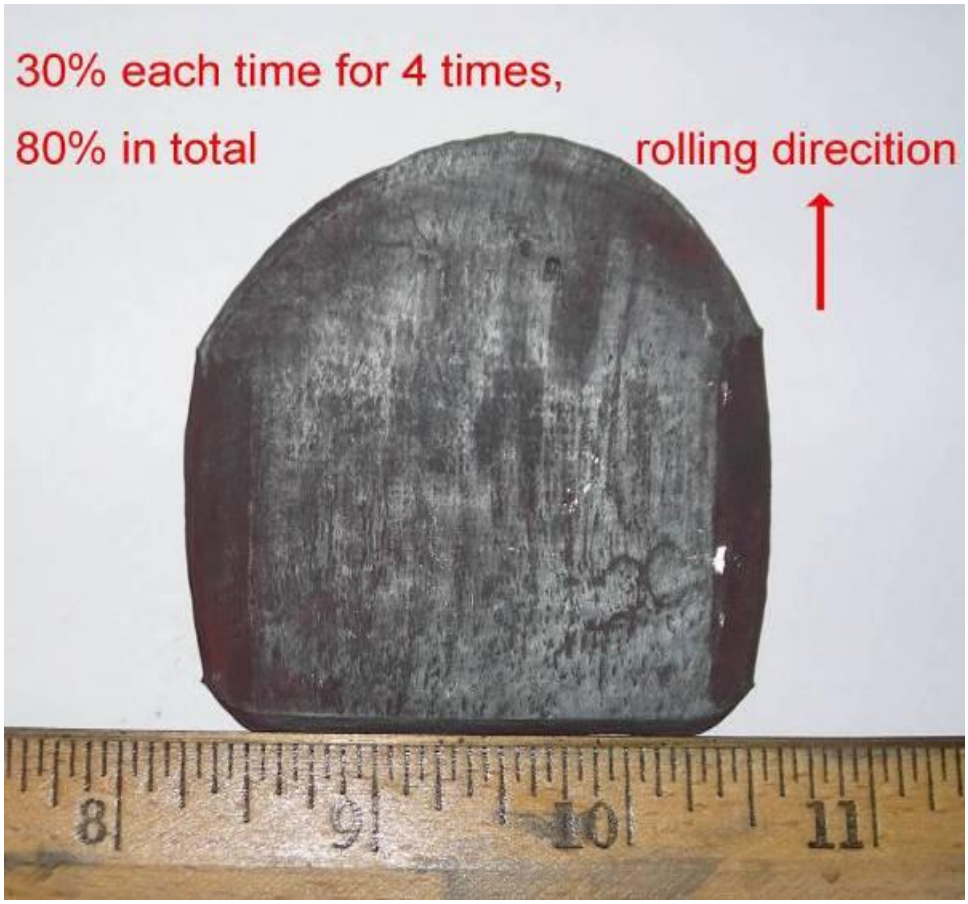


(b) (c)

Figure 2.1 (a) IMAGO atom probe, (b) schematic of atom probe tomography (APT), and (c) a representative APT sample



(a)



(b)

Figure 3.1 (a) As-cast ingot, and (b) after hot-rolling with 80% reduction in thickness

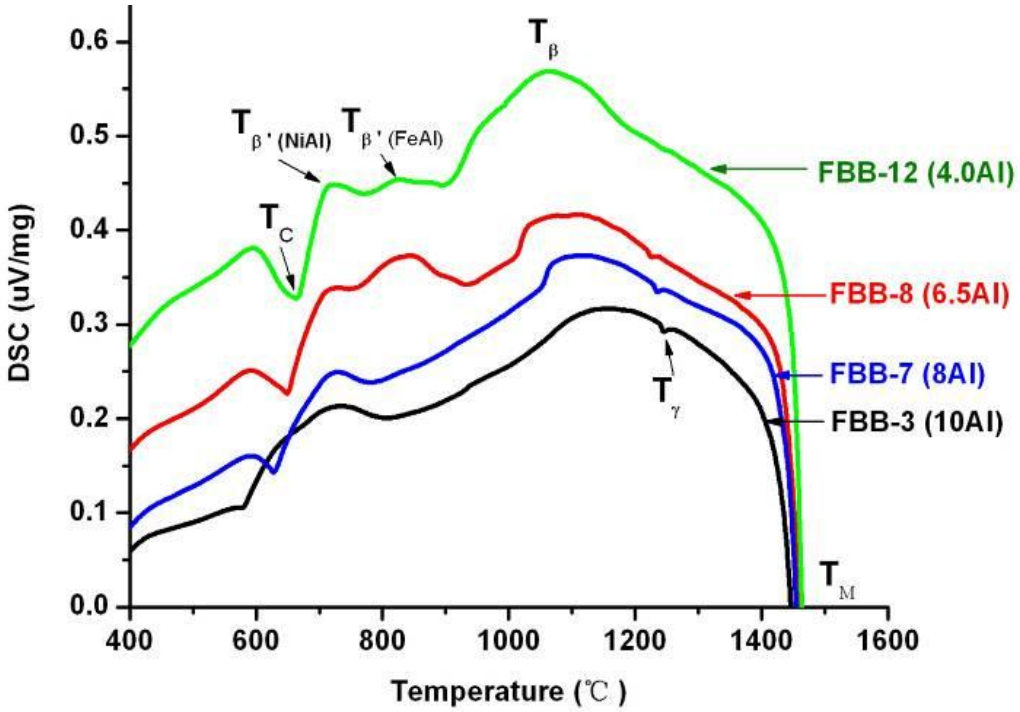


Figure 3.2 Solvus temperature of NiAl decreases as reducing the Al%

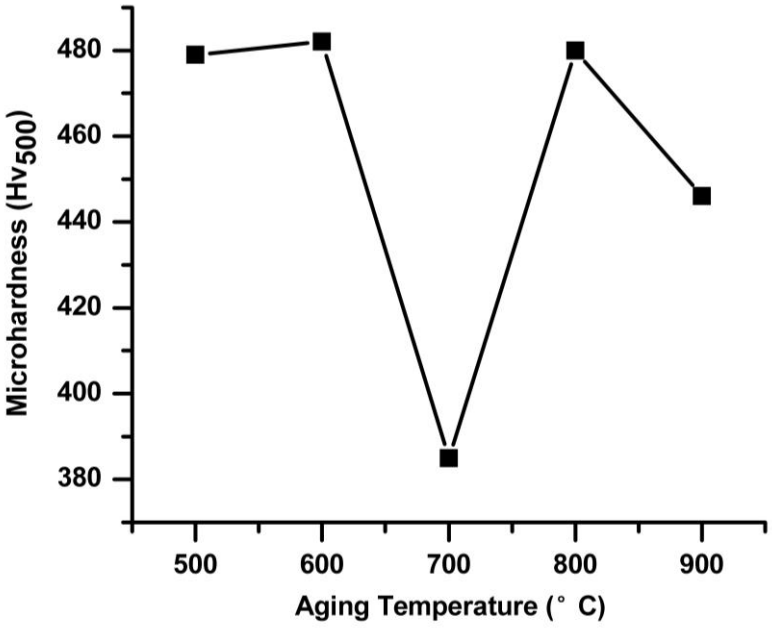


Figure 3.3 Microhardnesses of hot-rolled FBB-8 after aging at different temperatures for 1 hour

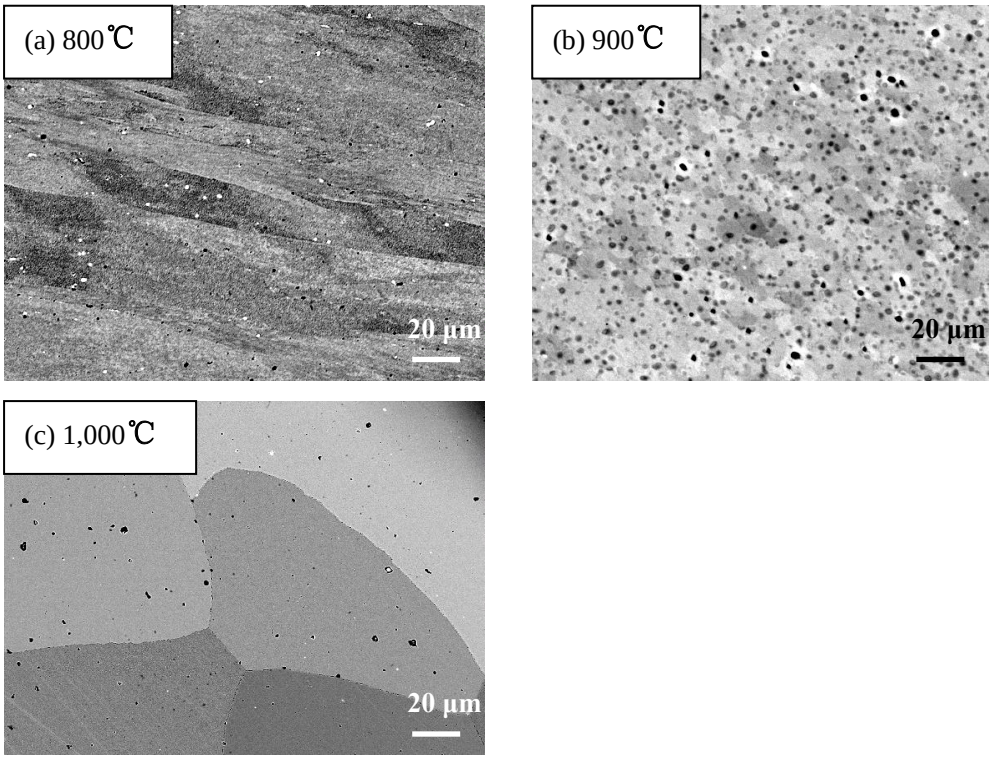


Figure 3.4 SEM micrographs showing the microstructures of hot-rolled FBB-8 after aging at different temperatures for 1 hour

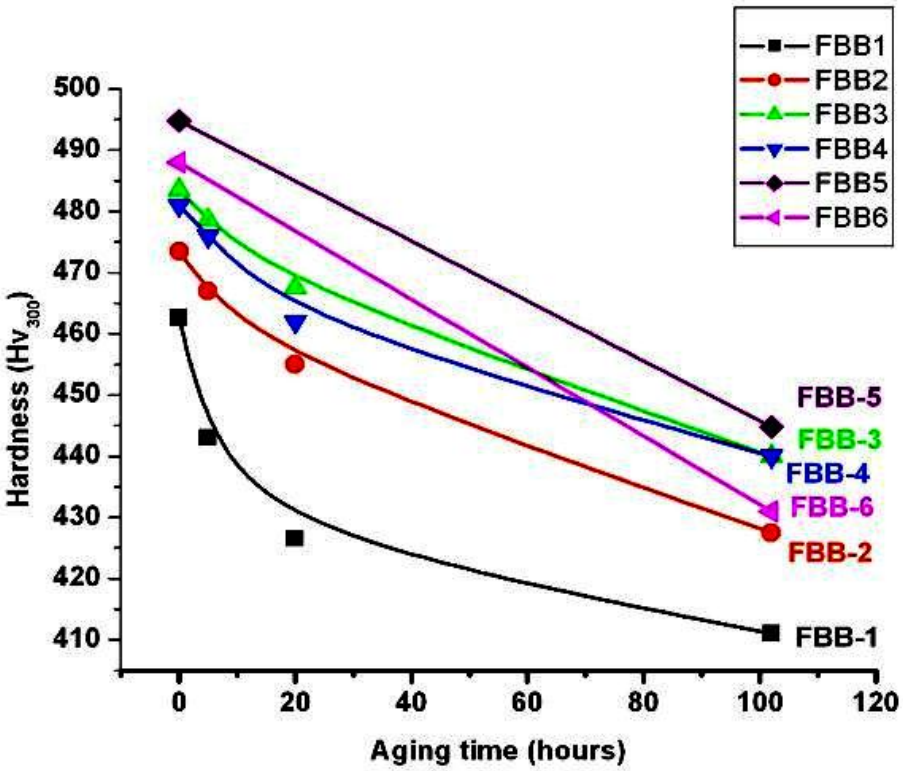


Figure 3.5 Hardness of the designed alloys decrease as the aging time increases, the alloy compositions can be referred to Table 3.1

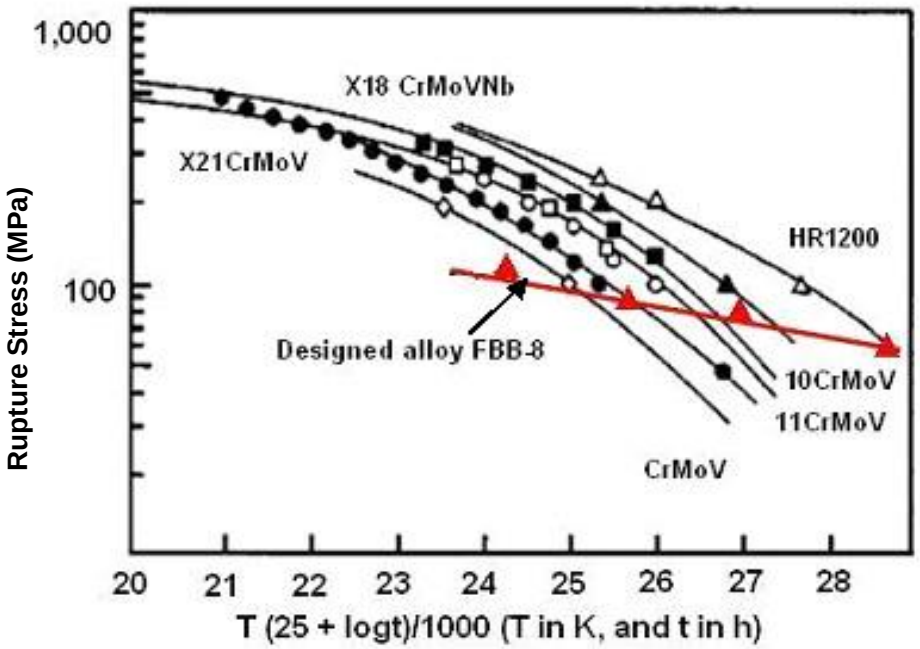


Figure 4.1 A comparison of the Larson-Miller parameter plots between FBB-8 and other Fe-based materials candidates for steam turbine applications, where the LMP is calculated by T(25 + log t)/1000. Tensile creep tests were performed at 700°C under loads of 140 MPa, 100 MPa, 80 MPa, and 60 MPa.

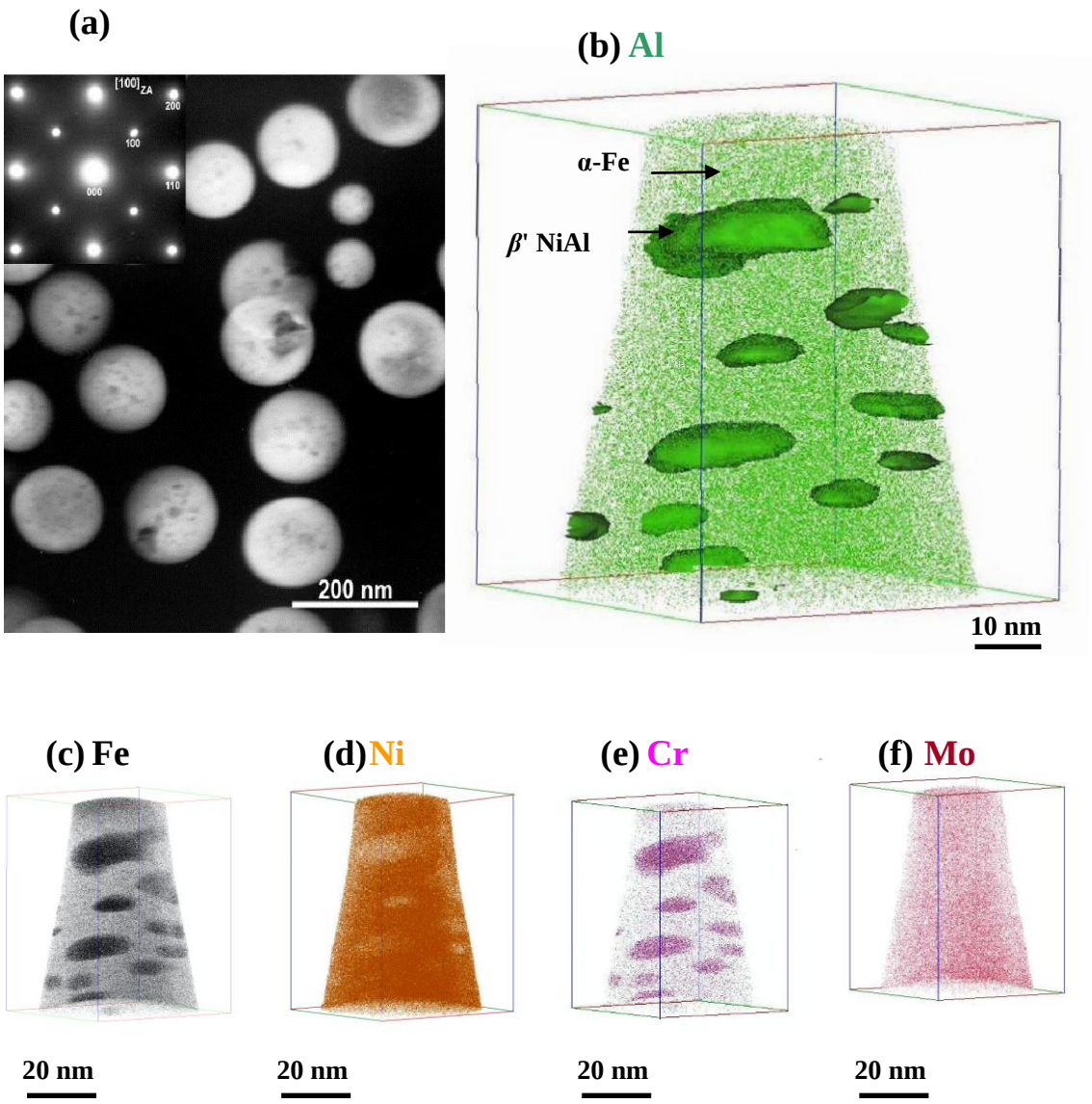


Figure 4.2 (a) Dark field TEM micrograph showing β' precipitates (bright regions) and selected area diffraction pattern (inset) with a zone axis of [100], and APT characterization of a β' precipitate as well as the dark regions [see Figure 4.2a)] inside the precipitate: (b) Al atom map and corresponding 15 % Al iso-concentration surface, (c) Fe map, (d) Ni map, (e) Cr map, and (f) Mo map.

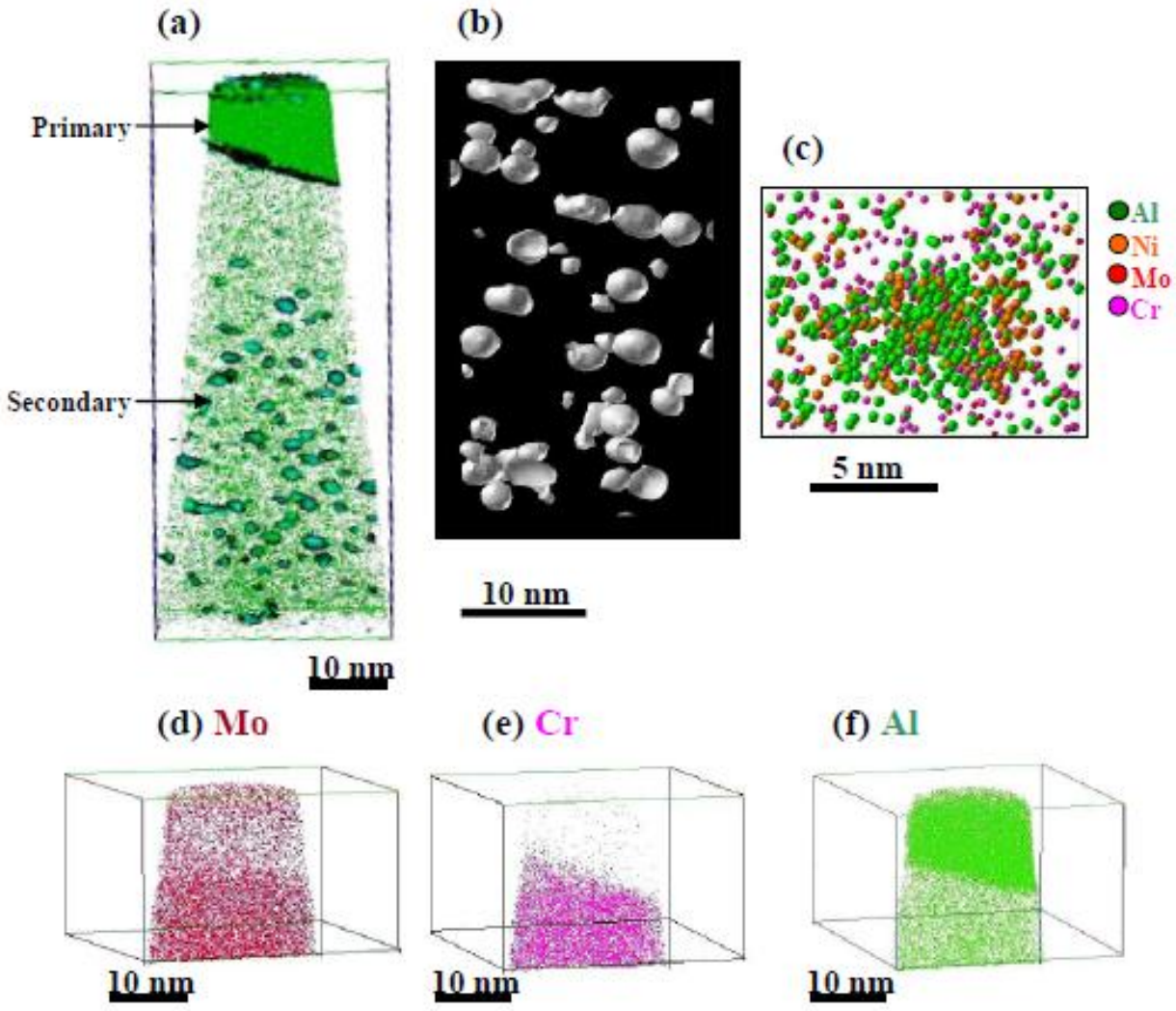


Figure 4.3 APT characterization of primary and secondary β' precipitates: (a) corresponding 15 at.% Al iso-concentration surface, (b) morphology of secondary ultrafine β' precipitates, (c) selected atom map of one ultrafine β' precipitates, (d) Mo atom map, (e) Cr atom map, and (f) Al atom map. The total number of atoms analyzed is 3,532,698.

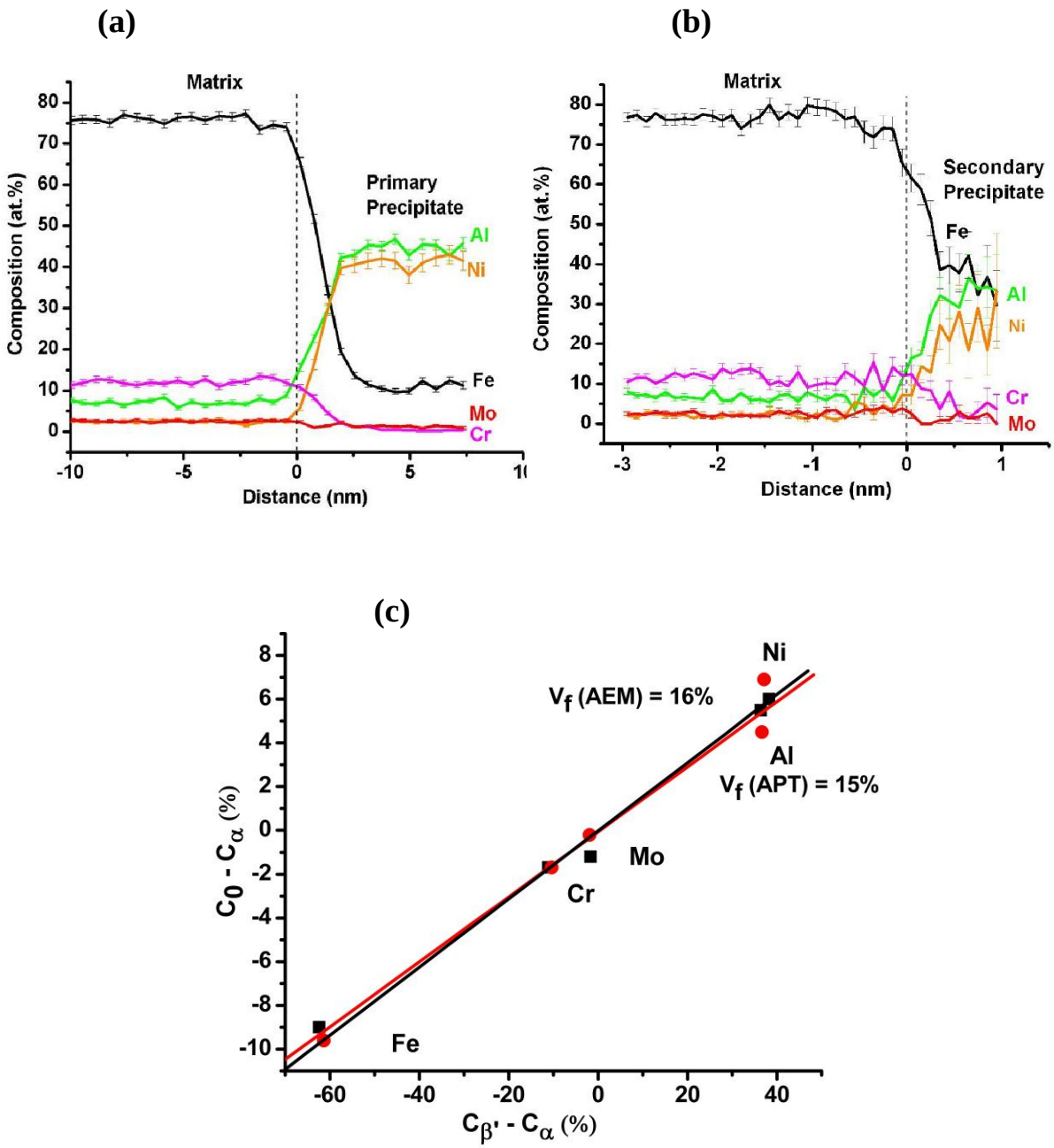


Figure 4.4 The composition profiles of (a) the primary β' precipitates, (b) secondary β' precipitates, and (c) the volume fraction of primary β' estimated by both AEM and APT.

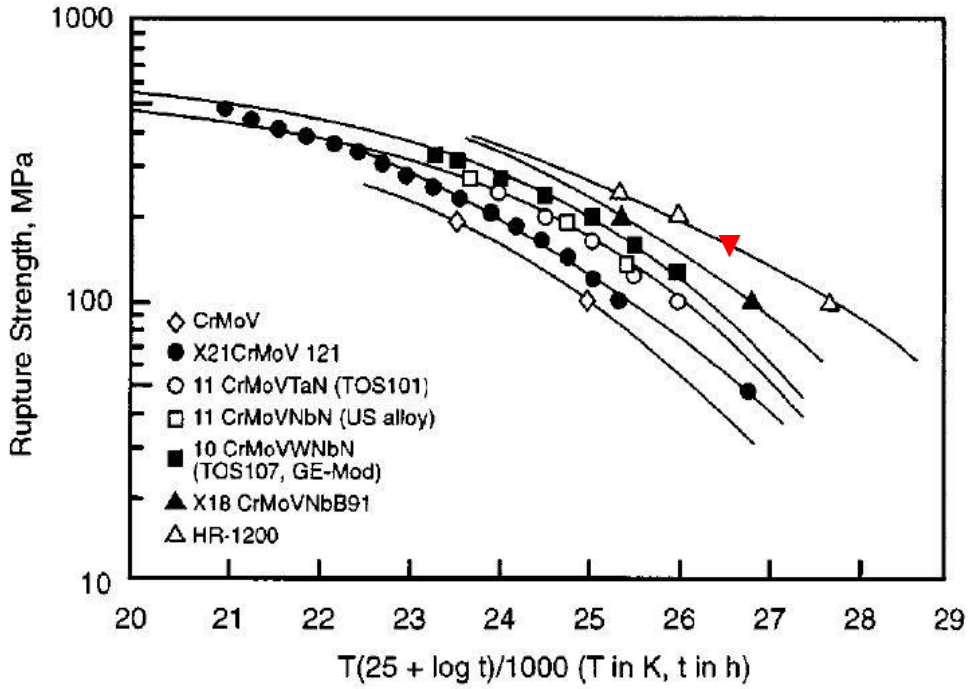


Figure 5.1 Comparison of the LMPs at 140 MPa between FBB-18 and other ferrite-based candidate materials for steam turbine applications

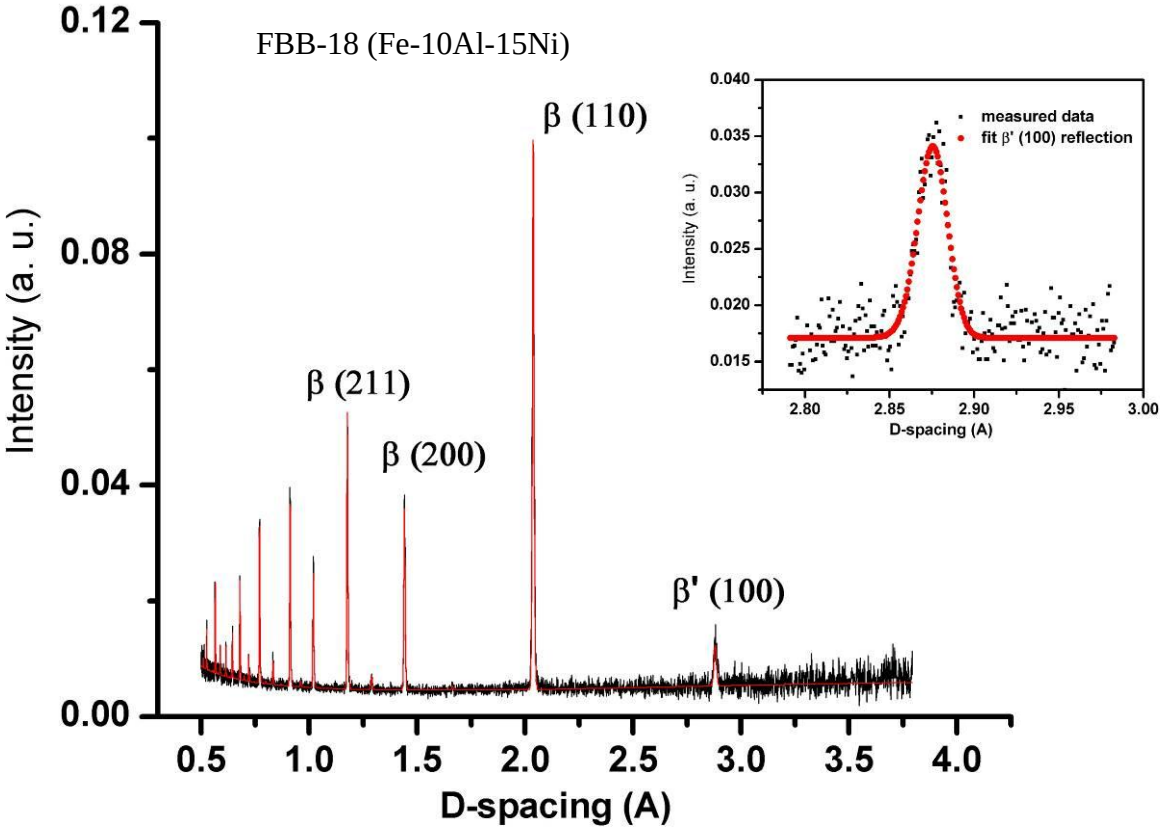
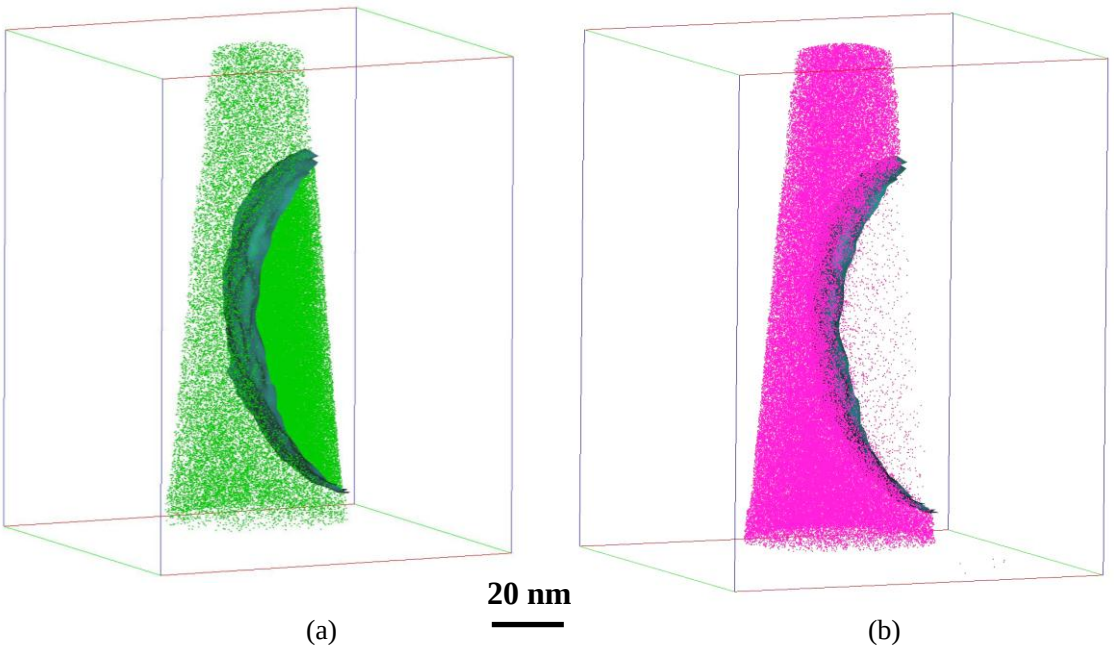
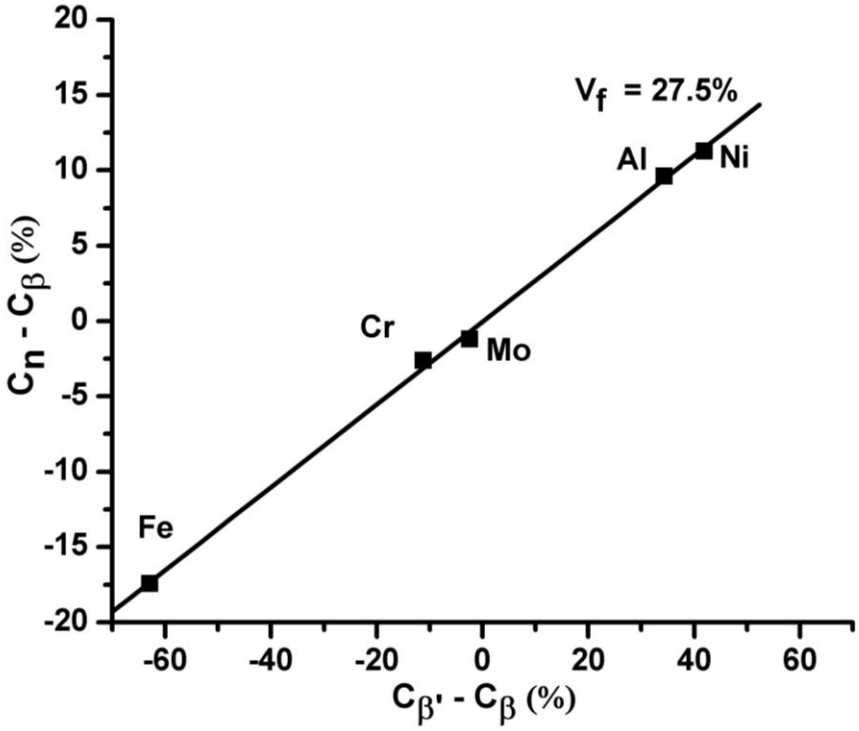


Figure 5.2 Representative neutron diffraction pattern and the single peak fitting result of the β' (100) superlattice reflection



(a) (b)



(c)

Figure 5.3 (a) Atom map of Al and 15% Al iso-concentration surface, (b) atom map of Cr, and (c) the volume fraction of primary *β'* estimated by lever rule

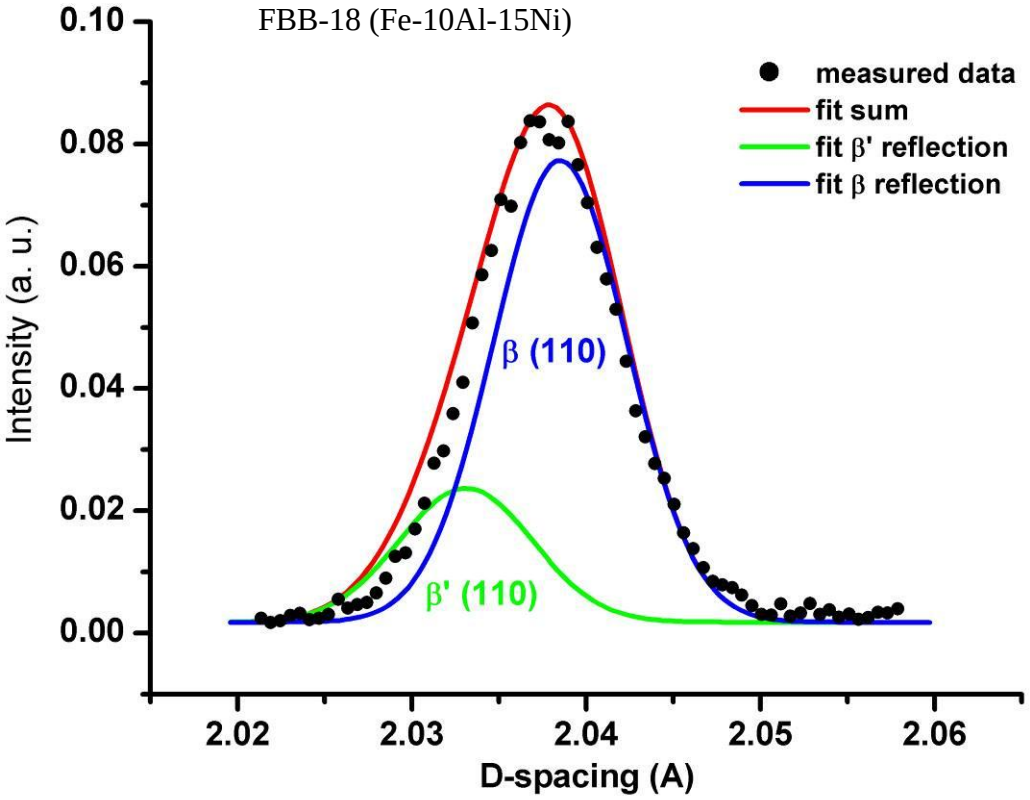


Figure 5.4 The separation of a ND fundamental reflection (100)

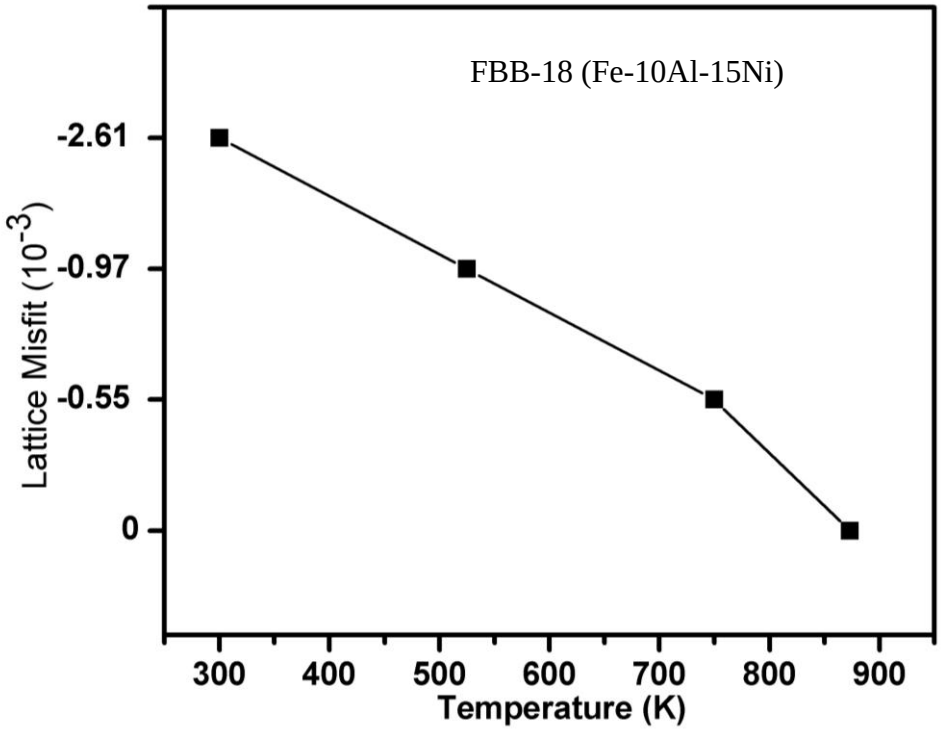


Figure 5.5 Lattice misfit between the matrix and precipitates as a function of temperature

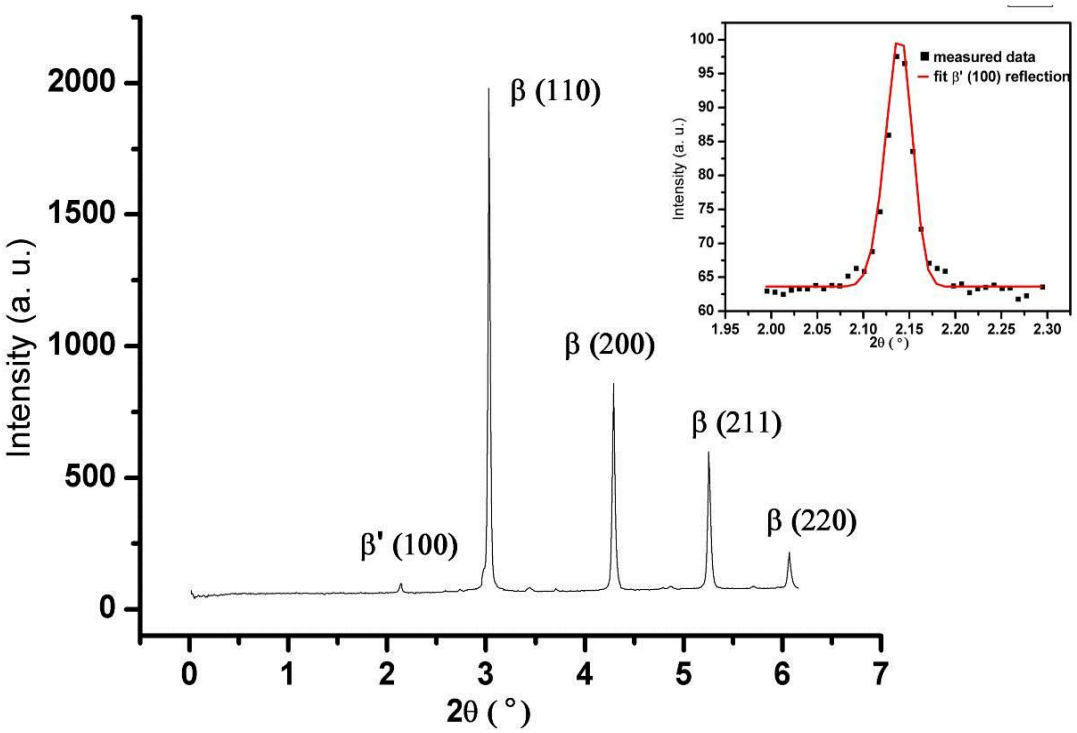


Figure 5.6 Representative XRD pattern and the single peak fitting result of the β' (100) superlattice reflection

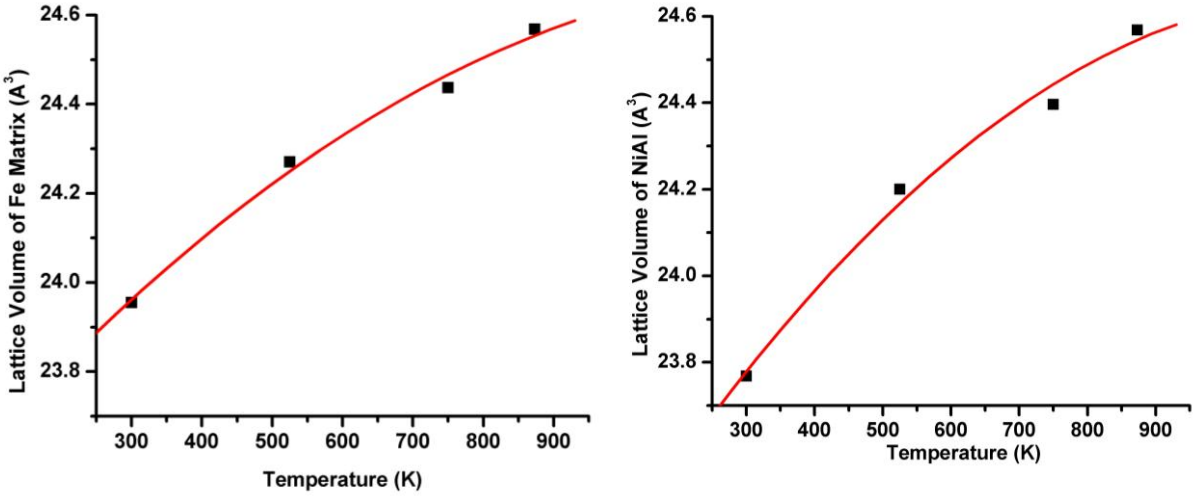
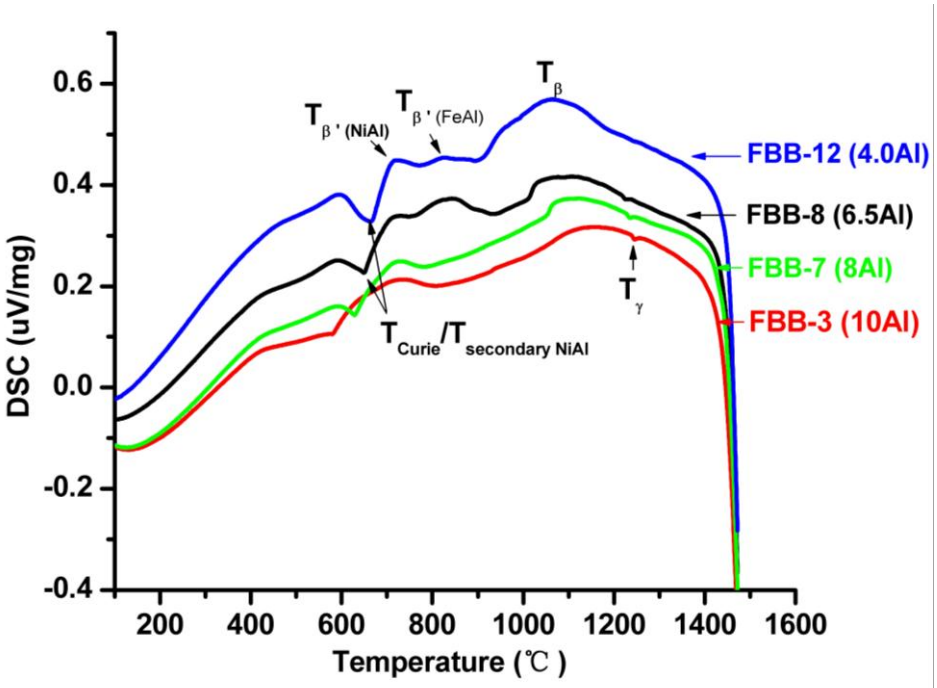
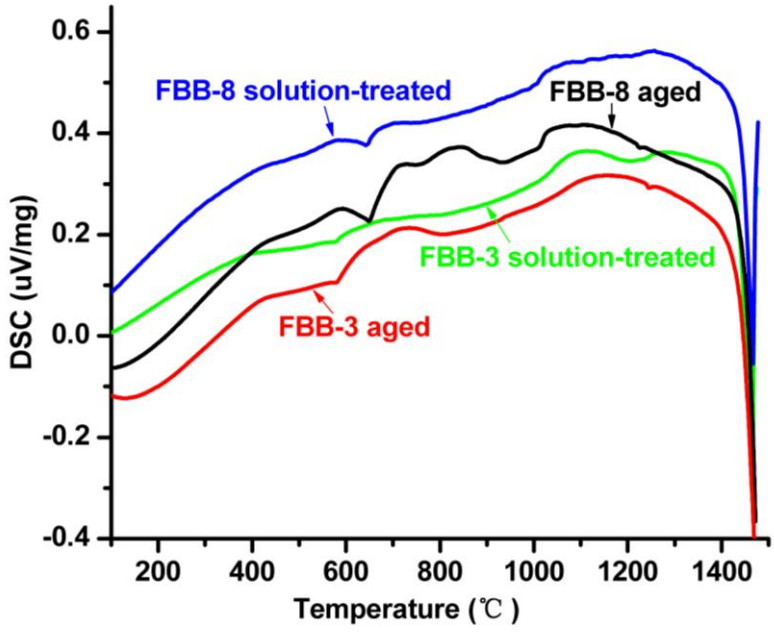


Figure 5.7 Lattice volume of the matrix (a) and precipitates (b) as a function of temperature

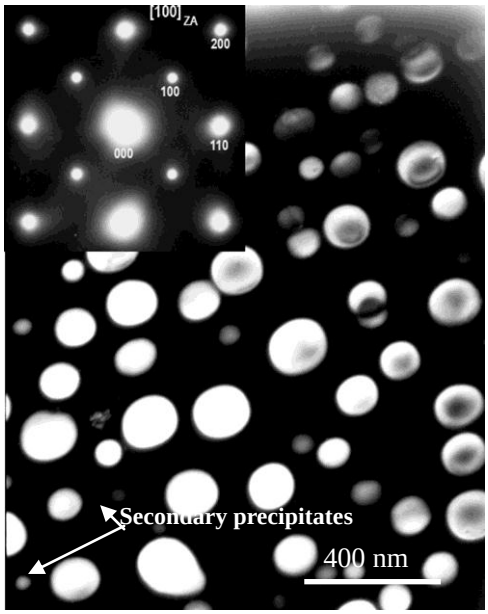


(a)

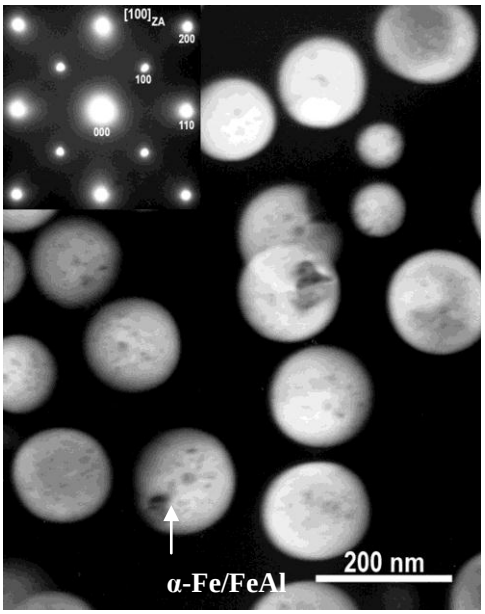


(b)

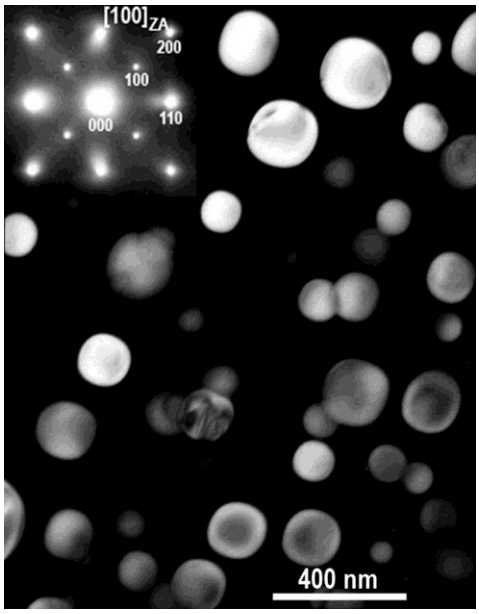
Figure 6.1 (a) The heating curves from the DSC analysis of the alloys with different Al% showing a phase transition peak at a temperature higher than $T_{\beta'(NiAl)}$. This is most likely to be the phase separation of FeAl inside NiAl. (b) A comparison between the DSC curves of the solution-treated and aged alloys.



(a)

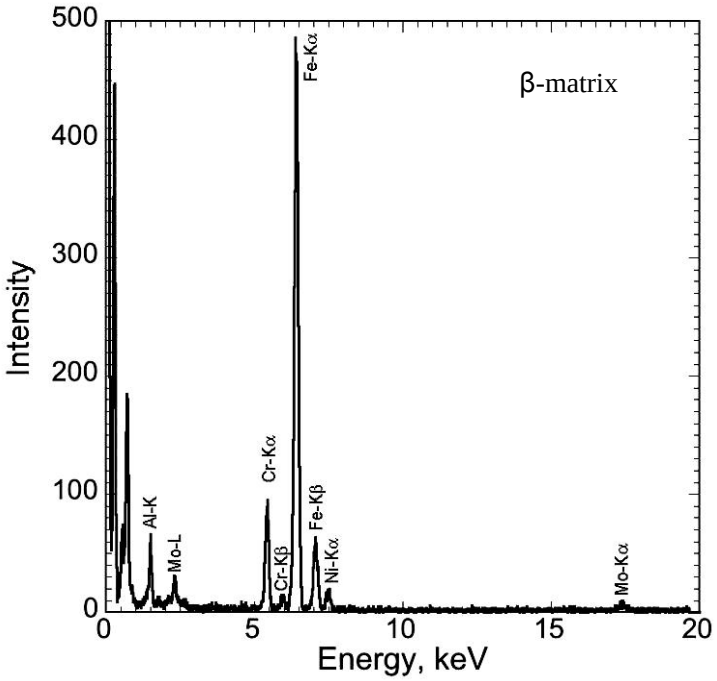


(b)

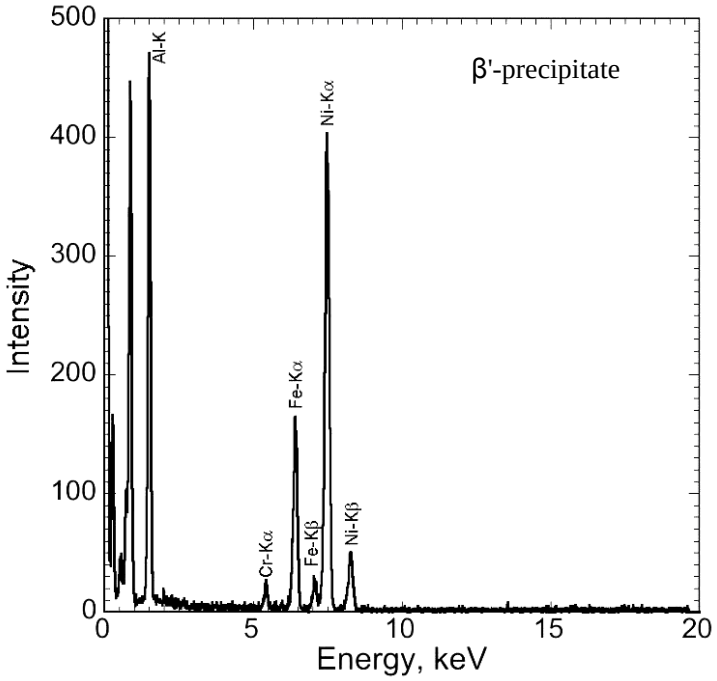


(c)

Figure 6.2 Centered dark-field (using 100_{B2} reflection) TEM micrographs of prototype alloys that are solution treated and then aged at 700 ˚C for 100 hrs: (a) FBB-3, (b) FBB-8, and (c) FBB-12. In each case, the diffraction pattern is shown as inset. TEM work was conducted by Dr. G. Ghosh at Northwestern University.



(a)



(b)

Figure 6.3 As-collected EDS spectra: (a) from the β matrix, and (b) from a β' precipitate in FBB-8 aged at 700˚ for 100 hrs.

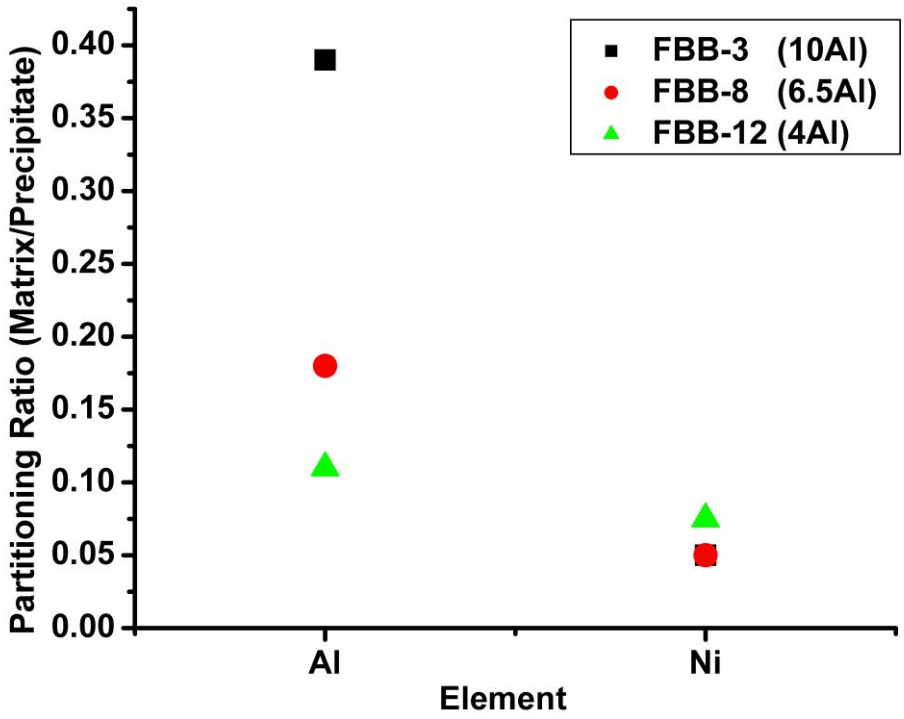


Figure 6.4 Partitioning ratios of Al and Ni in prototype alloys with different Al contents as determined by AEM. All alloys are aged at 700 ˚C for 100 hrs. The results show that the solubility of Ni in Fe matrix in the alloys is almost constant, while that of Al increases significantly as the Al content in the alloys increases.

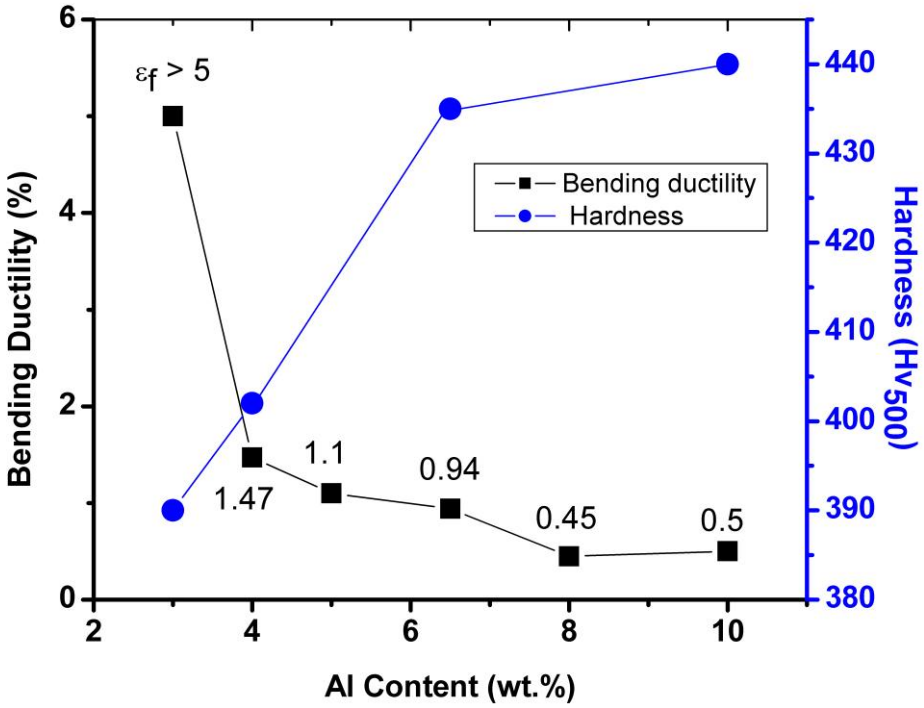


Figure 6.5 The effects of Al content in the alloy on the bending ductility and hardness of prototype alloys, where ε_f is the failure strain on the outer surface of the strip sample.

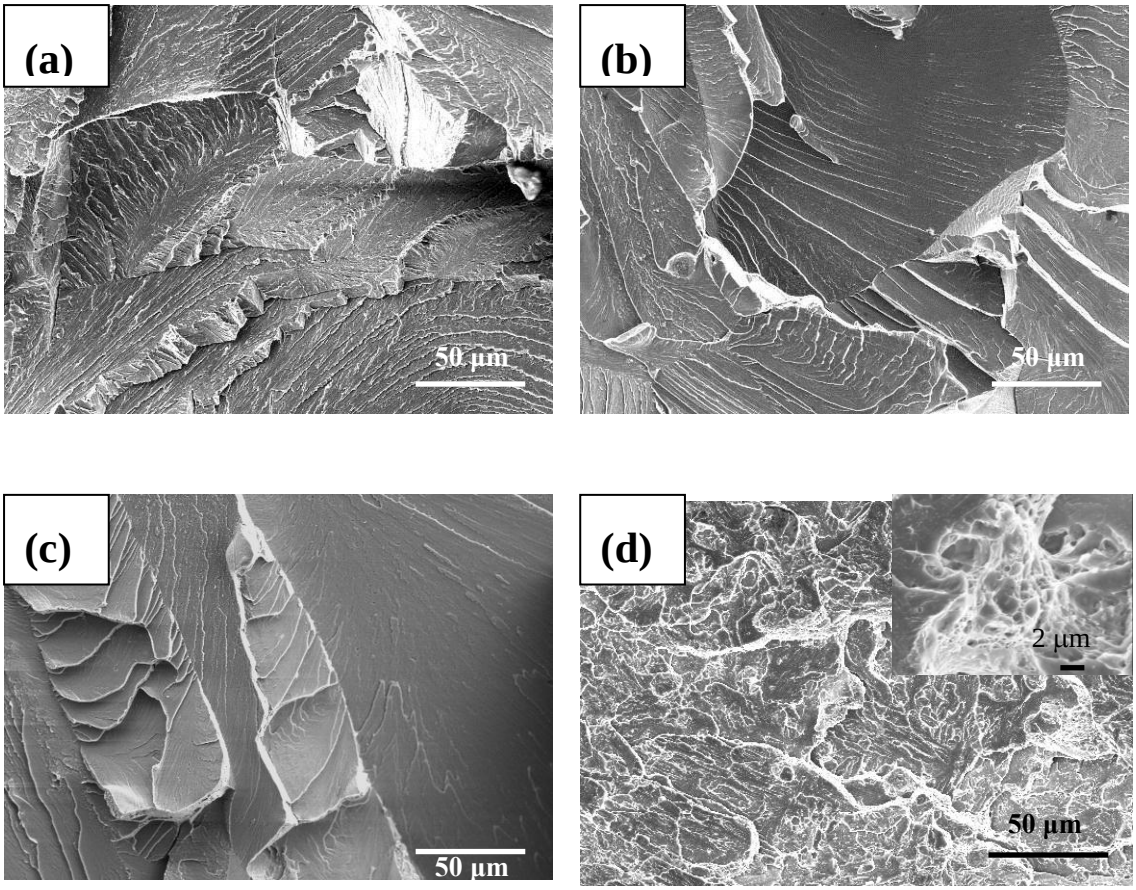


Figure 6.6 Cleavage fracture surfaces of bending-tested samples (a) FBB-3, (b) FBB-8, (c) FBB-9, and (d) FBB-13, the representative ductile fracture is shown as inset.

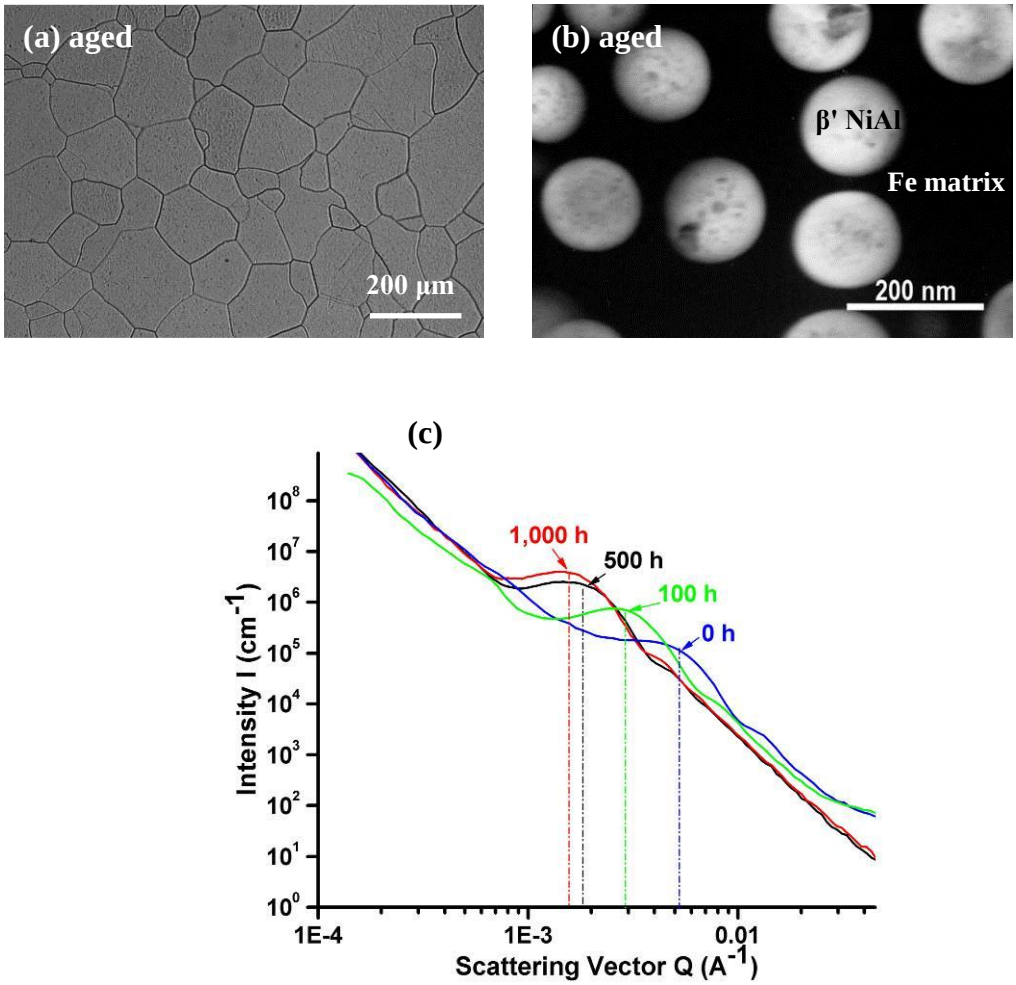


Figure 7.1 The microstructures of FBB-8: (a) optical micrographs showing the average grain size of the alloy aged at 700℃ for 100 h is ~ 100 μm, (b) TEM dark field (DF) micrograph using 100_{B2} reflection showing the average precipitate size of the aged alloy is ~130 nm, and (c) USAXS intensity vs. scattering vector plot of FBB-8 aged for different time periods at 700℃. The inter-particle spacing can be calculated by 2π over peak Q. The TEM work was conducted by Prof. G. Ghosh at Northwestern University.

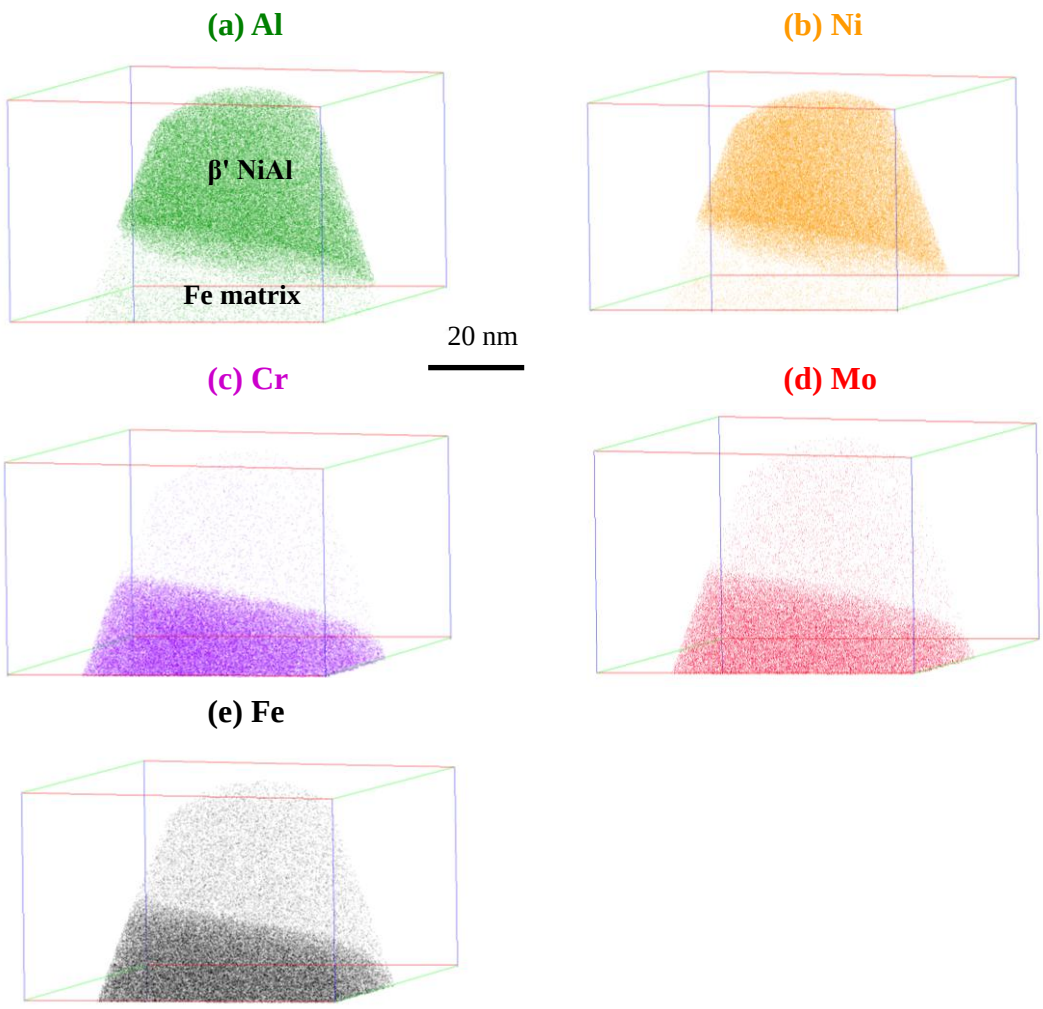
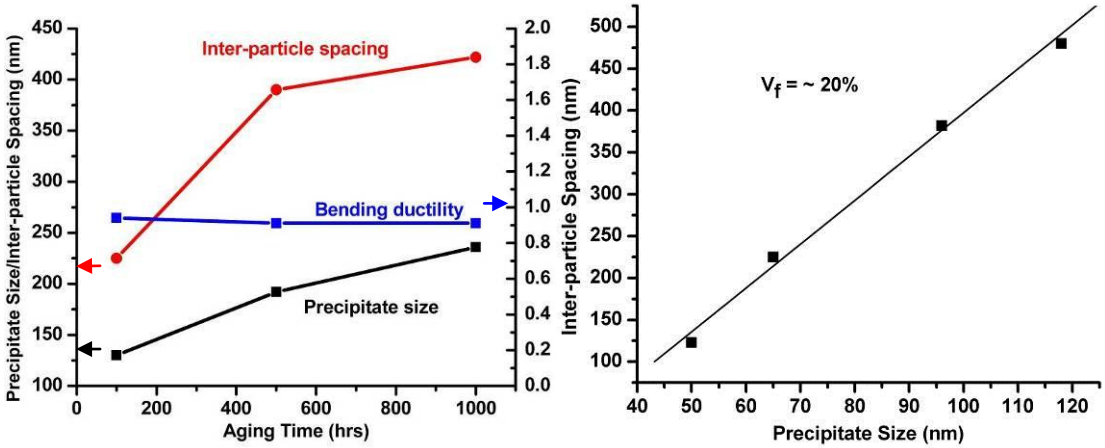


Figure 7.2 Representative atom map of elements in both the β matrix and β' precipitates (Alloy FBB-8). All the compositions can be measured by counting the numbers of collected ions.



(a) (b)

Figure 7.3 Microstructure and ductility of the alloy FBB-8 aged for different time: (a) bending ductility showing an independence of inter-particle spacing and precipitate size, (b) The inter-particle spacing showing a near linear relationship with the precipitate size.

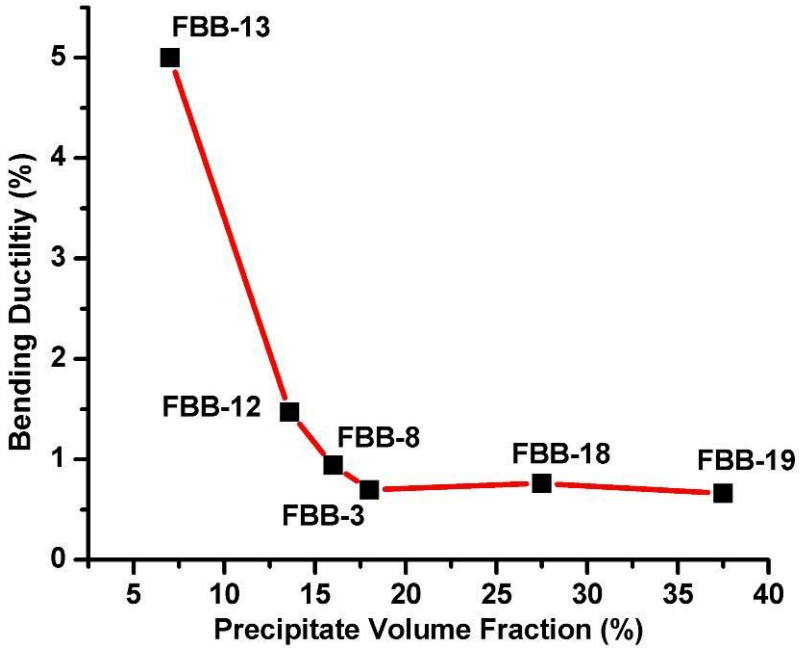


Figure 7.4 Bending ductility vs. β' precipitate volume fraction (V_f) curve showing the ductility decreases as V_f increases.

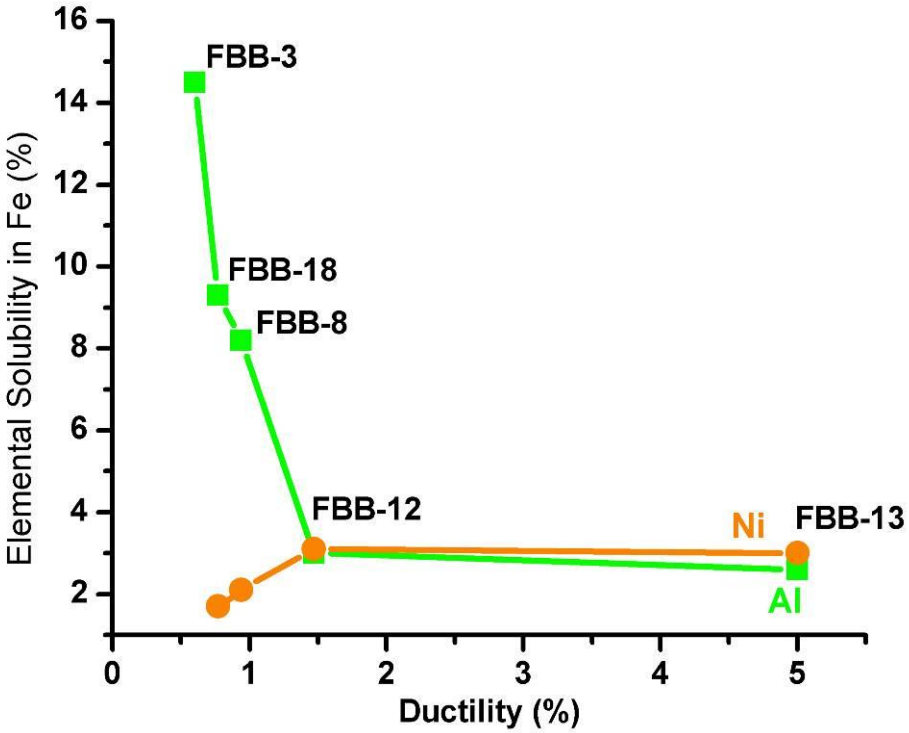


Figure 7.5 Elemental solubility in the β matrix showing low Al and high Ni solubilities contribute to the ductility improvement.

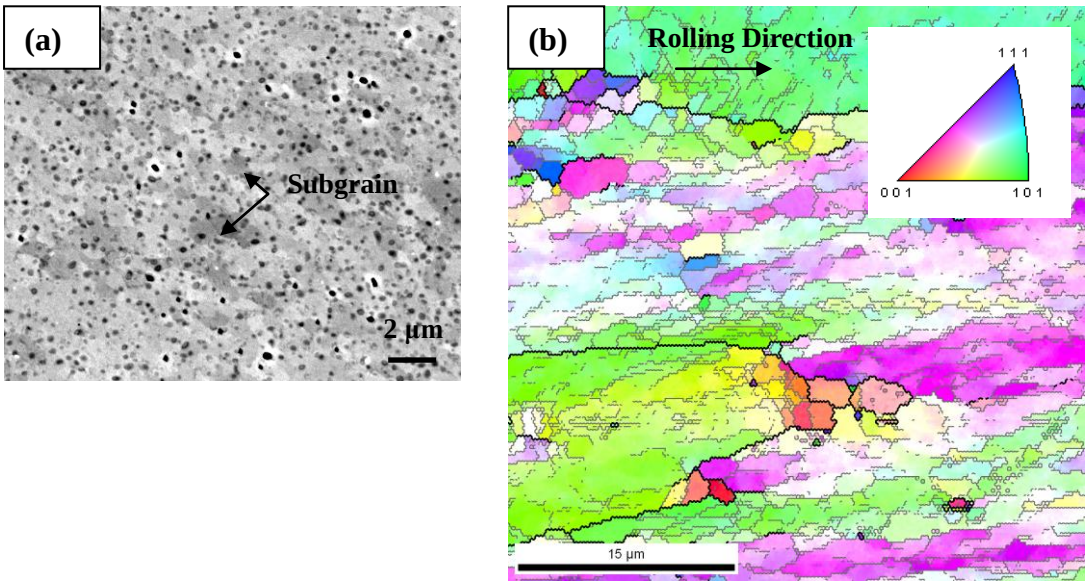


Figure 7.6 (a) SEM image showing the microstructure of the hot-rolled FBB-8 after aging at 850℃ for 1 h, and (b) EBSD mapping showing many subgrains with a size of ~ 1 μm inside the elongated grains.

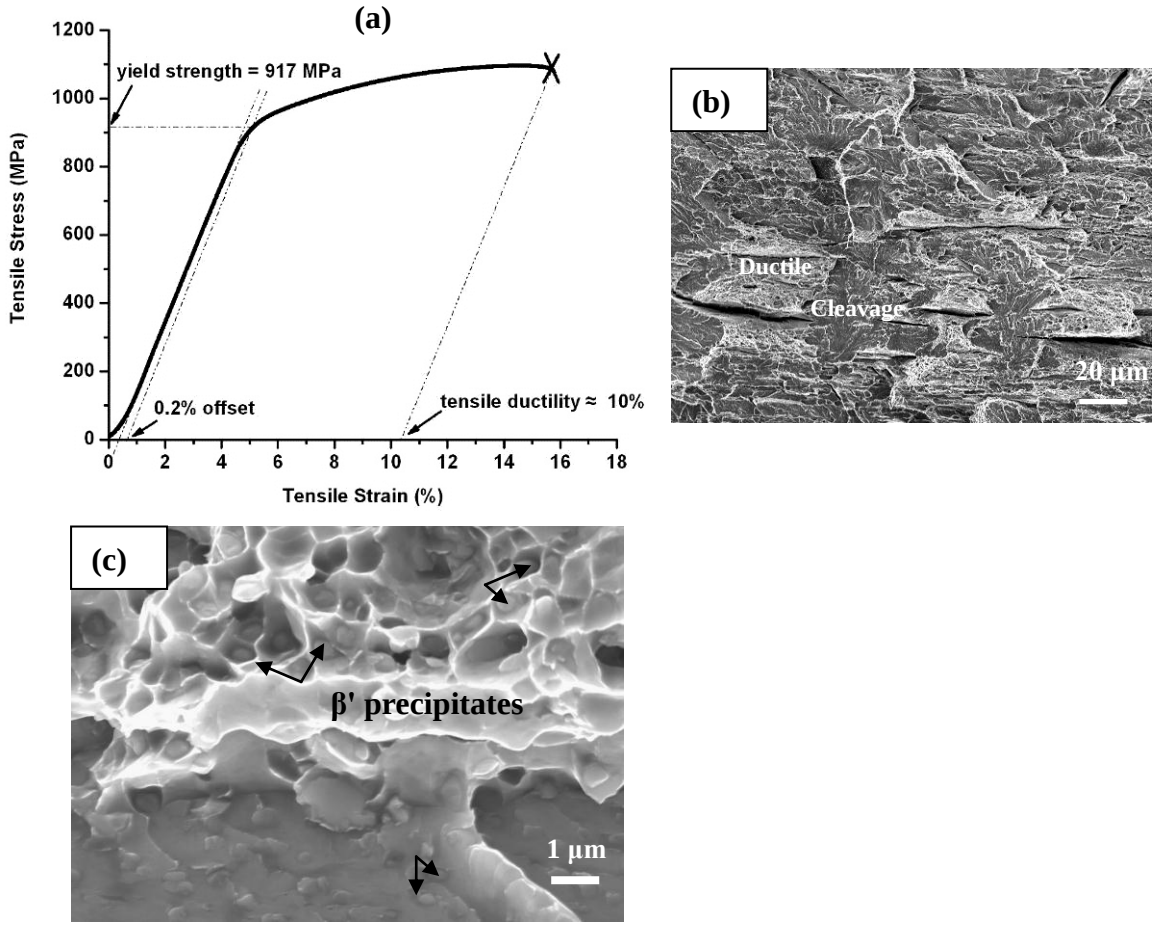


Figure 7.7 (a) Tensile stress vs. strain curve of hot rolled FBB-8, (b) fracture surface showing a mixture mode of cleavage and ductile rupture, and (c) high magnification image of the fracture surface in both ductile and cleavage areas.

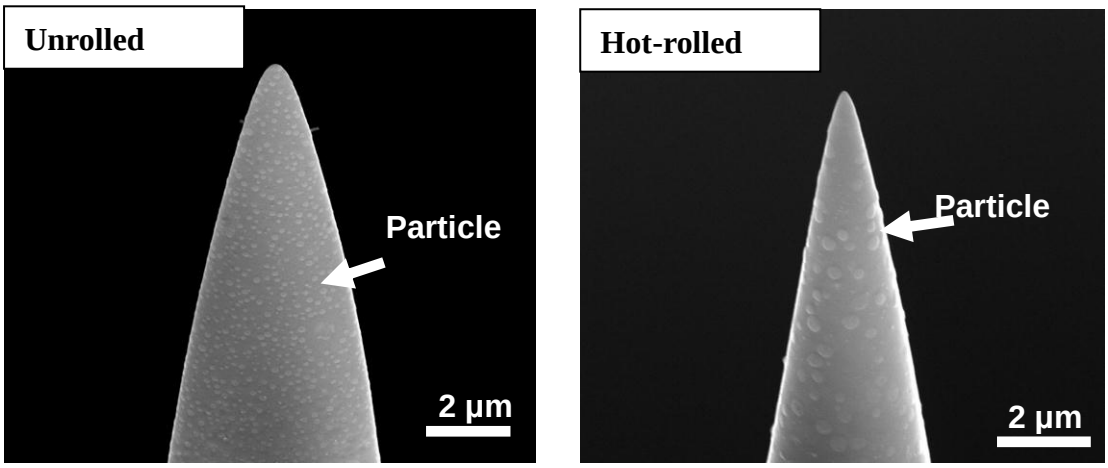


Figure 7.8 Atom-probe samples of the alloy FBB-8 by SEM in (a) unrolled and (b) hot-rolled conditions showing the coarsening of the precipitates.

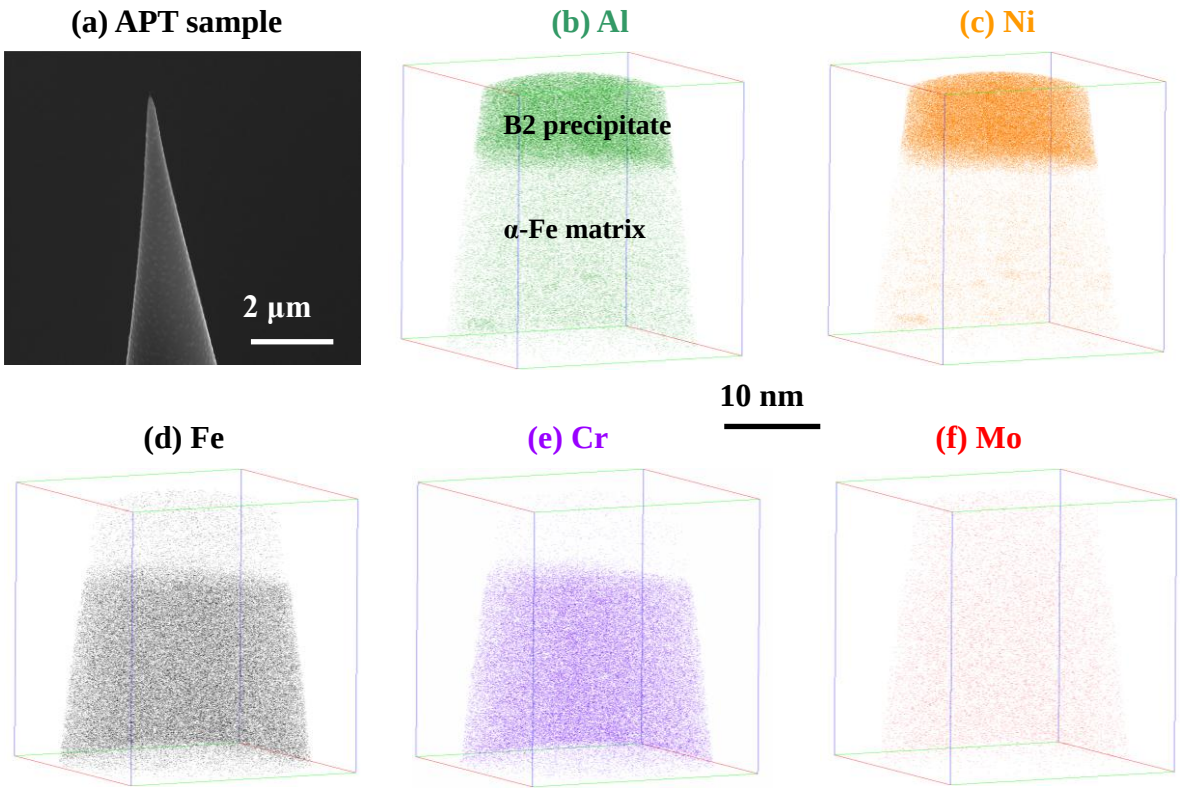


Figure 8.1 APT characterization of the FBB alloys: (a) SEM figure of the FBB-8 sample after polishing, (b)-(f): Representative atom maps of different elements in the alloy FBB-8.

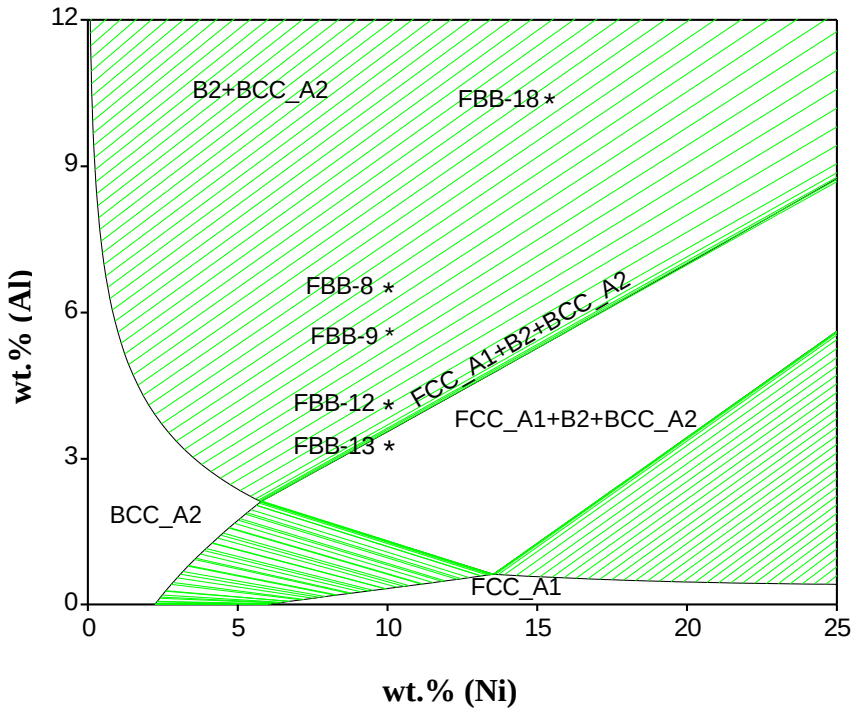
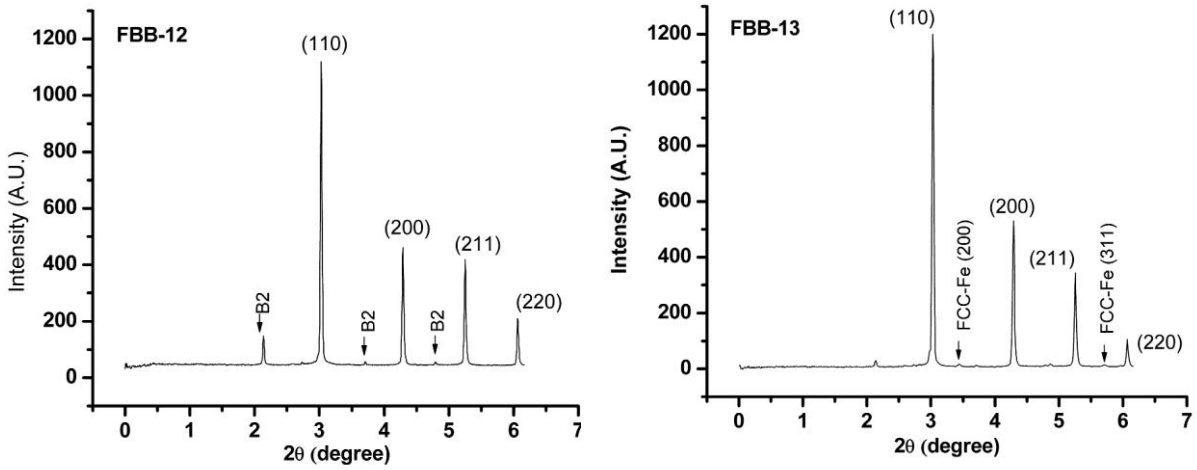
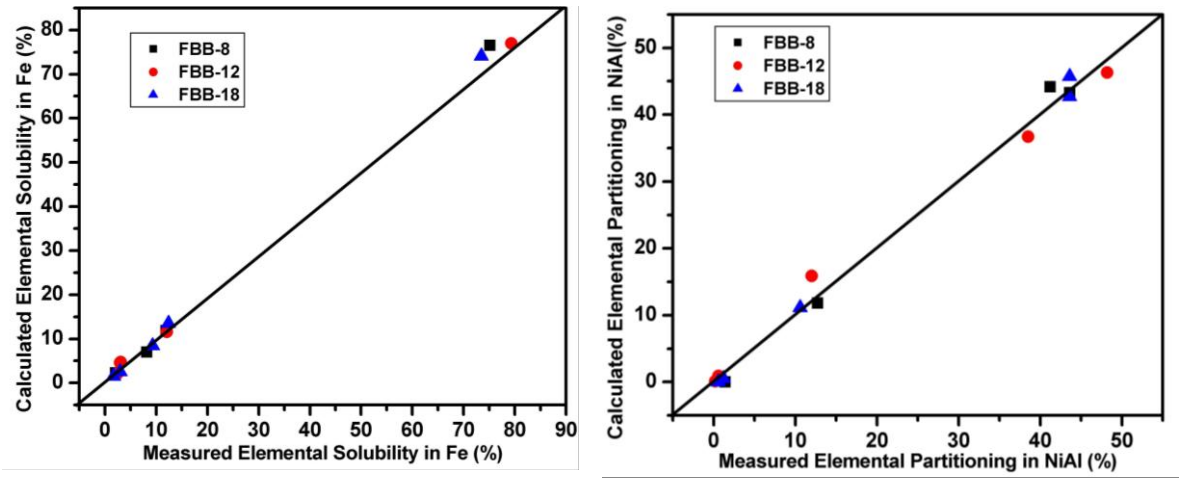


Figure 8.2 Calculated isothermal section of Fe-Al-Ni-10Cr-2Mo (wt.%) system at 700^{o}C. The thermodynamic calculations were conducted by Dr. F. Zhang from CompuTherm LLC.



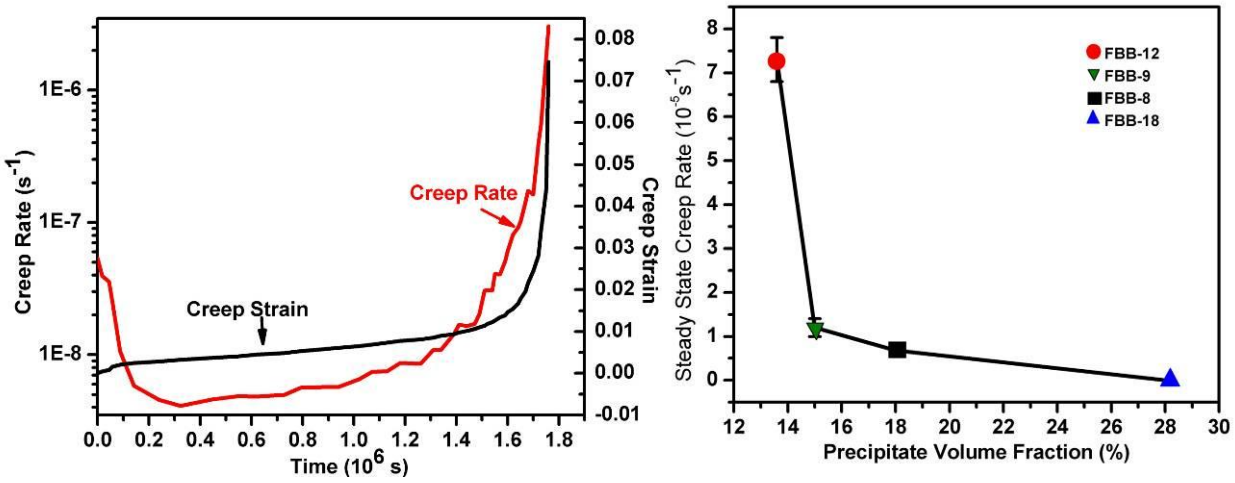
(a) (b)

Figure 8.3 Synchrotron high energy X-ray diffraction of alloys (a) FBB-12 and (b) FBB-13 revealing the possible formation of a small amount of FCC-Fe phase.



(a) (b)

Figure 8.4 Comparisons between the calculated and experimentally determined results showing good agreements: (a) elemental solubilities in Fe matrix, and (b) elemental partitioning in NiAl. Note that the data points of some elements in (a) and (b) overlap with each other as their concentrations are very similar. The detailed concentration of each element can be found in Table 8.2.



(a) (b)

Figure 8.5 (a) Representative tension creep strain and creep rate versus time curves of alloy FBB-18, (b) Steady-state-creep rate decreases as increasing the precipitate volume fraction.

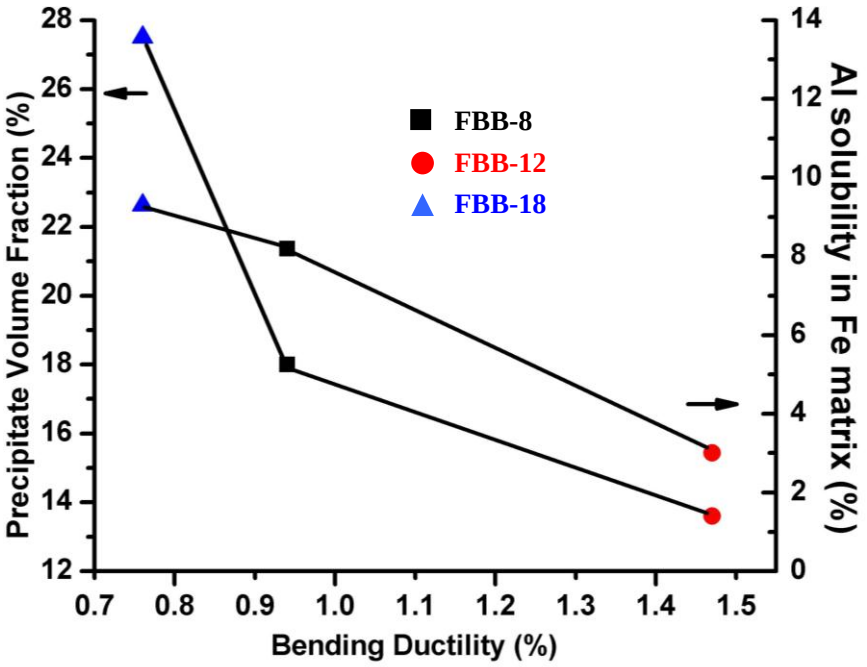


Figure 8.6 Bending ductility increases with decreasing the B2-ordered precipitate volume fraction and Al solubility in Fe matrix.

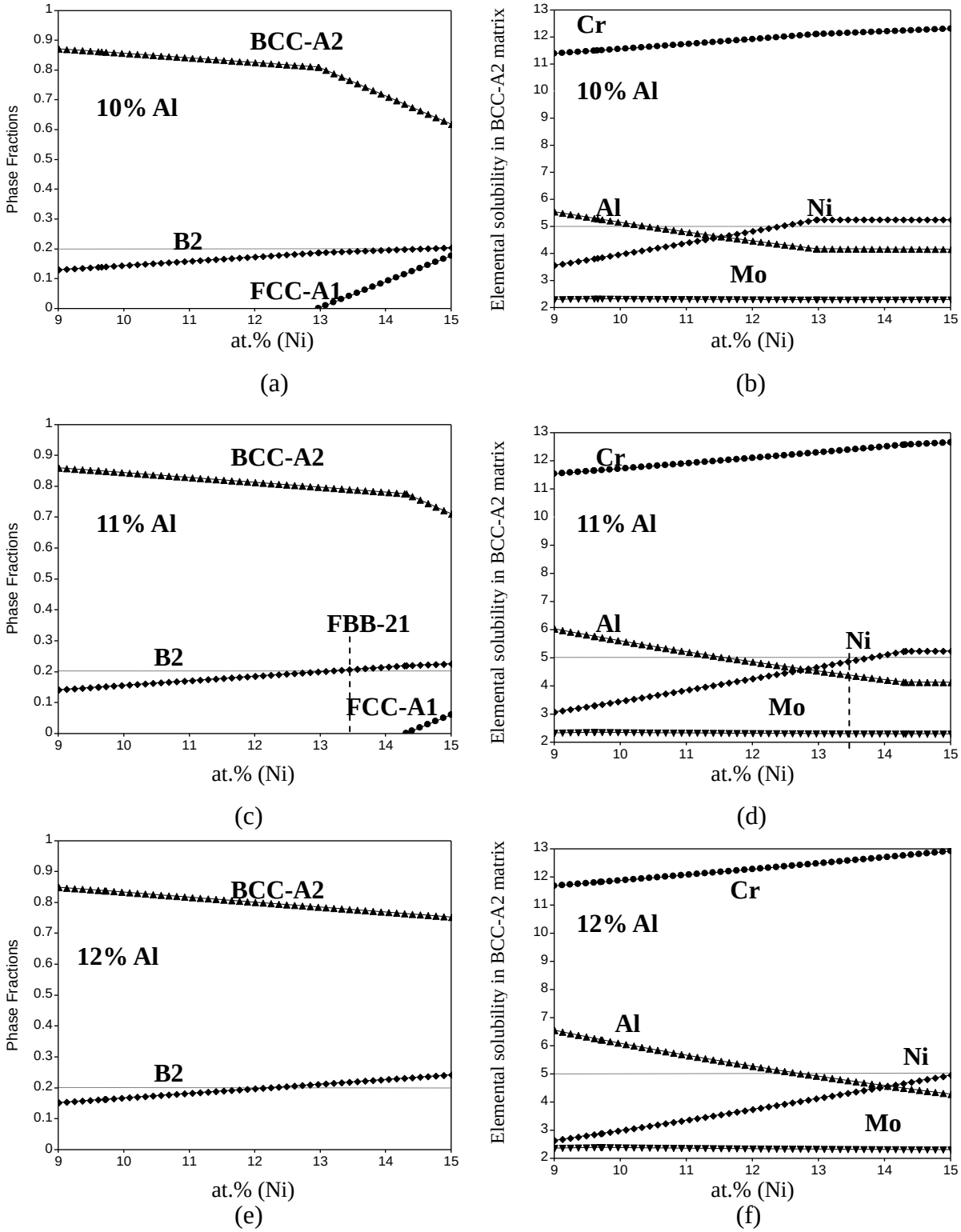
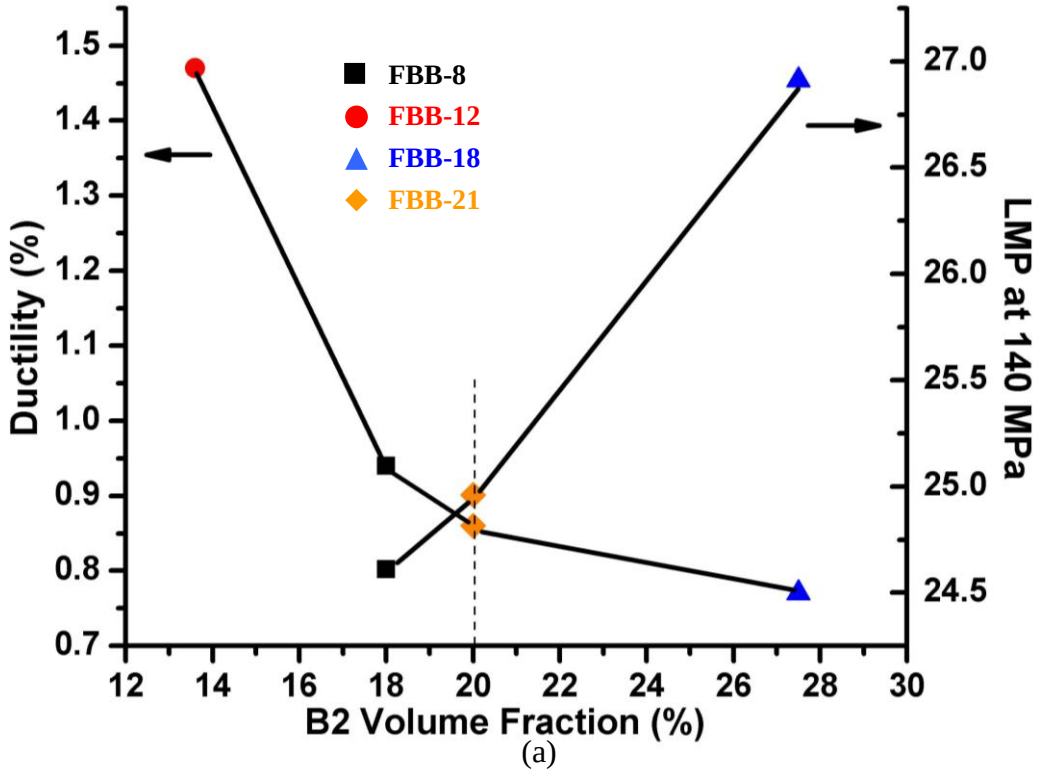
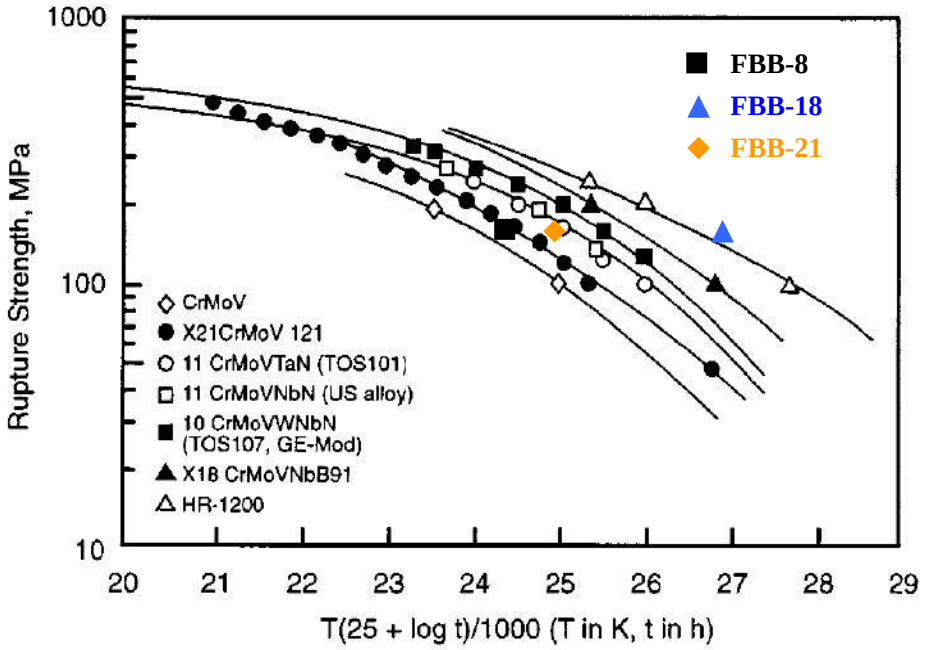


Figure 8.7 Thermodynamic calculations of phase fraction and the solubility of elements in the matrix BCC-A2 phase as a function of the Ni content for (a) and (b): Fe-10Cr-2Mo-10Al-(9-15)Ni, (c) and (d): Fe-10Cr-2Mo-11Al-(9-15)Ni, (e) and (f): Fe-10Cr-2Mo-12Al-(9-15)Ni. The thermodynamic calculations were conducted by Dr. F. Zhang from CompuTherm LLC.



(a)



(b)

Figure 8.8 (a) Comparison of the designed alloys regarding the ductility and Larson-Miller parameter (LMP) at a tensile stress of 140 MPa. The alloy FBB-21 predicted by the thermodynamic calculations exhibited a balance between the ductility and creep resistance, and (b) comparison of the LMPs at 140 MPa between the designed alloys and other ferrite-based candidate materials for steam turbine applications.

VITA

Zhenke Teng was born and grew up in the city of Nanning, Guangxi Province, China on July 30, 1981. He graduated with a B. S. degree and M. S. degree from the Department of Materials Science and Engineering at University of Science and Technology, Beijing in 2003 and 2006. He subsequently joined the Department of Materials Science and Engineering at The University of Tennessee to start his PhD study. In 2011, He received the University of Tennessee Chancellor's Extraordinary Professional Promise Award and Graduate Student Award for Excellence in Research in the Department of Materials Science and Engineering.